

Dissertation zur Erlangung der Doktorwürde der  
Naturwissenschaftlich-Mathematischen Gesamtfakultät der  
Ruprecht-Karls-Universität Heidelberg

vorgelegt von  
Diplom-Physikerin Johanna Berndt  
aus Dresden

Tag der mündlichen Prüfung: 22. Oktober 2012

# Mechanisms of CD95-Clustering

**Gutachter:** Prof. Dr. Roland Eils  
Prof. Dr. Ursula Klingmüller

## Abstract

In this study I investigated the mechanisms of clustering of the apoptosis receptor CD95 after induction with its ligand and the oligomerization level before induction. Previous studies demonstrated that receptor clustering is an essential part in apoptosis signaling. Mostly using biochemical methods and nuclear magnetic resonance the essential role of various mechanisms in receptor clustering could be shown, such as lipid raft localization of the receptor, clustering via the receptor death domain and internalization. An oligomerization of receptors before induction via a so called pre-ligand assembly domain could be shown at high concentrations, so that typically the receptor is assumed to be trimeric before induction. Moreover a consistent model of the role of all mechanisms in different cell types and direct observation on the plasma membrane is still missing. Therefore I investigated receptor clustering in single living cells on the cell membrane using microscopy. In particular I quantified intensities to correlate with the number of molecules. and studied receptor clustering by dynamics measurements using fluorescence recovery after photobleaching. I observed that receptor clustering is concentration dependent and in HeLa at high receptor concentrations the ligand as only crosslinking mechanism yields mean clusters size of seven molecules. Death domain assembly and lipid raft localization do not effect clustering in this cell type. At physiological expression levels the pre-ligand assembly shows an oligomer distribution with an eminent part of monomers or dimers. By knockdown of the receptor the distribution can be pushed to monomers. I made a consistent study for the type II cell line HeLa, considering many proposed clustering mechanisms and showed that ligand binding alone is a strong mechanism that can lead to high levels of clustering. I propose a model where the receptor is present as monomers or dimers at physiological concentrations in the absence of induction.

## Kurzfassung

In dieser Arbeit habe ich den Clusterungs-Mechanismus des CD95 Rezeptors nach Ligandinduktion und der Oligomerisationsstatus vor Induktion untersucht. Bisherige Studien zeigten, dass Clustern von Rezeptoren einen wesentlichen Teil im Apoptose-Signalweg darstellt. Mit hauptsächlich biochemischen Methoden und Kernspinresonanz wurde der Einfluss von verschiedenen Mechanismen auf ein Clustern des Rezeptors erforscht, insbesondere eine Anordnung des Rezeptors in Lipid Rafts, Internalisierung und Bindung über eine Domäne des Rezeptors namens "death domain". Ebenfalls biochemische Methoden konnten eine Bindung zwischen Rezeptoren vor Induktion über die so genannte Pre-Ligand-Assembly-Domäne (PLAD) aufdecken, so dass momentan das Modell eines Rezeptortrimers weit verbreitet ist. Zudem fehlt ein einheitliches Model zur Beschreibung aller Cluster-Mechanismen in unterschiedlichen Zellen ebenso wie Messungen direkt auf der Zellmembran. Daher habe ich das Rezeptor-Clustern auf der Zellmembran von lebenden Zellen mit Mikroskopiemethoden untersucht. Insbesondere wurden Intensitäten quantifiziert um Molekülanzahlen pro Cluster zu ermitteln desweiteren wurden Aggregation mit Diffusionsbestimmung mit Bleichexperimenten gemessen. Ich habe festgestellt, dass das Clustern von Rezeptors von der Rezeptorkonzentration abhängt. In HeLa-Zellen führt die Vernetzung durch den Liganden, als alleiniger Mechanismus zu Clustergrößen von sieben Molekülen. Die Verbindung der death domains und Lipid Raft Lokalisierung wurden als Aggregationsmechanismen in diesem Zelltyp ausgeschlossen. Bei physiologischen Rezeptorkonzentrationen vor Induktion folgt der Rezeptor einer Anzahlverteilung mit einem erheblichen Anteil an Monomeren oder Dimeren. In Zellen mit künstlich verringerter Rezeptorexpression konnte die Verteilung hin zu Monomeren verschoben werden. Ich habe eine einheitliche Untersuchung der HeLa Zelllinie des Types II angestellt unter Betrachtung aller vorgeschlagenen Cluster-Mechanismen und habe gezeigt, dass Ligandeninduktion als einziger Mechanismus zu großen Rezeptoraggregationen führen kann. Für physiologische Konzentrationen ohne Induktion ist das Modell eines Rezeptors anzunehmen, der hauptsächlich mono- und dimerisch vorliegt.

# Contents

<b>I. Introduction</b>	<b>8</b>
<b>1. Apoptosis and CD95-Receptor Clustering</b>	<b>9</b>
1.1. Apoptosis . . . . .	10
1.1.1. The Functions of Apoptosis . . . . .	10
1.1.2. Apoptosis Malfunctioning and Related Diseases . . . . .	10
1.1.3. The Process of Apoptosis and its Molecular Mechanism . . . . .	11
1.2. The CD95 Receptor . . . . .	14
1.2.1. The Structure of CD95 . . . . .	14
1.2.2. The CD95 Signaling Pathway . . . . .	15
1.2.3. The Two different Cell Types . . . . .	17
1.2.4. Modifications of CD95 . . . . .	17
1.3. Regulation Mechanisms . . . . .	19
1.3.1. The Role of Lipid Rafts in Type I and Type II cells . . . . .	19
1.3.2. The Actin Cytoskeleton . . . . .	20
1.3.3. The Role of Receptor Internalization . . . . .	21
1.3.4. Receptor Oligomerization on the Plasma Membrane before Induction	21
1.3.5. Receptor Oligomerization after Induction . . . . .	23
1.3.6. Models of CD95 Oligomerization Mechanisms . . . . .	25
<b>2. Microscopy Approaches to Characterize Receptors at Single Cell Level</b>	<b>27</b>
2.1. Confocal Microscopy . . . . .	28
2.1.1. Fluorescence Microscopy . . . . .	29
2.1.2. Laser Scanning Confocal Microscopy . . . . .	30
2.1.3. Spinning Disc Confocal Microscopy . . . . .	32
2.1.4. Signal Quantification and Signal Disturbances . . . . .	32
2.1.5. The Limit of Resolution . . . . .	34
2.2. Stimulated emission depletion . . . . .	36
2.3. Protein Dynamics and Clustering . . . . .	40
2.3.1. Diffusion Models . . . . .	40
2.3.2. Membrane Models . . . . .	41
2.4. Fluorescence Recovery after Photobleaching . . . . .	42

<b>II. Materials and Methods</b>	<b>44</b>
<b>3. Materials and Methods</b>	<b>45</b>
3.1. Chemicals, Antibodies, Stable Cell Lines . . . . .	46
3.2. Immunostaining . . . . .	50
3.3. Flow Cytometry . . . . .	50
3.4. Confocal Laser Scanning Imaging . . . . .	51
3.5. Fluorescence Recovery after Photobleaching . . . . .	52
3.6. Spinning Disc Confocal Imaging . . . . .	52
3.7. Stimulated Emission Depletion Microscopy . . . . .	52
3.8. Dot Segmentation Image Analysis . . . . .	53
<b>III. Results</b>	<b>55</b>
<b>4. CD95 Concentration</b>	<b>56</b>
4.1. The Number of Receptors per Cell . . . . .	57
4.1.1. Quantification of CD95 by Flow Cytometry . . . . .	57
4.1.2. The Typical CD95 Expression is roughly 10000 Receptors per Cell . . . . .	58
<b>5. CD95-Clustering at High Expression Levels</b>	<b>60</b>
5.1. CD95 resides into Dots at the Plasma Membrane upon Induction . . . . .	61
5.2. Quantification of Dot Formation . . . . .	66
5.2.1. The Number of Dots increases over Time . . . . .	67
5.2.2. The Dot Size increases over Time . . . . .	68
5.2.3. The Majority of Dots contains about seven Molecules . . . . .	69
5.3. Clustering measured by Dynamics Observation . . . . .	71
5.3.1. Fluorescence Recovery after Photobleaching . . . . .	71
5.3.2. CD95 diffuses three to four-fold slower upon Induction . . . . .	76
5.3.3. Possible Slowdown Reasons . . . . .	76
5.4. The Only Aggregation Mechanism is Crosslinking by the Ligand . . . . .	78
5.4.1. The Receptor Aggregation is independent of the Lipid Rafts . . . . .	79
5.4.2. The Receptor Aggregation is independent of the Death Domains . . . . .	81
5.4.3. The Dot Size is Concentration Dependent . . . . .	83
<b>6. CD95-Clustering at Physiological Expression Levels</b>	<b>85</b>
6.1. The CD95 Organization on the Plasma Membrane at Confocal Resolution . . . . .	86
6.1.1. Quantification of Dots . . . . .	88
6.1.2. The Number of Dots is Proportional to the Cell Size . . . . .	91
6.1.3. The Mean Number of Dots per Cell is 4300 . . . . .	92

## Contents

---

6.1.4. The Intensity Calibration reveals that most Dots contain less than Three Receptors . . . . .	94
6.1.5. The Lower Membrane represents the Whole Cell . . . . .	95
6.2. Simulation of the Microscope Characteristics . . . . .	96
6.2.1. In Silico Images . . . . .	99
6.2.2. Many Oligomers contain less than Three Receptors . . . . .	99
6.3. Stimulated Emission Depletion allows for Higher Resolution of Clusters . .	101
6.3.1. STED Imaging of CD95 . . . . .	102
6.4. The Simulation of the Characteristics of STED Images . . . . .	104
6.4.1. CD95 on HeLa Cells is either Dimeric or a Mix of Oligomers with a Mean of Two Receptors per Cluster . . . . .	106
6.4.2. CD95 is Monomeric in Knockdown Conditions . . . . .	110
<b>7. Discussion</b>	<b>112</b>
7.1. The CD95 Oligomerization after Induction . . . . .	113
7.2. The Lipid Rafts can be excluded as Oligomerization Mechanism . . . . .	114
7.3. The Death Domains can be excluded as Oligomerization Mechanism . . .	115
7.4. The Oligomerization is Concentration Dependent . . . . .	116
7.5. Oligomerization on the Plasma Membrane at Physiological Expression Levels	117
<b>Appendix</b>	<b>120</b>
A.1. Estimation of the Diffusion Coefficient from the Bleaching Profile . . . . .	121
<b>List of Figures</b>	<b>122</b>
<b>Glossary</b>	<b>124</b>
<b>Bibliography</b>	<b>126</b>
<b>Acknowledgements</b>	<b>136</b>

Part I.

Introduction



# 1. Apoptosis and CD95-Receptor Clustering

## 1.1. Apoptosis

Apoptosis is one mode of programmed cell death in multicellular organisms, designed for the removal of unwanted cells of the same body.

Contrary to necrosis - a premature demise of single cells of an organism accompanied by inflammation - apoptosis is an organized active process of the dying cell. Following a biochemical cascade the cell degrades itself, so that its remains can be phagocytosed by the surrounding cells and components can be recycled. In that process the apoptotic cells show typical morphological features, notably blebbing, cell shrinkage, nuclear fragmentation and chromatin degradation [1], instead of bursting and spilling any possibly damaging content. In a human body 50 to 70 billion cells die every day due to apoptosis thus maintaining the functionality of the organism.

### 1.1.1. The Functions of Apoptosis

Apoptosis' central task of killing unwanted cells leads to several different areas where this process plays a central role.

Typically apoptosis eliminates abnormal, misplaced, non-functional or harmful cells, Figure 1.1 F. Using cytotoxic T cells and natural killer cell to eliminate infected cells in time is crucial to prevent viral infections from spreading. Another example is apoptosis as response to stress or DNA damage, e.g. by UV-light.

A second task of apoptosis is the maintenance of homeostasis, Figure 1.1 E. In healthy bodies blood and skin cells, for instance, are constantly renewed. This proliferation, however, has to be continuously compensated by cell death.

Apoptosis plays a major role in the development of most plants and metazoan organisms especially for tissue remodeling, such as sculpting and deleting structures, Figure 1.1 A, B, C, D. The formation of digits in some higher vertebrates is a well-studied example, where apoptosis eliminates the cells between developing digits .

Apoptosis is also indispensable in the development of the immune system, especially in the maturation of lymphocytes. About 95% of the freshly produced T-cells are deleted in the thymus during maturation, because they are either not functional, failed to rearrange their T cell receptor gene, or even autoreactive [3]. The termination of an immune response also requires the elimination of the activated mature T cells by apoptosis.

### 1.1.2. Apoptosis Malfunctioning and Related Diseases

Since apoptosis is implicated in a plethora of vital functions of a healthy organism, malfunctioning of apoptosis can lead to an extensive variety of diseases. These can be

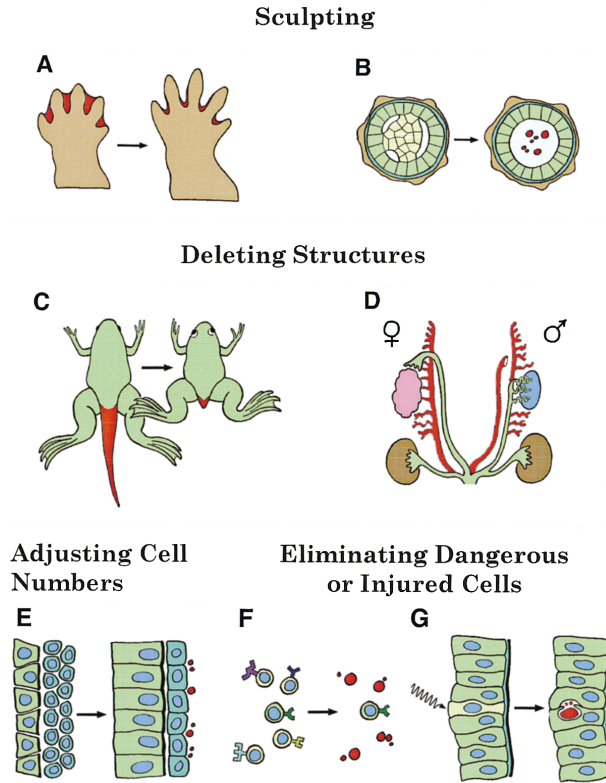


**Figure 1.1.:** The different functions of apoptosis in animal development according to [2]

categorized into two groups, depending on whether excessive or too little apoptosis occurs [4], [5].

Unwanted apoptosis leads to a pathological cell loss, as it occurs with ischemic diseases, Alzheimer's disease, neurodegenerative disorders or AIDS [6]. When apoptosis is insufficient cells can grow excessively leading e.g. to tumor growth or autoimmune diseases [7].

### 1.1.3. The Process of Apoptosis and its Molecular Mechanism

It would be very harmful for the organism, if half-dead cells were around, therefore the decision for apoptosis should be taken in an all or nothing manner. The need for apoptosis can come from the cell itself, from its surrounding tissue or from a cell that is part of the immune system. Therefore there are various stimuli, extrinsic or intrinsic inducers, that induce the apoptotic signaling. This signaling pathway then leads to the decision,

whether to start apoptosis or instead block the apoptotic signal and lead to a pro-survival pathway.

Apoptotic cell death is carried out by a group of proteases called caspases. There are initiator caspases, namely caspase 8, 10, 9 and 2) that upon signaling activate the effector caspases (caspase 3, 7 and 6) by proteolytic cleavage, the so called caspase cascade. The effector caspases then cleave the proteins of the cell. Those proteins include the cytoskeleton proteins, leading to a shrinkage of the cell and a breakdown of the nuclear envelope. Further they activate the endonucleases, that are responsible for the DNA degradation into chromatin bodies, with DNA fragments of 180-185 base pairs length. The cell membrane shows irregular buds, a process called blebbing, and the cell breaks apart into vesicles, the so called apoptotic bodies, that are later phagocytosed by other cells.

In a normal living cells, when no apoptosis signal is present, the caspase inhibitor XIAP (X-chromosome linked inhibitor of apoptosis protein) is responsible for inhibiting wrongly activated effector caspases and enzymatically targeting them for degradation. When apoptosis is signaled, the equilibrium between XIAP and the caspases is shifted to allow for the caspase cascade to execute apoptosis. There are two signaling pathways that can lead to this shift of equilibrium - the extrinsic and the intrinsic pathway.

The main feature of the evolutionary older intrinsic pathway is the permeabilization of the mitochondria outer membrane (MOMP), that leads to release of cytochrome c and other pro-apoptotic factors such as SMAC (small mitochondria-derived activator of caspases). SMAC inhibits XIAP thus shifting the equilibrium. Cytochrome C binds to apoptotic protease activating factor-1 (Apaf-1). This interaction with cytochrome c induces a conformational change in Apaf-1, promoting Apaf-1 oligomerization to initiate apoptosome formation. The apoptosome then binds to the pro-caspase 9 to start the caspase cascade and execute apoptosis. The intrinsic pathway can be started by various stimuli and is regulated by various proteins, such as those of the Bcl-2 family, that can promote and inhibit apoptosis via this pathway.

One way to start apoptosis is the induction of death receptors of the so called TNF receptor family. This family of receptors has a common motive in the intracellular part, called the death domain [9]. This death domain can oligomerize and recruit adaptor proteins TRADD or FADD [10]. These in turn can directly recruit initiator caspases and by dimerization these are activated [11].

The extrinsic pathway is induced by receptors of the so called TNF receptor family, called death receptors. This family of receptors has a common motive in the intracellular part, called the death domain [9]. This death domain can oligomerize and recruit adaptor proteins TRADD or FADD [10]. These in turn can directly recruit initiator caspases and

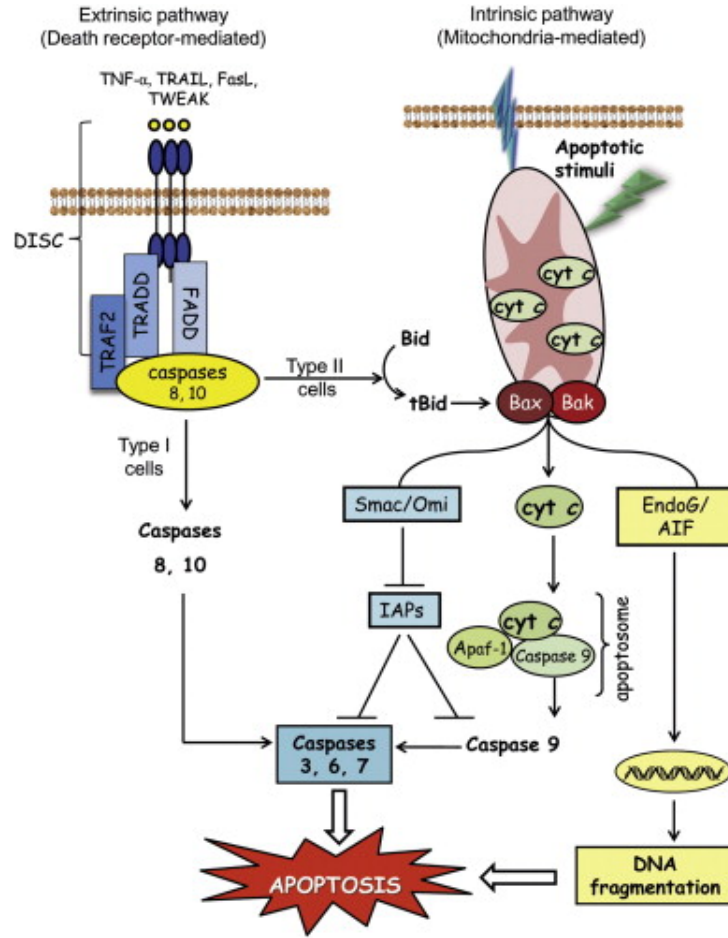


**Figure 1.2.:** Model of the intrinsic and extrinsic signaling pathways for apoptosis. The intrinsic apoptosis pathway is characterized by mitochondria regulation. The extrinsic pathway is induced by death receptor induction and can induce apoptosis by directly activating the caspase cascade [8]

by dimerization these are activated [11]. When this signal is strong enough to overcome the caspase inhibitor XIAP the necessary caspase cascade can directly start apoptosis as described above.

## 1.2. The CD95 Receptor

### CD95-mediated Functions of Apoptosis

One way to initialize apoptosis is the induction of the CD95 receptor, one of the so-called death receptors. This particular pathway plays an eminent role in the immune system [12]:

CD95 is responsible for the peripheral deletion of activated mature T cells at the end of an immune response, called T cell homeostasis, the killing of targets such as virus-infected cells or cancer cells by cytotoxic T cells or natural killer cells, the removal of autoreactive T cells [13], [3] and the killing of inflammatory cells at immune-privileged sites such as the eye and testis [14], [15].

#### 1.2.1. The Structure of CD95

CD95 (Tumor necrosis factor receptor superfamily member 6, APO-1, APT-1) is a transmembrane receptor of the TNF-receptor superfamily, which has a predominant function in apoptosis. It is a type I transmembrane protein with a mass of 45 kDa.

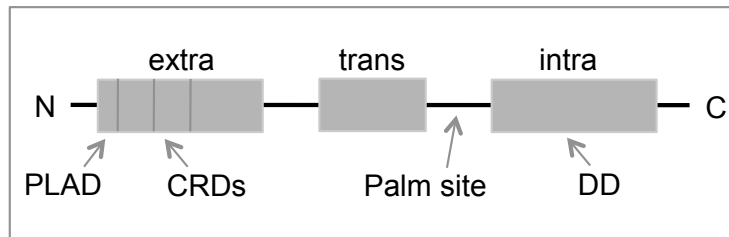


**Figure 1.3.:** Structure of CD95. The N-terminal extracellular domain contains three cysteine rich domains and the so called pre ligand assembly domain (PLAD). On the intracellular part contains the characteristic death domain. The amino acid cysteine 199 serves as a palmitoylation site that is located on the intracellular part of the receptor near the transmembrane domain.

The structure is very similar to many TNF receptors, Figure 1.3. As a transmembrane receptor it has the typical hydrophobic transmembrane helix (amino acids 174-190) and an extracellular and an intracellular domain.

The intracellular part contains the death domain (DD), an 80 amino acid long domain characteristic for all TNF receptors. This key domain of these receptors binds one of the adaptor proteins FADD or TRADD to serve as a platform for the caspase activation, that will lead to apoptosis.

Another homologous part to all TNF receptors are the three highly conserved cysteine-rich-domains (CRD) located in the extracellular part (CRD1: 47-83, CRD2: 84-127, CRD3-128-166). Contrary to most other TNFs the linker between CRDs and transmem-

brane domains is only 8 amino acids short allowing for less flexibility. CRD2 and CRD3 [9] are responsible for ligand binding, while the functional role of CRD1 remained obscure for a long time.

In 1999, however, the pre-ligand-assembly domain (PLAD) was identified in CD95 and also other members of the TNF receptor superfamily [16], ([7] in CD95), ([17] in the receptors p60 and p80 of the TNFR superfamily). It is part of the CRD1 at the N-terminal end of the receptor and it mediates a specific ligand-independent assembly of the receptors. The receptors were shown to self associate via these domains by various biochemical and biophysical techniques [9]: gel filtration and chemical crosslinking experiments [7] or fluorescence energy transfer (FRET) [18]. With the latter it could be shown that dominant interference of CD95 mutant of the disease autoimmune lymphoproliferative syndrome (ALPS), where the death domain is either mutated or truncated, is occurring through pre-ligand association of receptors via the PLAD-domain.

### 1.2.2. The CD95 Signaling Pathway

Apoptosis can be initiated by CD95. Upon induction of apoptosis the adaptor molecule FADD (Fas-associated-protein with DD) binds homotypically to the death domain of CD95 receptor [12], [19]. FADD then recruits procaspase 8 or 10 via its death effector domain to form a complex called DISC (death inducing signaling complex) thereby connecting the receptor to the apoptotic effector machinery [12]. Procaspase 8 is activated by dimerization at the DISC [20], auto-cleavage then leads to further stabilization and possible release to the cytosol. Caspase 8 is an initiator caspase that - depending on cell type - can induce the intrinsic or extrinsic apoptosis signaling pathway.

### Induction Mechanisms

Given its importance for the protection against harmful processes, CD95-mediated apoptosis can be initialized in various different mechanisms.

It was shown that the CD95 receptor can mediate apoptosis by chemical activation as in the case of apoptosis by ET-18-OCH<sub>3</sub> [21], [22]

More commonly CD95 activation happens through induction of the receptor by binding of the respective ligand or antibody: The natural CD95-ligand presents itself in two different form. The transmembrane form is presented on the plasma membrane of another cell, such as a natural killer cell. (Referenz). The soluble form is generated by cleavage of the transmembrane form, it will furthermore referred to as soluble CD95 ligand, sCD95L (Referenz).

Experimentally CD95 can be activated by artificial inducers. For instance ILZ-sCD95L is an artificial fusion of the soluble ligand to isoleuzin (ILZ) forcing a stable trimerization of the ligand. This results in higher activation and cell death upon induction. In our Laboratory Clarisse Liesche could show, that while sCD95L is not able to kill HeLa cells, ILZ-sCD95L can induce 100% cell death. HeLa cells overexpressing CD95 however, are as susceptible to the soluble form as to the ILZ and cell death occurs at same speed. Among other artificial inducers is the use of antibodies, for instance the agonistic APO1-3, that induces cell death as efficiently as the ligand. On the other hand, the antibody APO1-1 is not agonistic, while still showing high binding affinity to the receptor.

### Inhibition of CD95-induced Apoptosis

In some experiments when examining the early events of apoptotic signaling and the receptor distribution on the plasma membrane, the cells should stay intact and not die of apoptosis. There are various ways to inhibit apoptosis.

The most direct way to inhibit apoptosis is to block the caspase cascade. The drug z-vad irreversibly binds to the catalytic site of caspase proteases and thereby inhibits induction of apoptosis.

From a family of proteins from herpesviruses come v-FLIPs, which contain death effector domains and can inhibit apoptosis [23] to evade host defenses and contribute to the propagation of the virus. The human homologue is the protein c-FLIP (FLICE inhibitory protein). It can compete with caspase 8 at the DISC and therefore inhibit caspase activation [24], [25]. Constitutive expression of c-FLIP can lead to Hodgkin's disease [23].

As described before the intrinsic apoptotic pathway is regulated by members of the Bcl-2 protein family. All mitochondrial activities can be blocked by overexpression of Bcl-2 or Bcl-x<sub>L</sub> [26], [27].

v-FLIPs is a family of proteins from a herpesvirus, that contain death effector domains and can inhibit apoptosis [23] to evade host defenses and contribute to the propagation of the virus.

### Survival Pathways

It has been shown that caspase 8 can activate the NF- $\kappa$ B pathway [28] and that TNF receptors are massively involved in NF- $\kappa$ B survival pathways [29]. CD95 was also shown *in vivo* to be involved in survival signaling in mice controlling neuronal branching in the developing brain [30], [31] and survival signaling via the DISC could be also shown [32].



### 1.2.3. The Two different Cell Types

From the activation of caspase 8 there are two signaling pathways that lead to apoptosis [33]. Cells can be divided into two types, depending on which pathway they chose. Type I cells use the extrinsic pathway, where the caspase cascade is mainly activated directly by the DISC, whereas type II cells choose an intrinsic pathway, where caspases are activated via mitochondrial outer membrane permeabilization, as described above, Figure 1.2.

To test whether cells are of type I or type II, apoptosis is manipulated with Bcl-2 or Bcl-x<sub>L</sub>. In type II cells these proteins inhibit apoptosis, while type I cells, still die using the extrinsic pathway, possibly slower, since they are deprived of help of the intrinsic pathway.

For CD95-induced cell death the discriminator between type I and type II apoptosis is the XIAP levels [34].

One example for a mixed cell type is the MCF7 lymphocyte cell line, that can be turned from one type to the other by expression of specific proteins [33].

It has been proposed that evolution initially developed only the intrinsic pathway Scaffidi1998 and extrinsic pathway was developed later.

The first signaling events on the extrinsic pathway for type I cells are very well described in [35]. Upon induction of the ligand CD95 forms microaggregates, that can be observed on SDS-Page-Gels [36]. Then FADD is recruited to the DISC and CD95 forms clusters that can be observed in confocal microscopy [37], a process, that can only efficiently occur, with caspase 8 binding. In a next step the activated receptor is internalized into endosomes, in an actin cytoskeleton dependent manner [38], [35].

### 1.2.4. Modifications of CD95

Apoptosis signaling is regulated on many different levels, the early signaling events being determined by the receptor and its surrounding. I want to start with modifications and mutations on the receptor itself leading then to the further regulation mechanisms in the surroundings, chapter 1.3 .

**Ubiquitination** of receptors in general is mainly responsible for surface receptor internalization, DNA repair and protein kinase activation. While ubiquitination plays a major role in regulation and sorting of the membrane bound form of CD95L, CD95 is not massively regulated by ubiquitination. Downstream again, caspase 8 can be further stabilized by ubiquitination and also the IAP (inhibitor of apoptosis) family members can be regulated by ubiquitination [39].

pathway	cell line	cell type
<b>type I</b>	SKW 6.4	lyphoblastoid
	H9	T cell line
	Hep G2, BJAB, L929, K50	-
	MCF7	with CD95 and casp3 over-expression
	Hek 293T	-
<b>type II</b>	CEM	T cell line
	Jurkat	T cell line
	HeLa	cervical cancer (epithelial)
	MCF7	breast cancer

**Table 1.1.:** list of cell types and their CD95 signalling pathway: according to [33]

**Palmitoylation** can influence membrane binding and targeting and for many receptors is particularly responsible for localization and and enrichment in the lipid rafts, regulation effective signal transduction [40]. For the vast majority of proteins palmitoylation is occurring post translationally at cysteine residues.

Many TNF receptors are S-palmitoylated at an intracellular membrane proximal cysteine, e.g. death receptor 6 [41]. Also CD95 is palmitoylated at this site, cysteine 199. This palmitoylation is required for the redistribution into lipid rafts, for a raft dependent cytoskeleton association and consecutive efficient cell death in Hek293T cells [42]. The same palmitoylation of cysteine 199 has been shown to be a pre-requisit for the formation of SDS-stable aggregates of CD95 the B-lymphoblastoid cell line SKW6.4 [38] (that can be found inside and outside the detergent resistant membranes). Cysteine 199 mutants no longer form SDS-stable aggregates [38].

In death receptor 6 it was shown that palmitoylation did not play an essential role in lipid raft targeting [41], therefore other targeting mechanisms such as extracellular glycosphingolipid binding motifs were proposed.

**Glycosylation** can affect the folding, trafficking , localization and function in the receptors of the TNFR family [41]. E.g. glycosylation of death receptor 6 is required for the localization to the plasma membrane. Effects on lipid raft targeting and ligand binding remain unresolved [41]. CD95 receptor can be glycosylated at sites N136 and N118, however this does not play a major role in DISC formation and signal

transduction, neither in the formation of CD95 high molecular weight structures [43].

One observation is the formation of SDS- and  $\beta$ -mercapto-ethanol stable aggregates of high molecular weight after induction [36] (after crosslinking with antibody in HuT78 cells), [7], [44]. These microaggregates in SKW 6.4 cells are found both inside and outside of detergent-resistant membranes.

### 1.3. Regulation Mechanisms

The decision between life and death is fatal and therefore regulation of apoptosis is multifaceted and has several independent influences [45].

In 2002 the early signaling events of CD95 in type I cells were described in detail [35]: these are formation of microaggregates, actin-dependent FADD recruitment and later receptor internalization. In a further study on type I cells (SKW 6.4 and H9) the same steps were observed, and especially the mechanism of palmitoylation was further elucidated with biochemical techniques, connecting the events to lipid raft localization and caspase 8 activation [38].

These examples in particular cell types show the importance of mechanisms as lipid raft localization, actin cytoskeleton dependence, internalization and clustering for the regulation of CD95-mediated apoptosis.

#### 1.3.1. The Role of Lipid Rafts in Type I and Type II cells

Lipid rafts and detergent resistant domains can be defined according to different methods, so that statements of findings need to be done cautiously.

Muppidi and Siegel [46] showed that redistribution of CD95 into lipid rafts is an important mechanism to mediate clonotypic cell death of activated T cells. Using density gradient fractionation it was shown that in type I cells CD95 relocalization into lipid rafts makes the cells sensitive to CD95-mediated apoptosis. In type II cells apoptosis appears to be independent of lipid rafts.

Gajate and Mollinedo [21], [22] showed that the ether lipid (Et-18-OCH<sub>3</sub>) induces the redistribution of Fas into the detergent resistant domains, again determined by sucrose gradient, which represents a self-sufficient step mediating a CD95-dependent apoptotic signal.

Legembre [47] used the membrane fractions of sucrose gradient ultracentrifugation (Triton X-100 cell lysate) to define raft and non-raft localization of the CD95 receptor. They

could show an amplification of CD95-mediated apoptosis in type II cells, that was caused by a recruitment of the receptor to the lipid rafts. The enhancement appears to be of the mitochondrial apoptotic pathway.

One mechanistic clue supporting redistribution of CD95 into lipid rafts is the palmitoylation of the cysteine 199 near the transmembrane region. It has been shown to be involved in the redistribution of the receptor into the lipid rafts in Hek293 cells (established by sucrose gradient studies), and seems to be a mandatory step in triggering efficient cell death signaling [42].

The formation of SDS-stable CD95 aggregates however was shown to involve palmitoylation of the membrane proximal cysteine 199 in CD95 and Cysteine 199 mutants no longer form SDS-stable aggregates [38].

In Jurkat cells ceramide depending capping, i.e. accumulation of the receptor in one large domain at the plasma membrane and subsequent apoptosis could be shown. This was abrogated by disruption of lipid rafts by cholesterol depletion with the disolvant  $\beta$ -cyclodextrin [48], [49]. However the role of ceramide increase as an activator or just as a response to CD95 activation is still not clear [3].

When inducing CD95-mediated apoptosis in Jurkat with the drug Aplidin, CD95 and many other apoptosis signaling molecules are recruited to lipid rafts (sucrose gradient ultracentrifugation of Triton X-100 cell lysate) [49]. This recruitment is crucial for the capping and subsequent apoptosis.

### 1.3.2. The Actin Cytoskeleton

The actin cytoskeleton can play two different roles in Apoptosis: inducing apoptosis or mediating apoptosis.

On one hand disruption of the actin cytoskeleton is a severe injury to the cell and thus can itself induced apoptosis [?]. This apoptosis involves CD95 and the effect is reduced in cells lacking CD95.

On the other hand studies on Jurkat, a T-cell line, observed a capping of CD95 with microscopy and enrichment of various apoptosis related proteins in lipid rafts. When actin cytoskeleton is disrupted with cytochalasin B or with jasplakinolide no more capping and recruitment to lipid rafts can be observed, indicating a major importance of the actin cytoskeleton in cap formation [49].

Again in T-lymphocytes (CD4<sup>+</sup> cells) after induction CD95 colocalizes with ezrin, a protein that links the actin cytoskeleton to the plasma membrane. Ezrin-inhibition protects

from CD95-mediated apoptosis, showing that association to actin cytoskeleton is key mechanism "in rendering human T lymphocytes susceptible to the CD-mediated apoptosis" [50].

### 1.3.3. The Role of Receptor Internalization

The role of receptor internalization on signaling was studied in detail on type I cells. A general requirement of receptor internalization for CD95-mediated cell death was shown, where DISC components occurs only after receptor internalization in the cytosol and inhibition of internalization impairs DISC formation and apoptosis [51].

Recent findings reveal a role for receptor internalization and endosomal trafficking in selectively transmitting the signals that lead either to apoptosis or to the survival of the cell [52].

The mechanisms lipid raft localization, actin cytoskeleton association and receptor internalization all follow the same mechanism of regulating signaling by localization in subcellular compartments. Thereby receptor accumulation is achieved that serves signaling by providing the high local caspase 8 concentrations that are needed for auto processing of the enzyme. The role of the mechanisms can not be defined universally but seem to be highly dependent on cell type.

### 1.3.4. Receptor Oligomerization on the Plasma Membrane before Induction

There are many reasons to assume that spacial organization of CD95 on the plasma membrane and its oligomerization status regulates apoptosis. It is known, that procaspase 8 upon dimerization can be auto processed to become an active caspase. This needs high local concentrations, that can be favored by the spacial organization and clustering of the DISC.

Often the receptor was assumed to be trimeric [53], but stringent evidence is still lacking. There are various hypotheses and analysis with different methods that reveal the importance of receptor organization before and after induction.

Historically for TNF receptors a so called ligand induced trimerization model was proposed. The receptor before induction is monomeric on the plasma membrane and is trimerized upon induction by a trimeric ligand. The model was supported by solution and crystallography studies, that showed a three to three ratio of ligand and receptor [9]. In this trimeric structure the ligand chains are located between the receptor chains. By analogy for long time CD95 was assumed to follow the ligand trimerization model.

### Pre-Ligand-Assembly

However there are reasons, that speak for a different ordering. E.g. TNF $\alpha$  can bind to both TNF-R1 and TNF-R2. A ligand induced trimerization could easily generate hetero-receptor trimers, but only homotrimers are observed in experiments [54].

The promiscuous nature of binding of TNF $\alpha$  speaks for a pre-ordering of TNF receptors. Similar considerations hold true for CD95, when studying the autoimmune diseases ALPS (Autoimmune Lymphoproliferative Syndrome): in these diseases CD95 is mutated or even truncated at the extracellular part. Interestingly these non-inducing receptors can dominantly interfere with the full length CD95 and disrupt apoptosis signaling. Even non-ligand binding receptors could interfere, speaking for a pre-ligand assembly [18] that was shown in H9 T lymphoma cells and Hek293 T cells by fluorescence energy transfer microscopy (FRET).

There is molecular evidence for this receptor assembly: the pre-ligand assembly domain (PLAD) is a highly conserved domain at the extracellular end of most TNF receptors including CD95. Using biochemical assays it was shown in Hek293T cells that the PLAD domain is responsible for pre-association of TNF receptors [17]. For CD95 this same function of the PLAD domain could be shown, when PLAD was deleted in the ALPS mutations, leading to a loss of the dominant interference related to a loss of the receptor association [18].

### Is CD95 trimeric?

By analogy to TRAIL and also considering studies of a soluble form [55], CD95 ligand assumed to be a trimer [3] and also in our laboratory Clarissa Liesche provided stringent evidence for a trimeric structure of the ligand (data not shown).

In lack of other evidence CD95 was often assumed to be trimeric [53], [56], [3]. However this analogy to the ligand is not stringent and directly transferrable.

[57] show on purified protein that TNF- $\alpha$  and TNF- $\beta$  may intrinsically be polydisperse. The study implies, that the "trimer formation is a dynamic process and, with decreasing protein concentration, the trimer decays to dimers and monomers". Crystallographic structure analysis of TNFR-1 show, that the receptor before induction is a dimer [58] and likewise other TNF-receptor family members CD27 and CD40 have been shown to be dimers through intermolecular disulfide bonds [54], while crystallographic studies show a trimer to trimer stoichiometry for TRAIL-R2 and BAFF-R3 [59] of the extracellular receptor domain to the ligand.

It has not yet been possible to crystallize the whole CD95 receptor but only single domains, thus structural findings rely on analogy to other TNF receptors, mainly TRAIL [59] especially for receptors without induction.

The current model for receptor oligomerization assumes a pre-ligand assembly, however

most evidence for this derives from experiments with high receptor concentrations.

### 1.3.5. Receptor Oligomerization after Induction

In type II cells formation of SDS-stable microaggregates and clusters visible by microscopy were observed after induction. There are various hypothesis and studies, that investigated the role of receptor oligomerization after induction.

Another reasoning that speaks for receptor oligomerization is that procaspase 8 essentially needs to dimerize to be activated. Among other possibilities, such as chain formation [56], the formation of hexamers or higher aggregation of the receptor and DISC gives a simple manner to effectively translate from a trimeric structure of the ligand to such a dimeric caspase structure.

### Ligand induced Trimerization

It has been shown for  $\text{TNF}\alpha$  and  $\text{LT}\alpha$  that the ligands form trimers [60] and upon induction form a trimeric complex with the respective receptor (Ligand induced trimerization) [54].

The soluble form of CD95 ligand is a trimer [3], (Laboratory data by Clarissa Liesche). Considering structural aspects by analogy to  $\text{TNF}\alpha$  the membrane bound form of CD95L is considered a trimeric as well [60]. "It seems likely, therefore, that all ligands in this family adopt a similar tertiary structure and form oligomers" Based on this analogy it is further suggested that every CD95L-trimer binds three CD95 receptors, while DD-interaction leads to clustering in analogy to the ligand induced trimerization of other TNF-receptors [12].

### Clustering via CD95 Death Domains or FADD

Nuclear magnetic resonance structure of the CD95 death domains [61] suggests that CD95 is clustered via DD [61]. Two different interaction modes for death domains (DD) have been recently detected. The structure of a complex of CD95-DD and FADD-DD under acidic conditions reveals a four to four stoichiometry [62]. However in a more recent study the complex showed to form an asymmetric oligomeric structure composed of 5-7 CD95-DD and 5 FADD-DD [63], "which suggests that the CD95/FADD structure solved under acidic conditions does not represent the physiological structure in solution" [64].

Muppidi measured self-association of the downstream molecule FADD by fluorescence energy transfer microscopy. It was shown, that this self-association occurs via a motif in the death effector domain (DED) of the molecule and FRET in mutants lacking the DED. Also the self association of FADD was essential for CD95-mediated apoptosis in Jurkat cells [65].

Using a FADD-GFP stable clone I could observe clustering of FADD upon induction in our laboratory using total internal reflection microscopy (TIRF) kindly provided by the Nikon Imaging Center der Universität Heidelberg, Figure 1.4.

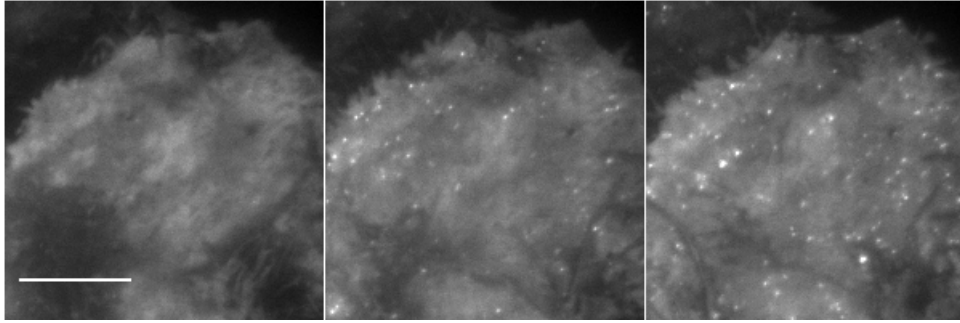


**Figure 1.4.:** FADD crosslinks after induction visible with background reduced microscopy: HeLa stably expressing FADD-mGFP induced with ILZ-sCD95L were imaged with total internal reflection microscopy (TIRF). This method was chosen to reduce background of the cytosolic FADD-mGFP and image only the region of the lower plasma membrane. Time-lapse microscopy. Left: before induction. Middle: 30 min after induction. Right: 55 min after induction. Scale bar: 5  $\mu\text{m}$ .

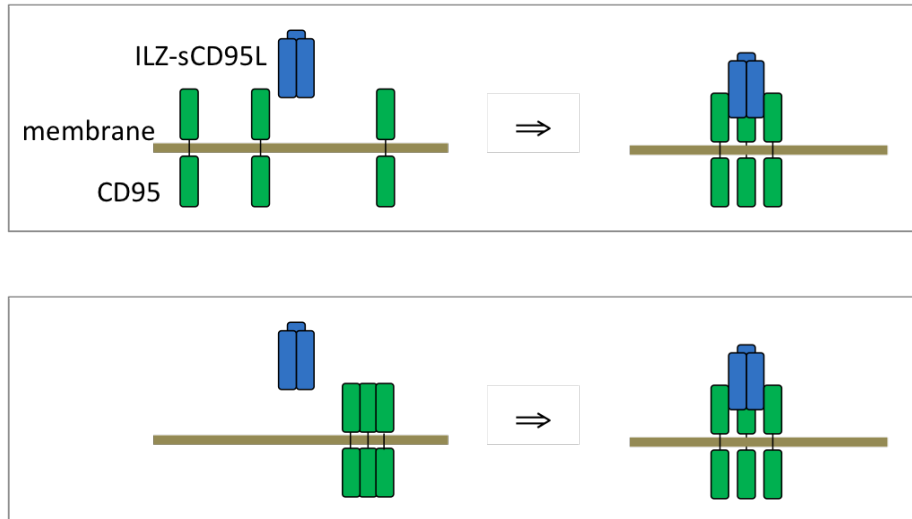
All these findings provide more insight on mechanisms and possible stoichiometry of oligomerization and clustering, however evidence for oligomerization levels at physiological conditions on the surface of living cells before and after induction is still lacking.



### 1.3.6. Models of CD95 Oligomerization Mechanisms

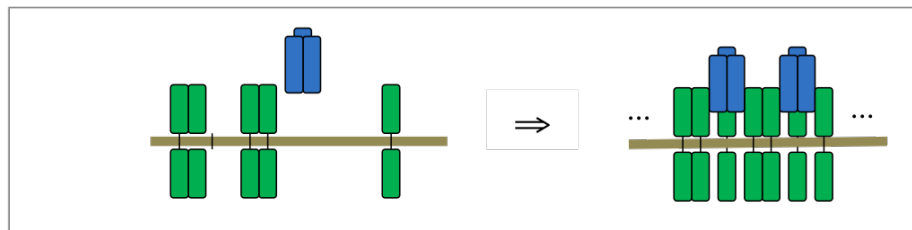
All these regulation mechanisms can be summarized into four different and not exclusive models for receptor organization and the oligomerization level before and after induction:

#### Ligand induced receptor trimerization



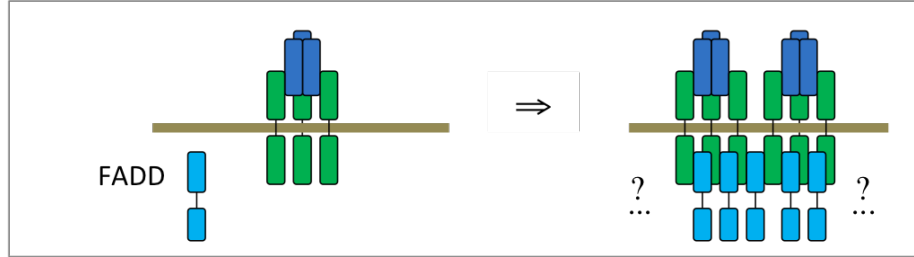
This model is mainly supported by analogy to crystallographic data for TNFR-1 and TNF $\beta$  complex. The ligand binds to exactly three oligomerization sites inside a receptor trimer, therefore the stoichiometry ligand receptor is three to three and no higher oligomers or aggregates form from the ligand receptor interaction.

#### Ligand induced oligomerization of pre assembled receptor



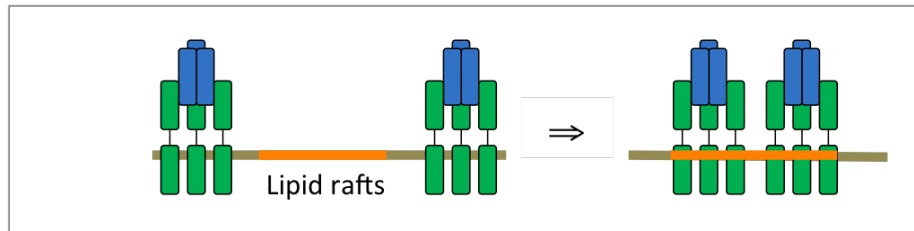
This model assumes that the receptor is not monomeric before induction, but assembled into oligomers via a pre-ligand assembly domain. This is one way to allow for a further oligomerization than three after induction.

### Ligand and FADD induced receptor oligomerization



This model assumes that a clustering after induction stems from self-association of the death domains of the downstream protein FADD [10].

### Translocation of induced receptors to lipid rafts



This model assumes a translocation of induced receptors to lipid rafts to be the reason for receptor clustering after induction.

In this thesis I present my work on CD95 receptor clustering and signaling using microscopy methods to characterize receptor distribution and behavior on plasma membrane based on these four not exclusive models for receptor clustering and the underlying mechanisms.

## 2. Microscopy Approaches to Characterize Receptors at Single Cell Level

In this work I investigated CD95 clustering using microscopy methods. Though CD95-mediated apoptosis signaling and accompanying mechanisms have been already studied intensively, many questions remain open also due to a high variation of occurring mechanisms depending on cell type. The receptor oligomerization level on the plasma membrane before and after induction is not yet precisely estimated and no clear model is yet verified, even though lots of studies indicate the importance of receptor organization for apoptosis sensitivity. Most studies were performed in overexpression conditions using biochemical methods and lysates or purified receptor for NMR studies. Evidence in living cells on the plasma membrane at physiological expression levels is still rare.

The goal of this work is to characterize the receptor and its clustering in living cells, aiming for high resolution in order to separate single receptors on the plasma membrane. One main target was to quantify receptor amount and its oligomerization levels before and after induction. To complement the existing knowledge, the distribution at high but also at physiological expression in living cells was explored. A more indirect characterization of the receptor on the plasma membrane was performed measuring its dynamics before and after induction to conclude on clustering and its mechanisms.

### 2.1. Confocal Microscopy

In the year 1675 a man named Anton van Leeuwenhoek for the first time caught a glimpse to a new world. With a microscope he studied water from a nearby pond and discovered thousands of tiny creatures, that no one had ever seen before.

Without knowing Leeuwenhoek made way for a new age in the studies of nature. To us may seem simple, but the germ theory itself could save thousands of lives by simple hygienic measures and vaccines. Still this very day microscopy is one of the most important techniques in modern cell and molecular biology, because contrary to other techniques it allows the observation of processes and mechanisms in living organisms.

New stains and the specific creation and use of antibodies or chemical tags, allow for a specific staining of nearly all parts of cells and organisms. The finding of fluorescent proteins e.g. the green fluorescent protein (GFP) in the 1960s and cloning in 1990s expands massively the research possibilities. But also microscopy itself is still massively explored and expanded: confocal microscopy enables three dimensional imaging of cells. Fast scanning techniques such as spinning disc increase time resolution. Photophysical properties of dyes allow for pH-measurement and molecular dynamics like dimerization. Bleaching techniques can be used for diffusion and dynamics measurements and detailed quantification is made possible by single molecule techniques. In the last decades high resolution techniques such as Stimulated emission depletion (STED),  $2\pi$ -microscopy, photoactivated localization microscopy (PALM) and stochastic optical reconstruction (STORM) expand research possibilities to the nanometer scale. A wonderful example of modern microscopy

is the mapping of all cells during zebrafish embryogenesis and its development of the vertebrate by light sheet microscopy performed by Philipp J. Keller et al. in 2008 [66]. <http://www.youtube.com/watch?v=3xh441Wdv84>

### 2.1.1. Fluorescence Microscopy

Since most microorganisms are transparent, it is necessary to increase the contrast of single observed parts of the cells. There are device-related possibilities, such as dark field of phase contrast, for parts with different optical density. Most of the times however fluorescence is used to increase contrast.

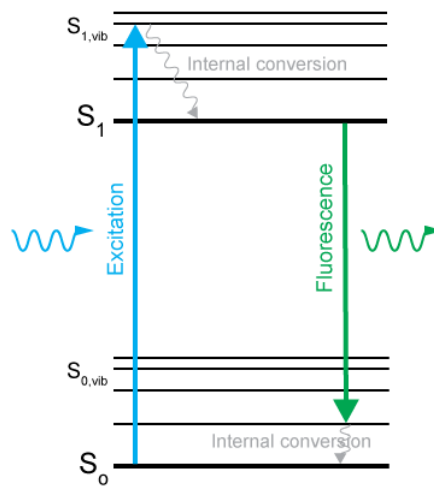


**Figure 2.1.:** Principle of fluorescence depicted on a Jablonski diagram: Molecules are lifted from the ground state  $S_0$  to an excited state  $S_1$  by excitation light. Vibrations result in little loss of energy (internal conversion). Then the molecule relaxes back to the ground state by emitting a photon (fluorescence) of a little less energy, than the excitation light.

Fluorescence is a photophysical property of particular molecules: These molecules have different energy states that can be depicted in a Jablonski diagram such as Figure 2.1. Fluorescence occurs, when the molecule is excited to energy level  $S_2$  by absorbing light of the energy  $S_2 - S_0$ , then loses some energy through vibration relaxations and then from a lower energy level  $S_1$  relaxes to  $S_0$  by emitting a photon, with lower energy (and higher wave length) than the exciting light.

Fluorescent molecules can effectively be used to stain biological samples for microscopy. To image one uses fluorescent microscopes, that detect only the fluorescent light: the

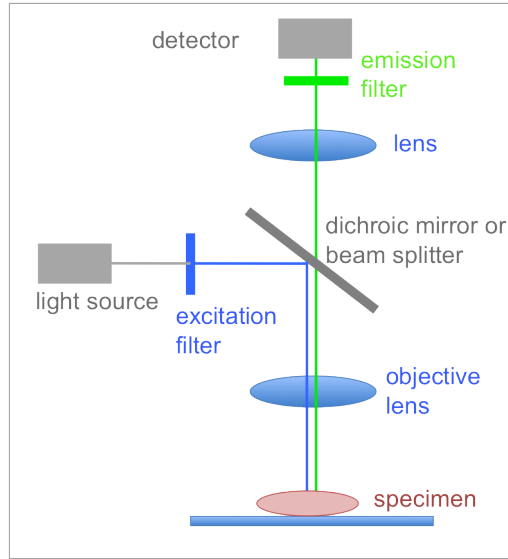


**Figure 2.2.:** Setup of a fluorescent microscope: the specimen is illuminated (e.g. with laser beam) of the excitation frequency of the observed molecules. These then emit fluorescent light of slightly higher wave length (lower energy). The incoming (excitation) beam and the outgoing (fluorescent) light are separated by a beam splitter of dicroic mirror. The emission filter refines the light beam before reaching the detector.

principle is easy. The incident excitation beam if necessary is filtered to the optimal wavelength by an excitation filter to illuminate the object. To direct the emitted light to the detector, the path of incident and emitted beam have to be separated either by a simple beam splitter, or a dichroic mirror that reflects or lets light pass according to the wavelength. The emission filter lets pass only the light from the emission spectrum of the fluorophor, so noise signal of any other wave length (especially reflexions from the strong excitation beam) are filtered out.

### 2.1.2. Laser Scanning Confocal Microscopy

The confocal principle was first described by Minsky in 1957 , however it did not become known and used until 1988, when scanning techniques were elaborated enough to allow for a good reconstruction of the image.

The principle of confocal microscopy [67], [68] is as simple as striking: The main idea is to use the light from the plain that is in focus and exclude out of focus blur. This is implemented by illuminating the sample through a pinhole, while another pinhole is placed in the plain of the virtual image in front of the detector. It is placed so that it lets pass only light from exactly the one illuminated point of the in focus object, while all light from

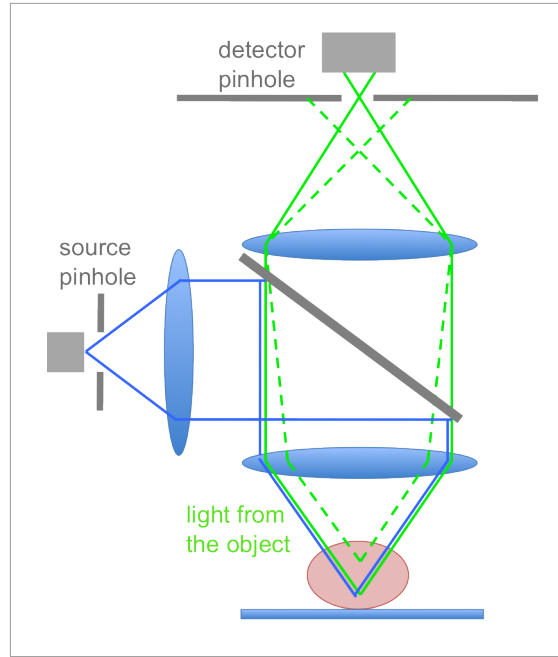


**Figure 2.3.:** The confocal principle: the setup of a laser scanning fluorescent confocal microscope is based on fluorescent microscopy setups, the pinhole filters out light from other layers than the layer in focus, therefore 3D imaging is possible.

other points of the plain or other out of focus plains is debarred as depicted in Figure 2.3.

To obtain a complete image, the points of the object are scanned one after the other and then composed together to a virtual image. By scanning the other plains, it is possible to get a 3D image of the observed object.

Due to the scanning technique there is no camera required, therefore photon multipliers (PMT) or even more light sensitive avalanche photo diodes (APD) are used as detectors. With the pinhole size it is possible to regulate the thickness of the plain from which light is still detected: the bigger the pinhole, the more light from different plains can reach the detector, with this the image becomes brighter but resolution in the vertical direction (z-direction) is decreased. For pinholes about the size of an Airy Disc, z-resolutions up to 300 nm can be reached.

### 2.1.3. Spinning Disc Confocal Microscopy

For big objects, the scanning process takes time, decreasing possible time resolution. Therefore came up the idea of scanning with 1000 pinholes at some distance at the same time. These 1000 pinholes are installed on a disc, that can rotate to scan the object, therefore called Spinning Disc. To allow for this, physically the same pinhole is used for incoming and outgoing light, therefore the dichroic is also integrated in the disc. Additionally the incoming laser is focussed on the pinholes for each with a little lens also placed on second disc, the microlens Disc, that moves together with the pinhole disc. Detection can not be done with one photomultiplier, but has to be carried out with a camera, to resolve the signal form the single pinholes separately. The camera also allows for a much higher light sensitivity than PMT detectors.

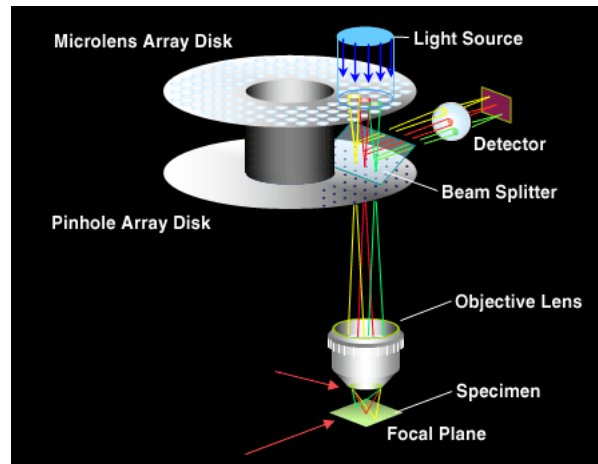


**Figure 2.4.:** The Spinning Disc is a method to accelerate scanning using 1000 pinholes at a time. The pinholes serve as source pinhole and detector pinhole at the same time. They are placed on a Disc, where the respective microlenses are arranged to focus the laser beam onto the pinholes and the beam splitter is included to separate incoming from outgoing light. (3i intelligent imaging innovations)

### 2.1.4. Signal Quantification and Signal Disturbances

My objective was to characterize receptor distribution, determining numbers of receptors and oligomerization levels, therefore one main goal was to quantify signal and related to receptor amounts. When using fusion proteins but also with antibody staining, the receptor amount is proportional to the fluorophor amount, which in turn (upon equal illumination) directly corresponds to the measured light intensity. Therefore intensity values can directly be used for quantification of receptors. When using equal staining techniques these intensities can be calibrated and thus receptor numbers counted.



In every microscope image there are disturbances that cause measurement errors. There are two main error sources: background and noise, that can be traced back to different sources of origin.

The background has a positive intensity value and is generated for example by autofluorescence of cells, unspecific signal, surrounding light and light reflexion on the glass. On the other hand noise is a measurement error on every single pixel of the image. It originates for example from the detector e.g. from the PMT or the camera from the amplification and read or as dark noise or the variation of the photons themselves, the so called shot noise.

When acquiring images, one should try to reduce these sources of error of cause considering other features of the measurement such as time and spacial resolution, bleaching and photo toxicity. Noise can be decreased relatively by acquiring more signal, e.g. if possible with longer integration times, stronger illumination and stronger fluorescent dyes.

However there are also image processing techniques for reducing these sources of error: Depending on the research question in cellular biology the background can be determined locally (e.g. on a position inside the cell) or globally (a position outside the cell) and then be subtracted from the image.

The distribution of the noise, that comes from the surroundings can be determined, but since it is randomly distributed on every pixel, one can not subtract it from the image like the background. However since the noise of different pixels is independent (high spacial frequency), while the signal mostly correlated over many pixels, smoothing (e.g. with a Gaussian kernel or low pass filter) can reduce the noise. A similar method, when the question allows for lower resolutions, is the merging of neighboring pixels, so called binning, which reduces noise compared to signal.

The shot noise on the other hand is a physical property of light itself. It is named after Walter Schottky, who discovered it on electric currents in vacuum tubes, but his findings hold true the same for photons of fluorescent signal. Contrary to the other sources that cause a constant noise, the shot noise is a statistic variation light intensity and therefore is dependent on the amplitude of the signal itself.

$$N_{\text{shot}} = \sqrt{\text{number of photons}}$$

Other error sources lie in the features of fluorescent dyes themselves: bleaching and blinking of the fluorescent dyes, quenching e.g. by chemical substances (GFP is quenched in the endosomal compartment of cells) but also uneven distribution of fluorescent dyes on the observed molecules can lead to errors in the observation of biological processes.

### 2.1.5. The Limit of Resolution

Microscopes are used to increase the resolution of objects that are not within the resolution of the normal eye. My goal was to observe single receptors on the plasma membrane of cells. The resolution plays a key role to separate receptors and high resolution allows for monitoring of clustering. However resolution is limited not only technically (by aberrations of the microscope) but particularly on a principle level by the diffraction of the light by the optical aperture. Even with a perfectly built aperture a point-shaped light source will appear as a small disc, called Airy Disc, caused by the diffraction of light. It can be described by the square of a Bessel-function, however the gaussian function represents a good approximation 2.5.

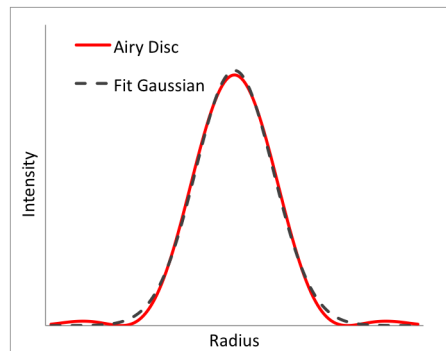


**Figure 2.5.:** The airy disc describes the intensity pattern, that results from diffraction when a point source is imaged. It can be theoretically describes as the square of a Bessel function (red) but very well approximated by fit to a gaussian function (black).

To define the resolution usually the Rayleigh criterium is used, which indicated that two near objects can still be resolved as two, when the minimum between the two maxima of the objects is 26% smaller than the maxima themselves. For a system that is limited only by the diffraction of light, the resolution therefore results as:

$$\text{resolution} = \frac{1.22\lambda}{2n \sin \theta} \quad (2.1)$$

where  $\lambda$  indicates the light's wave length,  $n$  is the refractive index of the medium and  $\sin \theta$  is the maximal angle of incidence achieve by the microscope objective. Ernst Abbe combined  $n \sin \theta$  to the physical variable NA. the numerical aperture, thereby postulating the Abbe diffraction limit:

$$\text{resolution} = \frac{0.61\lambda}{\text{NA}} \quad (2.2)$$

To increase the resolution one can thus optimize the variables in this equation. In modern microscopes numerical apertures up to 1.4 are achieved, by high angles and optically dense oil. Using light with small wavelength, e.g. UV-light, increases resolution, how-

ever one has to consider, that biological object might be massively damaged by such light.

The resolution in the vertical direction of a confocal microscope is limited to 600 nm. It is determined by the pinhole and can be increased by reducing pinhole size. This is however accompanied by a decrease in light, reducing the signal. In  $4\pi$ - microscopy the use of two objectives from both sample sides allows for duplication of the angle and therefore increases vertical resolution.

### The Point Spread Function

To characterize the features of optical systems however not always the resolution but rather a so called point spread function is used, which is defined as followed: Between the observed object and the virtual image there is the optics of the microscope, that generates aberration effects and the diffraction effects described by Abbe.

*The point spread function specifies as a direct function of space, how a point source will appear on the virtual image.*

With an optimal optical system, this corresponds well to the Airy Disc and can be approximated with a normal distribution (Gaussian function). To experimentally determine the point spread function of a microscope one has to acquire the image of a point like object, such as a fluorescent bead much smaller than resolution, e.g. 20 nm

### The Pixel Size and Sampling

As discussed earlier in Laser Scanning Microscopy objects are scanned point wise and then represented. Every point results into a pixel on the virtual image. This corresponds to a discretization on a continuous object, where the point distance corresponds to pixel size and has to be appointed reasonably. Since the image resolution is limited by the diffraction law, much higher pixel resolution is not necessary. Nyquist put this into a theorem stating:

**For a function with resolution  $d$  - meaning minimal frequencies of  $1/d$  - a sampling of  $d/2$  contains the maximal information.**

Therefore one should choose a pixel size  $d/2$  to achieve maximal resolution without over-sampling.

As I will show via simulations, that resolution has a key role in the imaging and quantification of receptors and oligomerization, therefore I performed high resolution microscopy in collaboration with Matthias Reuss.

## 2.2. Stimulated emission depletion

One limiting factor when observing receptor clustering microscopically is spatial resolution. Our goal is to separate receptors that randomly near, but still in the order of magnitude of 50 nm distance from receptors that cluster. For this, I collaborated with Matthias Reuss to perform high resolution microscopy.

One of the most important high resolution techniques is Stimulated Emission Depletion (STED) microscopy which was described and experimentally realized in the 90s by Stefan Hell [69]. The basic idea holds true for most super-resolution methods known today. It is to isolate dyes whose diffraction-limited images would normally overlap by switching them between a fluorescent bright and a non-fluorescent dark state sequentially. This way, they can be imaged one after another and thus be located separately. In contrast to high-resolution techniques such as PALM and STORM that rely on random switching and subsequent in-silico localization of individual emitters, STED is based on confocal laser scanning and localization is established in the sample itself. By keeping molecules at the periphery of the confocal excitation spot dark via stimulated emission, the area in which molecules are allowed to fluorescence is effectively shrunk and this way the resolution can be increased beyond the diffraction barrier.

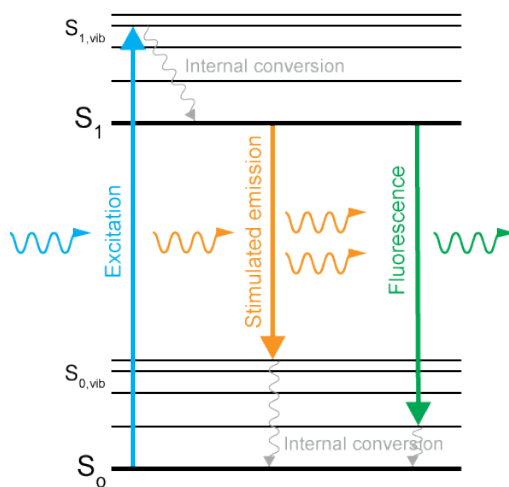


**Figure 2.6.:** The STED principle: Jablonski diagram of fluorophores, normally energy release occurs via emission of fluorescent light. In STED-microscopy molecules are relaxed by stimulated emission without emitting fluorescent light.

As depicted on the Jablonski diagram in Figure 2.6 excited fluorophores can release their energy by spontaneous relaxation, resulting in fluorescence. In STED this stimulated emission is enforced by irradiation with a depleting laser of a similar wave length to the exciting one.

To achieve a higher resolution the exciting laser is focused to a diffraction limited spot, Figure 2.7 (blue). The wavefront of the depletion laser is modified leading to a donut-like shape (red). The excited molecules only fluoresce in the spot (green), where they are not depleted.

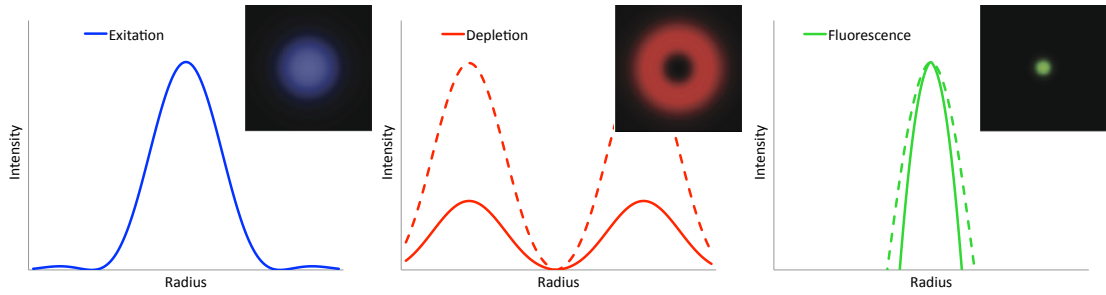


**Figure 2.7.:** Shape [70] and intensity profile of exciting and depleting laser result in a highly resolved fluorescent spot. When the depleting laser power is increased, higher resolution is achieved (dotted lines).

By increasing laser power of the depleting laser (dotted lines) more molecules are switched off as depicted in the intensity diagrams. The spot in which fluorophores are able to signal has a diameter of

$$d = \frac{\lambda}{2(NA)\sqrt{1 + I_m/I_{\text{sat}}}}$$

where  $I_m$  is the intensity of the depletion beam at its maximum and  $I_{\text{sat}}$  is the saturation intensity of the fluorescent molecule, a characteristic quantity normally in the range of  $1 \text{ MW/cm}^2$ . Outside this radius practically 95% of the molecules are switched off [71].

To achieve this resolution laser powers for the STED-laser are chosen in the range of  $200 \text{ MW/cm}^2$ . The high laser powers make alignment of the depletion laser crucial. Notably the intensity of the depletion laser in the centre of the donut, where molecules should give signal, needs to be set to 0, so that the wanted signal is not reduced. The depleting laser does not have the right wave length to bleach molecules directly, however the high energies can indirectly cause bleaching [71].

The STED setup is essentially a (confocal) laser scanning microscopy setup, where a second laser, the depleting laser is coupled in via a second dichroic mirror. A beam shaping device forms the characteristic donut shape of the depleting laser, Figure 2.8.

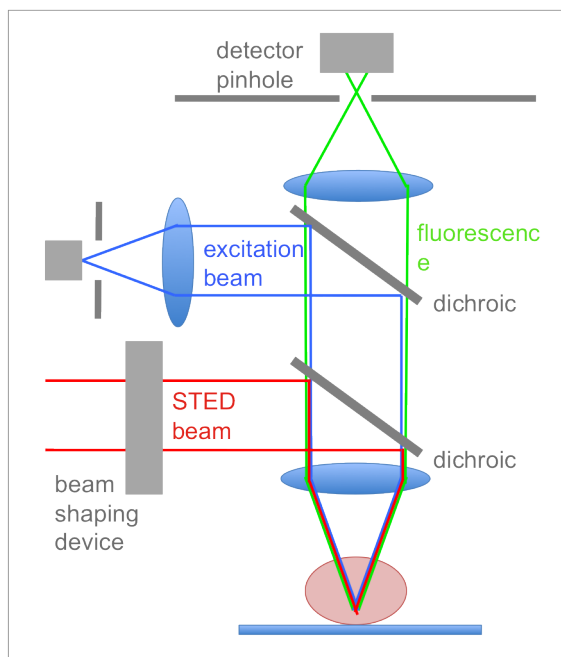


**Figure 2.8.:** STED setup: the setup essentially follows the setup of a (confocal) laser scanning microscope. With a second dichroic mirror the depleting laser is coupled into the light path. A beam shaping device forms the characteristic donut shape of the depleting laser. [72].

When molecules are continuously excited by a continuous wave laser (CW) a high number of molecules is continually in the excited state, from where they can cross over into a triplet state which is a known source for photo-bleaching. Therefore often pulsed exciting lasers are used. The depleting laser can be used in continuous wave modus or be pulsed as well and triggered to the exciting pulse with a adjustable time delay, in order to only illuminate the sample, when molecules are in the excited state.

### Point Spread Function

Contrary to the confocal systems the resolution is not determined by the optics of the microscope but by the switching off via depletion of molecules together with the fact that the location of the molecules that are allowed to remain in an on-state is established by the position of the donut-null, which in turn is positioned by the scanner. The point spread function that characterizes the resolution can for pulsed STED beams again be well approximated by a – now narrower – Gaussian function. However, incomplete switching, re-excitation or simply autofluorescence is often the cause for an additional pedestal of confocal width; then the true PSF is the sum of a confocal PSF with a Gaussian STED peak that can be approximated by a Lorentz function, Figure 2.9.

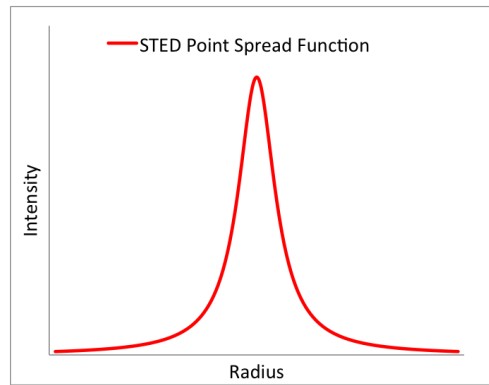


**Figure 2.9.:** The point spread function of STED microscopy is determined by the depletion of molecules next to the peak of resolution. The highly resolved peak and the characteristic basement around the peak is described by a Lorentz function.

STED is still developed further, aiming for simpler setups, where lasers are intrinsically aligned [73] and faster scanning setups [70], [74].

For the observation of receptor clustering resolution is a key issue and the high resolution techniques STED can give very far insights into receptor clustering. However protein dynamics measurements are more accessible and provide a robust instrument for observation of clustering also at very high receptor concentrations.

## 2.3. Protein Dynamics and Clustering

The naive idea of measuring clustering by dynamics is, that particles of bigger size should be diffusing slower and thus clustering should be possible to be diagnosed by a decrease in diffusion coefficient (a slowdown). Saffmann and Delbrueck focussed particularly on the differences between lateral diffusion in membranes and the more simple three dimensional diffusion in a bulk. Focussing on the CD95-receptor in the following I want to constrain to the case of a transmembrane proteins.

### 2.3.1. Diffusion Models

Theoretically the publication of Saffmann Delbrueck indicates a weak logarithmic dependency of the diffusion coefficient on the size of the protein [75]:

$$D \propto \ln(R) \quad (2.3)$$

$D$  represents the diffusion coefficient and  $R$  is the radius of the transmembrane protein in the plain of the membrane. The third dimension outside the membrane can be neglected.

For a long time theoretical approaches were based on this. However Gambin et. al. [76] have called into question this equation with experiments on artificial membranes. Considering literature data and their own experiments, they found that heuristically the dependency of the diffusion coefficient on the size can be described as a linearity in a Stokes-like expression.

$$D \propto \frac{1}{R} \quad (2.4)$$

Naji in 2007 [77] could theoretically support this finding arguing that "whenever the protein-lipid interactions locally deform the membrane, that deformation generates new hydrodynamic stresses on the protein-membrane complex leading to a suppression of its mobility." They suggest two effects and show that both theoretically lead to a  $D \propto 1/R$  scaling. One being enhanced dissipation associated with modifications of the flows in the solvent, the other being enhanced dissipation in the membrane itself, when local compositions, chain stretch or tilt order are changed. Guigas [78] modeled the effect of internal degrees of freedom of the included complex on the diffusion coefficient (not including upper membrane deviating) showing an effect of  $D \propto 1/R^2$ .

Therefore diffusion coefficients can be used to measure the oligomerization of transmembrane proteins. While the function of size is only very weak (logarithmic) for some particles and especially for lipid domains, for the majority of transmembrane proteins there could be shown a linearity like in 2.4 experimentally and theoretically accounted for.



Since there are no structural data for CD95, the transmembrane radius, and structure of interaction of CD95 can only be estimated, so that a measurement of the diffusion coefficient can only yield qualitative but no quantitative statements on oligomerization.

### 2.3.2. Membrane Models

There are different models for the composition of the plasma membrane and its influence on the diffusion of proteins:

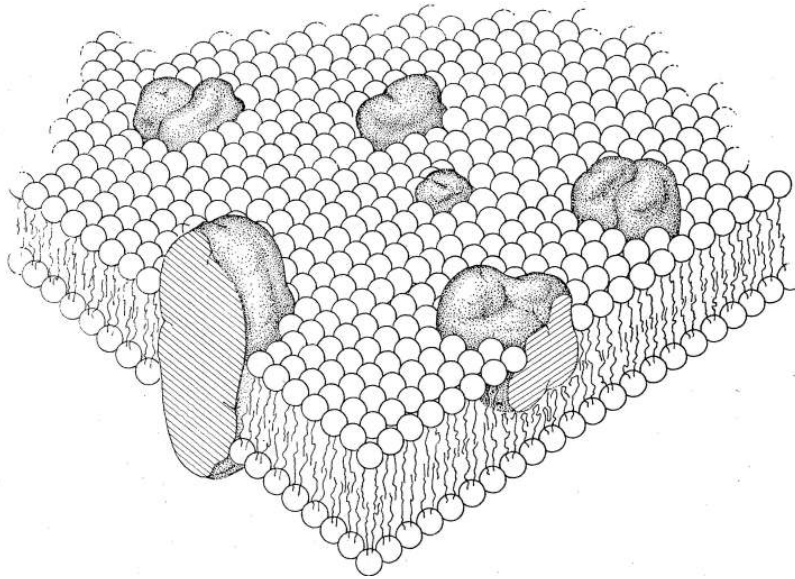


**Figure 2.10.:** Original figure from Singer and Nicolson (1972) depicting membrane cross section with integral proteins in the phospholipid bilayer mosaic. Phospholipids are depicted as spheres with tails, proteins as embedded shaded, globular objects. Peripheral proteins, which would be situated at, not in, the membrane surface, are not shown. Transmembrane protein spanning entire membrane on left.

The simplest model is the fluid mosaic model of Singer and Nicolson [79]: which assumes a laterally homogeneous lipid membrane. The associated proteins can diffuse freely with Brownian motion in the plain following the findings of Saffman and Delbrueck described earlier [75]. However in the real cell plasma membrane protein diffusion becomes sometimes anomalous [80]. Also diffusion coefficients are much lower than in artificial membranes [81]. There are various reasonings to explain this slowdown. Retardation is possibly due to protein protein interactions active transport, cytoskeleton interactions and confinement and membrane lipid microdomains [82].

Therefore the diffusion coefficient  $D$  may differ between short distances (e.g. in a raft or within a mesh of the cytoskeleton) and long distances, covering many rafts or scaffolds. Different measurement techniques for the diffusion coefficient therefore provide local or global values. Fluorescence correlation spectroscopy (FCS) measures local values, while fluorescence recovery after photobleaching (FRAP) can also be set up for long distance measurements of diffusion. [83] gives a good review on the differences between many of these techniques and the insights to the structure of the plasma membrane achieved with diffusion measurements.

### 2.4. Fluorescence Recovery after Photobleaching

In the 70s biologists started using fluorescence photobleaching recovery as a tool to study localization and dynamics of biomolecules. In the experiment locally a small part of fluorescent molecules, that are to be observed, is irreversibly bleached and the redistribution of the unbleached molecules is observed. There are several reviews that cover the different methods and the applications of FRAP: Reviews: [84], [85], [86].

With this method already various interesting discoveries could be made regarding localization and dynamics of proteins and also interaction with other components in living (in vivo) cells [84].

The fact, that in many cell compartments molecules diffuse freely and are not bound, could only be shown by FRAP - e.g. in the mitochondrial matrix [87], in the nucleus [88], in the cytoplasm, in the ER-lumen [89] and in the ER- and Golgi membranes [90]. While previous considerations and studies "suggest that the mitochondrial matrix, if it is indeed a crowded protein solution, would severely hinder solute diffusion" Partikian et. al. could show with FRAP experiments, that this hindrance "relatively mild" and proteins can diffuse nearly as freely in the matrix as in aqueous solution [87].

Also the retention of proteins in the ER and Golgi is not achieved by immobilization [90]. The transport of proteins through membrane trafficking pathways could be studied in detail revealing: "protein traffic through the various compartments of the secretory pathway" "compartment residence times and rate constants" for delivery from ER into Golgi and to plasma membrane transport mechanisms [91][92] but also behavior during mitosis [93].

But not only mechanisms of long range directed and diffusive transport could be studied, also the study of dynamics of proteins in one compartment can bring insights on cellular mechanisms. Notably mobility measurements of cell surface-proteins, with altered mobile fraction can illustrate interaction with cytoskeleton element of the extracellular

matrix. A list of biological processes, that have been studied with FRAP is displayed in table 2.1. One has to carefully consider, which are the driving forces of movement of the fluorescent molecules and which are the conditions of the experiment in order to chose the right experimental and analysis method for FRAP.

diffusion coefficients in cellular compartments or on membranes: free movement, hindered diffusion	[84] [87] [94] [90] [89] [88]
anomalous diffusion	[95]
directed movement such as flow	[96]
interaction with other cellular components: e.g. other proteins, cytoskeleton, extracellular matrix	[84]
binding rates: e.g. to the plasma membrane	[97]
conformational changes	[84]
exchange of labeled proteins between compartments: e.g. protein trafficking	[91][92][90]

**Table 2.1.:** List of protein and cell features, that can be studied by dynamics measurement, notably fluorescence recovery after photobleaching (FRAP)

Part II.

Materials and Methods

### 3. Materials and Methods

### 3.1. Chemicals, Antibodies, Stable Cell Lines

#### Cell culture

HeLa cells and all deriving clones were maintained in DMEM (GIBCO, Ref. 11960-044 500ml, 444689, 1056) with 10 % fetal calf serum (Gibco-BRL) in 5 % CO<sub>2</sub>, L-Glutamine at 1% (Invitrogen) and Penicillin/Streptavidin at 1% (MERCK)

#### Antibodies

**Fas (human), mAb (APO-1-3)** anti CD95 mouse antibody, IgG<sub>3</sub>, Enzo life sciences, Lausen Switzerland, 1 mg/mL, monoclonal

**Fas (human, mAb (APO-1-1)** anti CD95 mouse antibody, IgG<sub>1</sub>, Celonie GmbH monoclonal mouse antibody, not agonistic to CD95, 1 mg/mL, mono-clonal

**Alexa Fluor 488 Goat Anti-Mouse IgG (H+L)** anti mouse antibody, IgG (heavy and light chain), Molecular Probes (Invitrogen), 1 mg/mL, polyclonal

**Anti-Mouse-IgG - Atto 647N antibody produced in goat** anti mouse antibody, IgG, SIGMA (50185), 0.8 mg/mL, polyclonal

#### Transfection

Transfection of the different constructs was obtained with FuGene (R 6 Transfection Reagent, Roche) following the protocol. To allow localization of the receptor from the endoplasmic reticulum to the plasma membrane, experiments were performed two to four days after transfection.

#### Fibronectin-coating on microscopy chambers

For live cell microscopy Labtek chambers (8-well) were used. To achieve a flat attachment of cells on the glass, chamber were coated with fibronectin. Every well was incubated with 50 µL Fibronectin at concentration 1 mg/mL for 1 h, solution was removed with a pipet and the chamber kept at 37°C until use.

## Constructs

### shRNA-knockdown (2157)

GATCC AGCGT ATGAC ACATT GATTC TCAAG AGAAA TCAAT GTGTC ATACG  
CTTCT TTTT GGAAA

The shRNA against CD95 (coding sequence within the death domain) was cloned in pSilencer3.1-neo and stably expressed in HeLa cells (as later described). The shRNA is combined with a resistance against G418.

In the case where full length receptors were expressed in the stable knockdown cell line, we used a mutant form that minimizes the recognition of the shRNA while conserving the amino acid sequence.

The following receptor constructs were all expressed under the CMV-promoter.

Fluorescent proteins were fused to the C-terminal, intracellular part, of the receptor with the linker GGGGGPVAT.

The numbering used in the following, represents the receptor in a full length coding including the signal peptide.

### CD95-wt-mGFP (1127)

Wild type receptor fused to mGFP, a form of GFP, that minimizes dimerization.

### CD95-C199V-mGFP (1208)

In this construct a cystein in the intracellular part of the receptor (between death domain and transmembrane domain) is mutated into a valin. According to Chakrabandhu et al. [42] this cystein serves as a palmitoylation site and palmitoylation is inhibited in the mutant.

### CD95- $\Delta$ (210-335) (1208)

This construct is a receptor lacking the death domain (nucleotid 210-335) in the intracellular part of the receptor. Therefore it can not recruit FADD after induction. The CD95-knockdown shRNA does not affect expression of this mutant, since it is directed against the lacking domain.

## Stable clones

Stable clones were produced by transfecting HeLa cells with the vector (1-2 µg) containing the protein of interest (or shRNA) and a resistance to either puromycin or G418. Three days later transfected cells are incubated with medium containing the respective antibioticum (G418 at 0.8-1.2 mg/mL, puromycin at 1-2 µg/mL) to start the selection process for those cells that were transfected by the vector and therefore are resistant to the antibioticum. When 100% of the control cells are dead, the resistant cells are highly diluted and single cells are selected (e.g. by plating at low concentration into 96-well plates, leading to one cell per well). Single cells are now maintained (and let propagate) to yield a population of one single clone. The clones are then tested, e.g. by measuring the content of protein of interest or the function of the protein of interest, to choose the clones with the desired features.

### CD95-hE (high expression levels)

Stable HeLa clone (produced by Joël Beaudouin in the laboratory) that expresses CD95 at high expression levels of 200.000 receptor per cell, chapter 4.1.2. Puromycin-resistant.  
*Laboratory name: Apo-#12*

### CD95-GFP-hE (high expression levels)

Stable HeLa clone produced by Joël Beaudouin in our laboratory that expresses CD95-GFP at high expression levels of 140.000 receptors per cell, chapter 4.1.2. G418-resistant.  
*Laboratory name: Apo-mGFP-#1*

### CD95-kd

For production of the stable knockdown HeLa cells were transfected with shRNA (2157) and knockdown effect was verified by measurement of number of receptors. Figure 3.1 shows the histograms of the flow cytometry measurement of HeLa, the CD95-hE clone, the transiently transfected knockdown cells and control cells. The transfected cells show nicely two peaks, one peak of cells, that integrated the shRNA and therefore have a lower amount of receptors than HeLa, the other peak of cells that did not integrate the shRNA therefore coincides with non-transfected HeLa.

The knockdown cells were selected with G418 and clones chosen as described above. The clones were then again tested for amount of receptor by flow cytometry and percentage of cell death after three hours with high concentrations of ILZ-sCD95 was established, counting by eye, Figure 3.2. The clone used for further experiments was the one indicated with number 2.

*Laboratory name: kd-#21*



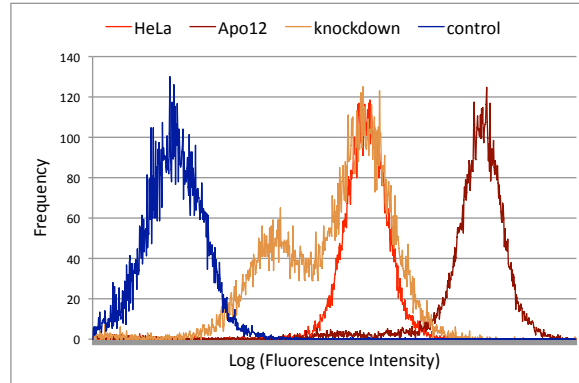


**Figure 3.1.:** Flow cytometry measurement of transiently transfected knockdown cells. The transiently transfected cells show two peaks. The left peak are cells that integrated the shRNA and therefore have less receptors. The right peak are the cells, that did not integrate the shRNA and therefore have the same amount of receptors as non-transfected HeLa cells.

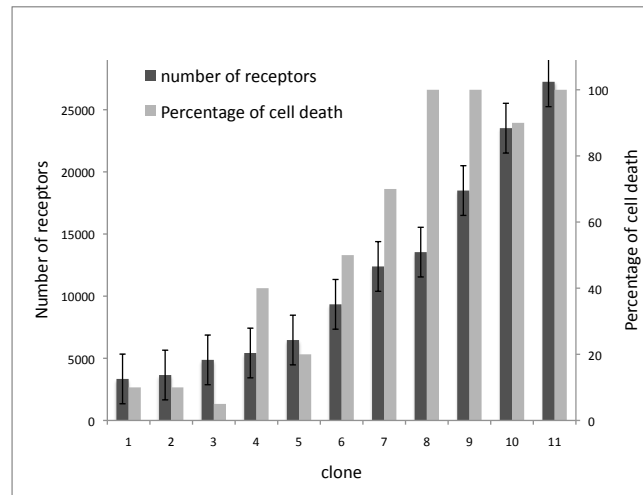


**Figure 3.2.:** Characteristics of stable knockdown clones. The number of receptors on the cell surface was determined by calibrated flow cytometry as described in chapter 3.3. The percentage of cell death was determined visually after three hours of ILZ-sCD95L induction.

#### CD95-GFP-pE (physiological expression)

To achieve a stable cell line with physiological expression fluorescent receptors, the stable clone CD95-kd was used, where endogenous receptor is knock down and that is already resistant to G418. Therefore the vector contained the mutant form of CD95 (minimized

recognition by shRNA) and a resistance to puromycin. Clones were selected according to death test and receptor amount similarly to the example above.

*Laboratory name: Fas-GFP-#7*

## 3.2. Immunostaining

The immunostaining protocol of HeLa cells for confocal microscopy was optimized building on a protocol existing in the lab. The goal was to observe the receptor distribution as is it in living cells without artifacts. Notably one disturbance, the cross linking of receptors by the primary antibody could sometimes be observed in the clone overexpressing CD95-GFP (CD95-GFP-hE). Therefore fixation was optimized on this clone, to avoid crosslinking.

**Buffers:** Fixation buffer: HBSS (Hank's Balanced Salt Solution, 10x, GIBCO Ref: 14065-049,  $\text{CaCl}_2 + \text{MgCl}_2$ ), 0.1M sucrose (ubs / SIGMA), 4% PFA (THERMO scientific, Prod# 28908,16%), 0.1% GA (Glutaraldehyde 25% ). Blocking buffer: HBSS, 0.1M sucrose, 1%BSA (Albumine Bovine Serum, Feststoff, SIGMA)

**Sample preparation for microscopy:** HeLa are plated on those cover slips that are later used for microscopy one day before, precool HeLa 5 min, flush with HBSS, fix 30 min with fixation buffer, wash with washing buffer (HBSS, 0.1M sucrose), block three times 5 min with blocking buffer, incubate 1 h with primary antibody (Apo 1-3,  $c = 10 \mu\text{g/mL}$ ) at  $4^\circ\text{C}$ , wash three times 5 min with blocking buffer, incubate 1 h with secondary antibody (Alexa 488  $\alpha$ -ms, Atto 647N  $\alpha$ -ms) at  $4^\circ\text{C}$ , wash three times 5 min with blocking buffer, wash quickly with Millipore water, mount with mounting medium (confocal: Fluoromount, STED: Mowiol), dry over night.

**Sample preparation for flow cytometry:** To reach a reasonable amount of cells for measurement, 500.000 cells are used for this protocol. Cells are detached by trypsination and washed with 10 mL PBS. Cells are fixed for 30 min with fixation buffer, for the following steps, the protocol above is followed, where washing is intended as incubation with 10 mL buffer and subsequent centrifugation and resuspension of the cells. Calibration beads (QIFIKIT) are washed once and then incubated with secondary antibody and prepared, following the protocol for cells. Instead of mounting, cells are suspended in 50  $\mu\text{L}$  PBS.

## 3.3. Flow Cytometry

To quantify the receptor on the plasma membrane, we performed quantitative flow cytometry using calibration beads. Cells were trypsinated, washed with DMEM, fixed with 4 % PFA and stained with monoclonal Apo1-3 and anti-ms-Alexa488. Cells were not

permeabilized in order only to stain the receptor on the plasma membrane.

For fluorescence measurements a flow cytometry system FC500 / MPL (Beckman Coulter) was used. It has a 488 nm, 20 mW Argon Laser is used for excitation. A setup with various dichroic interchangeable dichroic filters redirects the light to forward scatter, side scatter and fluorescent detectors.

The fluorescence measure in arbitrary units, however it is proportional to the number of fluorescent molecules and assuming an equally distributed staining, it is proportional to the number of receptors on cells. Fluorescence was calibrated using calibration beads with defined number of primary mouse antibodies, that are staining following the same protocol as the cells, Figure

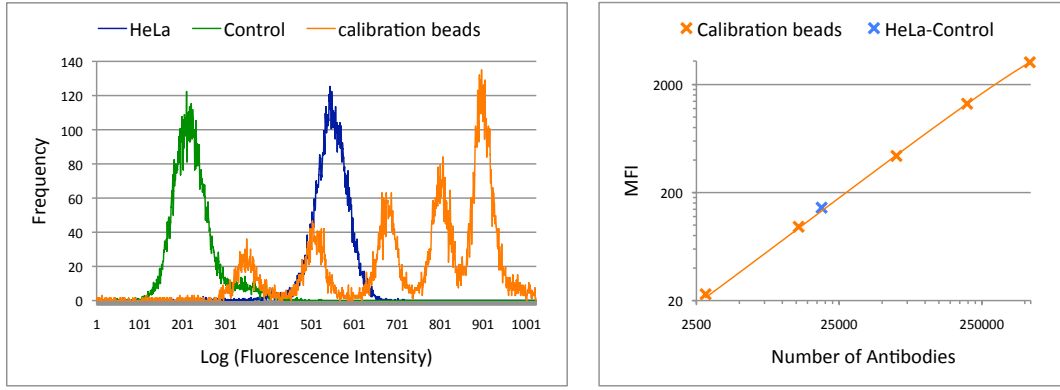


**Figure 3.3.:** Histogram of calibration beads is used to quantify receptor levels on cells: HeLa cells and calibration beads are stained following the same protocol, the known number of mouse antibody on the five populations of the calibration beads allows for a direct comparison of the logarithmic intensities of stained cells and control cells.

The number of antibodies  $N$  for every peak is provided by the manufacturer and mean fluorescence intensities for the beads MFI as well as for the cells  $I_{cells}$  are estimated from the histogram.

$$\log(N) = m \cdot \log(\text{MFI}) + n \quad \Longleftrightarrow \quad N_{\text{rec}} = N_{\text{cell}} - N_{\text{control}}$$

### 3.4. Confocal Laser Scanning Imaging

Images were acquired with a Leica SP5 confocal laser scanning microscope.  
Laser 488 nm

### 3.5. Fluorescence Recovery after Photobleaching

FRAP analysis was performed on a Leica LSM SP5 microscope equipped with an Ar 488 nm laser. A stripe of 2  $\mu\text{m}$  width was bleached on the lower plasma membrane of the cells and relative fluorescence intensities were measured. By measuring the widening of the stripe after bleaching the diffusion coefficient was estimated.

Pixel size was set to 247 nm, which with a stripe width of about 2  $\mu\text{m}$  allows still for a good spatial resolution even if not maximal Niquist sampling. With a scanning speed of 1000 Hz and an image size of 256 pixel, this allows for a time resolution of 0.28 s. This leads to an intensity signal of about 29 (arbitrary units) with a noise standard deviation of 12, which still allows for a good fitting of the gaussian profile.

To allow for an automated measurement of cells after induction the autofocus modus of the microscope was used. Autofocus is typically measured in reflection mode. At very low resolution and very little frame size (64 x 64 pixels) a user-defined z-range is scanned and highest intensity estimated, corresponding to the level of the glass surface, where the laser is reflected. The next image is then taken at a user defined distance from the glass (for the lower membrane typically around 0.3  $\mu\text{m}$ ).

### 3.6. Spinning Disc Confocal Imaging

I want to kindly thank the Nikon Imaging Center der Universität Heidelberg for the possibility to use their devices for Spinning Disc confocal imaging.

The confocal spinning Disc images were acquired on a Perkin Elmer spinning disc confocal ERS-3 on a Nikon Eclipse Ti inverted microscope using the laser line 488 nm. The system is equipped with a highly sensitive Hamamatsu EM-CCD camera C9100-50 (sensitized emission method) with a pixel size of 83.4 nm and a 100x 1.4NA Plan Apo Oil objective.

The following parameters were used for image acquisition: Laser Power: 75%, AOTF: 100%. field of view: 100  $\mu\text{m}^2$ , exposure time: 2 s, EM-Gain camera: 120. To allow for highest possible resolution the z-step size was chosen 0.15  $\mu\text{m}$  and no binning in xy was applied to meet the Nyquist sampling theorem.

### 3.7. Stimulated Emission Depletion Microscopy

The stimulated emission depletion images were acquired on a STED system, built in house by Matthias Reuss in the Department Optical Nanoscopy of the German Cancer Research Center. The system consists of a Leica DMI6000 stand, where external pulsed

lasers were coupled in for excitation and STED. For beam scanning, a home-built "Quad-Scanner" was used as described in [74].

For excitation a pulsed laser diode (Picoquant, Germany) was used at a wave length of 634 nm, triggered by the STED-laser via optical pickup using a fast photodiode (PDM-400, Becker & Hickl, Germany). The STED laser was a Titanium:Sapphire laser (Spectra Physics, Canada, repetition rate 80 MHz used at a wave length of 750 nm. The pulses were stretched to  $\approx 200$  ps by sending them through 50 cm of NBK5 glass followed by a 100 m long single-mode polarization-maintaining fiber (OZ Optics, Canada). The STED intensity was about  $70 \text{ MW/cm}^2$  in the focal plane.

The following parameters were used during image acquisition: pinhole size: 1 Airy disc, dwell time:  $100 \mu\text{s}/\text{pixel}$ , field of view:  $100 \mu\text{m}^2$ , pixel size: 20 nm. The excitation power at the back focal plane was  $10 \mu\text{W}$ , the STED power 100 mW.

### 3.8. Dot Segmentation Image Analysis

Stefan Wörz, in our department developed an image processing tool for the segmentation of point-like structures with intensity profiles similar to two or three-dimensional gaussian functions [98].

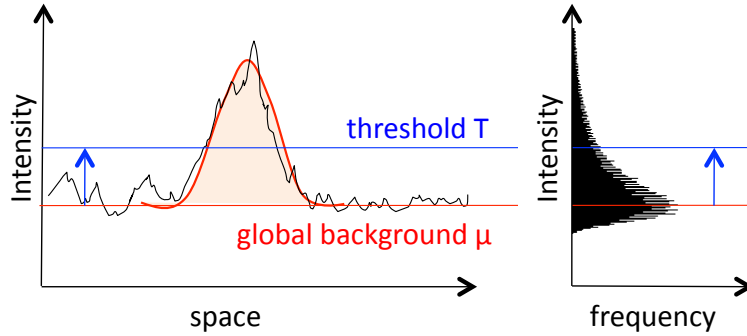


**Figure 3.4.:** Dot Segmentation. The background is determined as the maximum of the intensity histogram of the image. The threshold for spot detection is determined as  $T = \mu_h + f\sigma_h$  where  $\mu_h$  and  $\sigma_h$  denote the mean and standard deviation of the intensity histogram and  $f$  is an adaptable parameter.

The program works in several steps, Figure 3.4. At first images are smoothed with a gaussian filter of width  $(\omega \cdot \text{pixel size})$  to reduce noise. Then a threshold  $T = \mu_h + f\sigma_h$  is defined, where  $\mu_h$  and  $\sigma_h$  denote the mean and standard deviation of the intensity

histogram of the whole image.  $f$  is a free scaling factor, that has to be sensibly adapted to the image. With this threshold local maxima are determined, that are considered as spot candidates. Every spot candidate is then fitted to a gaussian function. For this fit also a radius of the fitting area can be adapted  $r_{\text{ROI}}$ . The fit results in an effective local background subtraction. Various adaptable rules are implemented, that define how to proceed with overlapping spots, ellipsoid spots, spots of relatively large or small intensity, contrast or size. The output of the program is a list of spots and their features such as integrated intensity  $I$ , contrast  $c$  = amplitude of gaussian to local background, x-, y- and z-position, size and many more.

Depending on the experiment and the biological question, that the images originate from the appearance can be very different: e.g. what structures are images, how close and dense they are located, local and global background, pixel size, but also the composition, resolution and brightness of the structures. Therefore various parameters in the tool are freely selectable and need to be adapted to the respective image.

Part III.

Results

## 4. CD95 Concentration



## 4.1. The Number of Receptors per Cell

### 4.1.1. Quantification of CD95 by Flow Cytometry

To characterize the receptor on the plasma membrane my first goal was to estimate number of receptor that are on the plasma membrane to be able to determine receptor concentrations.

To quantify the receptor on the plasma membrane, we performed quantitative flow cytometry using calibration beads. Cells were fixed and stained with monoclonal Apo1-3 and anti-ms-Alexa488. Cells were not permeabilized in order only to stain the receptor on the plasma membrane.

Fluorescence of a whole cells is measured by flow cytometry and yields an intensity value in arbitrary units. These units can be calibrated using calibration beads. These beads are consist of 5 populations with a defined number of mouse epitopes on the surface. They are stained with the same protocol as the cells and since fluorescence is proportional to the number of fluorescent molecules on the surface, they are used to calibrated the intensity scale to numbers of receptors. An example of fluorescence intensity distributions of these beads and of HeLa cells is shown in Figure 4.1, note that the fluorescence intensity is depicted on a logarithmic scale, therefore lognormal intensity distributions appear as gaussian bells. The control consists of cells, stained without the primary antibody and represents the unspecific staining and autofluorescence. To estimate the number of receptors per cell, the median for HeLa and control are subtracted and calibrated again the beads as described in chapter 3.3.

It has been proposed that binding of the primary antibody is hindered by fixation, therefore I tried incubation with the primary antibody (Apo 1-3 and Apo 1-1) before and after fixation, Figure 4.2. There is not a massive difference in fluorescence intensities, when fixing before or after the primary antibody, showing that the antibody can still bind after fixation. Therefore to avoid long detachment times of living cells, in all further experiments cells were fixed before staining.

I tested both antibodies to know whether staining they both work well and especially with fixation before staining, results are very similar, Figure 4.2.

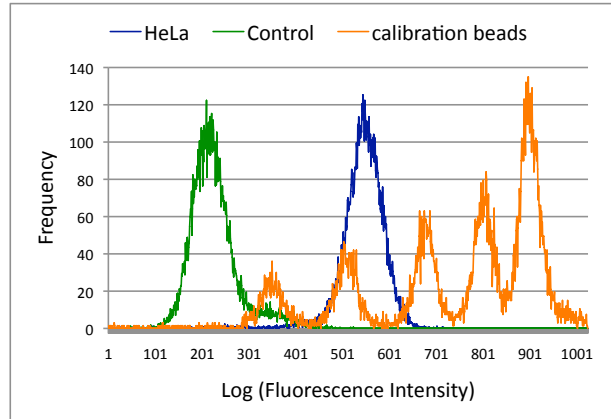


**Figure 4.1.:** Histogram of calibration beads is used to quantify receptor levels on cells: HeLa cells and calibration beads are stained following the same protocol, the known number of mouse antibody on the five populations of the calibration beads allows for a direct comparison of the logarithmic intensities of stained cells and control cells.

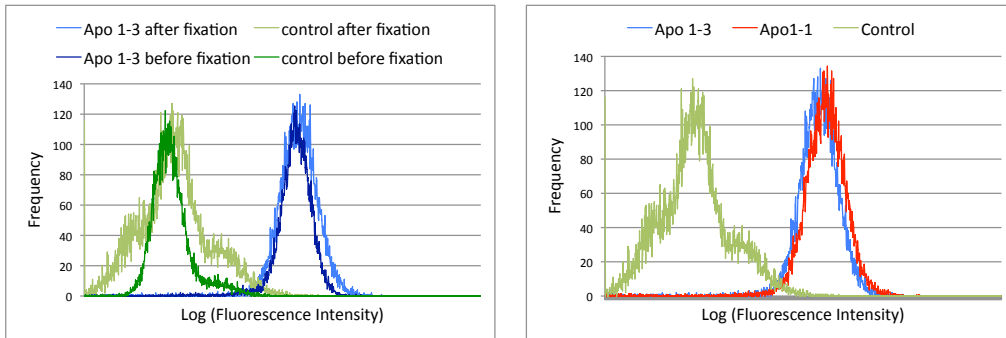


**Figure 4.2.:** Protocol optimization. Left: fixation does not hinder antibody binding, since both peaks show similar intensities. Therefore fixation should be performed before staining, to avoid long detachment times of living cells. Right: both antibodies yield similar fluorescence values, therefore in future either one can be used.

#### 4.1.2. The Typical CD95 Expression is roughly 10000 Receptors per Cell

My goal is to characterize the receptor on the plasma membrane notably determining clustering and oligomerization levels at different receptor concentrations. High expression levels can easily be achieved with transient transfection (also a stably high expressing cell line was produced by Joël Beaudouin in the lab, CD95-hE and CD95-nGFP-hE, chapter 3.1). For low expression levels I produced stable knockdowns as describes in chapter 3.1. For observation in living cells, I produced a clone stably expressing CD95-mGFP at physiological expression levels in the knockdown.

#### 4. CD95 Concentration

---

Using this protocol, I determined expression levels of different cell lines: HeLa cells, clones highly expressing the receptor (CD95-hE) or the receptor fusion (CD95-mGFP-hE), the receptor knockdown clone (CD95-kd) and the clone expressing physiological levels of fluorescent receptor (CD95-pE), Figure (6.1). Error bars represent the estimated measurement error, when averaging over experimental replicates.

	receptor number	error
CD95-hE	200000	-
CD95-mGFP-hE	100000	-
HeLa	21249	1328
CD95-pE	9937	4000
CD95-kd	2705	1675
Panc1	8023	2430
T98G	6397	837
LN18	7040	2000
Jurkat	13000	-

**Table 4.1.:** Mean number of receptors per cell estimated by flow cytometry. High expression is about 10 times higher than physiological expression, while the knockdown reduced receptor amount about 3 fold. Error bars represent the estimated measurement error, averaging over experimental replicates (not cell to cell variation).

The mean number of receptors on HeLa cells is about 20.000. High stable expression yields about 10 fold higher expression. The knockdown clone contains about one third of the receptor amount. I produced a stable line, expressing CD95-GFP at physiological expression levels, making allowing for live cell experiments at physiological expression levels.

Some other cell lines: neuronal, pancreatic and lymphocyte were tested and had similar expression levels as HeLa, indicating, that measurements at physiological expression levels are also relevant for a wider range than HeLa.

## 5. CD95-Clustering at High Expression Levels

## 5.1. CD95 resides into Dots at the Plasma Membrane upon Induction

Our goal is to characterize the receptor localization and distribution on the plasma membrane, especially focussing on receptor clustering on the plasma membrane. To reach this aim, a GFP-fusion of the receptor was expressed at high levels in HeLa cells imaged by confocal laser scanning microscopy.

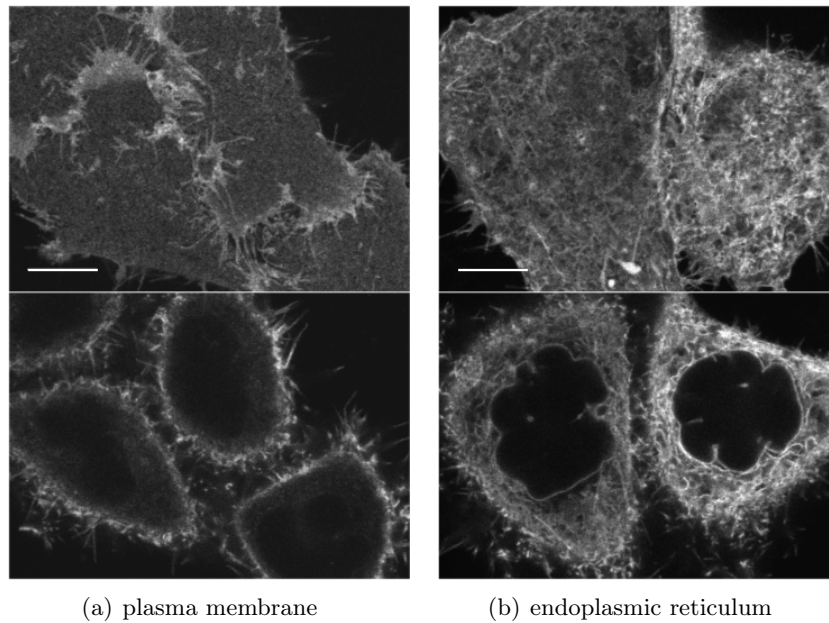


**Figure 5.1.:** HeLa cells, 3 days after transfection with CD95wt-GFP. (a) CD95wt-GFP is homogeneously distributed on the outside the cell if located at the plasma membrane (b) it forms a net-like structure inside the cell, when located in the endoplasmic reticulum. Top: lower part of the cell. Bottom: section of the cell. Scale bar 10  $\mu$ m.

One challenge is to only observe the receptors that are on the cell surface and not those inside internal trafficking pathways. Therefore receptors were imaged three to four days after transfection, which gives enough time for the transport from the endoplasmic reticulum to the plasma membrane. Moreover we studied only the receptors that appeared homogeneously distributed on the plasma membrane and discarded those that localized in a net-like structure of the endoplasmic reticulum in the inside of the cell, Figure 5.1. Another challenge is to achieve even images that allow quantification of the receptor distribution. Therefore we imaged the lower plasma membrane, that lies flat in one layer unlike the filipodia at the top of the cell, Figure 5.1. In order for the membrane to attach

evenly on it, the glass was coated with fibronectin before plating the cells as described in chapter 3.1.

Using this protocol it was possible to observe the behavior of the receptor on the plasma membrane after induction: within one hour after induction with relatively high ILZ-sCD95L concentrations (killing within 30-60 min) the pool of evenly distributed receptors contracts into dots at the plasma membrane (Figure 5.2). The structures are highly dynamic, Figure 5.3.

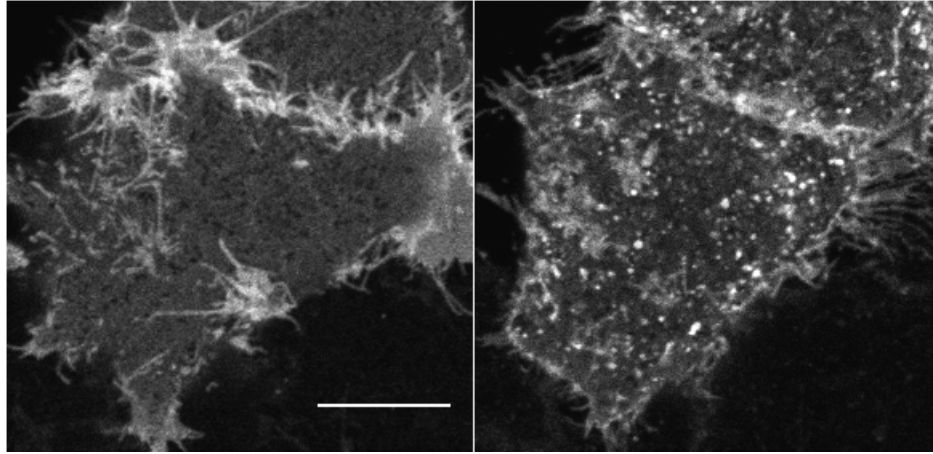


**Figure 5.2.:** Upon induction dots form on the plasma membrane. HeLa cells transfected with CD95wt-GFP. Left: before induction. Right: after one hour induction with ILZ-sCD95L the receptors form dots at the cell surface. Scale bar: 10  $\mu$ m

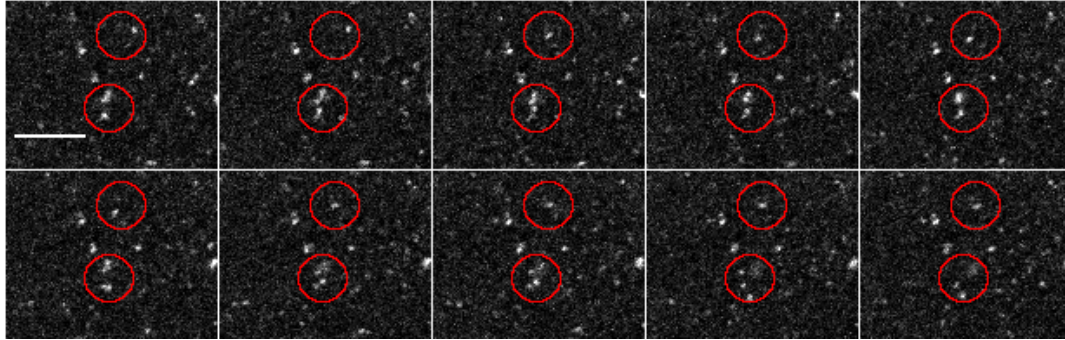
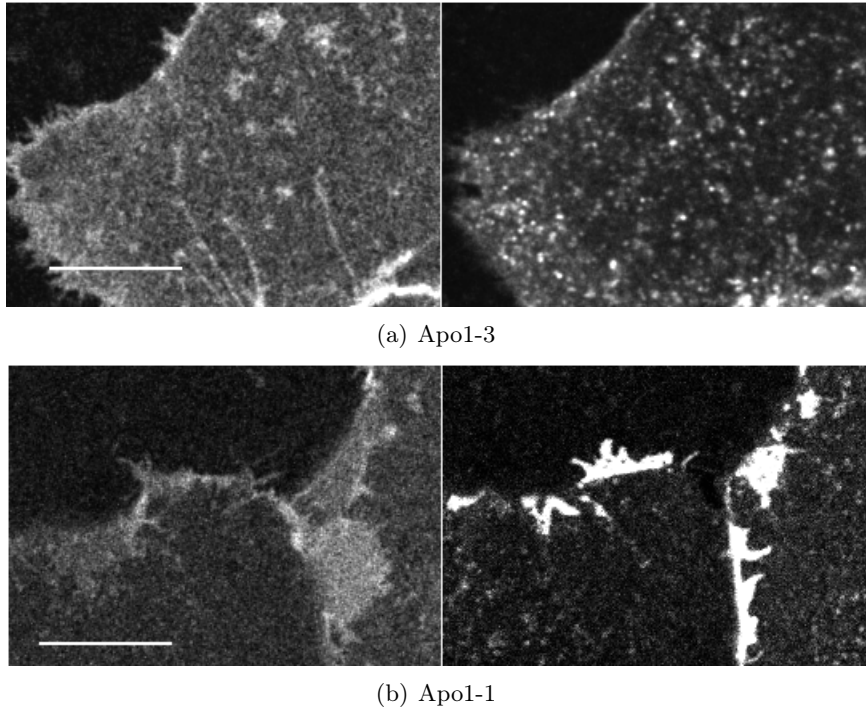


**Figure 5.3.:** The dots that form on the plasma membrane are diffusing visibly. HeLa cells transfected with CD95wt-GFP. In a time lapse microscopy after induction with ILZ-sCD95L at high time resolution (same settings as used for fluorescence recovery after photobleaching). The structures change their position regularly (within the marked ROIs). Images at a frame time of 1.3 ms. Scale bar: 5  $\mu$ m

To test whether the dot formation is correlated with the death-inducing function of the receptor, we used different inducers and studied their ability to form CD95 dots.

The agonistic antibody Apo1-3 induces similar dots as the ILZ-sCD95L, Figure 5.4(a), when used at concentrations of 1  $\mu\text{g}/\text{mL}$ , a concentration that kills cells on the same time-scale as the high concentrations of ILZ-CD95L (data not shown).

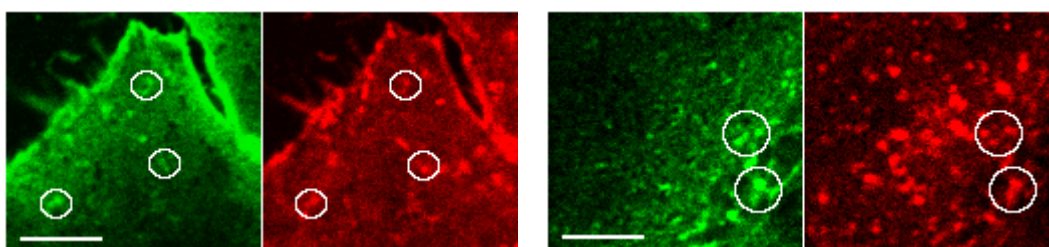
When using the non-agonistic antibody Apo1-1 at the same concentration, we did not observe the same formation and dynamics of the dots, Figure 5.4(b). Rather patch-like patterns appeared mainly at the connections between two cells, which indicates that receptors are not crosslinked on the same membrane, but different membrane patches are crosslinked by the antibody. The Apo1-1 antibody is not able to induce cell death and does not form the typical receptor dots on the plasma membrane, indicating that these dots might correlate with the death-inducing function of the receptor.



**Figure 5.4.:** Different inducers form different receptor patterns: HeLa cells transfected with CD95wt-GFP. Left: before induction. Right: after one hour induction with antibody at the concentration of 1  $\mu\text{g}/\text{mL}$  (a) Apo1-3 form the typical dynamic structures. (b) Apo1-1 forms large patches at cell connections. Scale bar: 10  $\mu\text{m}$ .

There are various possibilities for the origin of these dots. Receptors could be clustering, due to molecular interaction, be it the ligand, the receptor or the downstream proteins.

Another possibility is the relocation of receptors into lipid rafts on the plasma membrane. A third different alternative is the accumulation of internalized receptor into early endosomes. To exclude the latter, one needs to test whether the receptors in the dots are still inserted in the membrane and reach the outside or whether they are already internalized. The resolution of confocal microscopes is in the range of hundreds of nm, hence we can not resolve structures of nm thickness, such as the plasma membrane and DISC formation. Therefore to test whether the receptors in the dots are still on the cell surface, live cells were induced to form dots, then cells were fixed and immunostained without permeabilization, to allow the antibody to stain only targets on the plasma membrane.



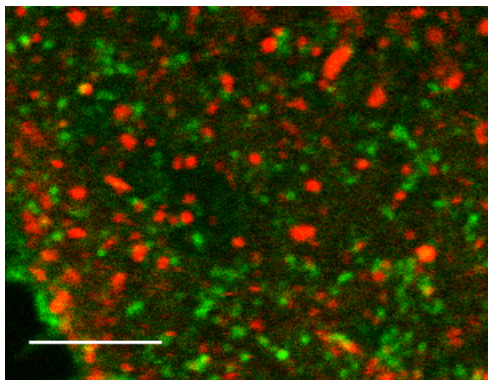
**Figure 5.5.:** Dots can be immunostained and therefore reach the outside of the cells. HeLa cells were transfected with CD95wt-cherry (red) and induced for one hour with ILZ-CD95L. Then cells were fixed and immunostained with Apo1-3 mouse antibody and antimouse-Alexa-488. Scale bar:  $\mu\text{m}$

Figure 5.5 shows that some dots can be stained by the antibody, but also the receptors on the plasma membrane, that are not located in dots are stained, forming a high background, that impedes good statistics and quantitative analysis. This however suggests that parts of the dots are present at the plasma membrane and are not formed in early endosomes.

To confirm this further, I performed staining of the early endosomes with a fluorescent cherry construct of the Rab5 early endosome marker, while simultaneously imaging the formation of the receptor dots as previously. The early endosomes do not colocalize with the formed dots of receptors as can be seen in Figure 5.6.

I found formation of dots upon induction, that appear very similar to aggregated structures that were found mainly in type I cells by Siegel and Muppidi [37] but also in the form of SDS-stable aggregates [38]. Upon antibody induction of Cos-7 cells and SKW 6.4 cells structures, named signaling protein oligomeric transduction structures (SPOTS) were observed by microscopy. In Jurkat cells cap formation could be shown. SDS-stable aggregates were mainly observed in type I cells (SKW 6.4 and H9) and typically were about 90 to 200 kDA.





**Figure 5.6.:** The dots do not colocalize with early endosomes. HeLa CD95 knockdown cells were transfected with CD95-wt-GFP (green) and Rab5-cherry (early endosome marker). Cells were induced for one hour with ILZ-CD95L and imaged as live cells. The dots do not colocalize with the early endosomes excluding internalization as only clustering mechanism. Scale bar: 5  $\mu$ m.

In most of such studies antibodies instead of ligand were used for induction, since antibodies most likely bind to different epitopes than the ligand, also the transduction mechanisms might be different. Therefore in this work mainly ligand induction was used to aim for more physiological conditions.

Most studies also investigated in detail internalization, formation of structures such as SPOTS and SDS-stable aggregates, and induction and signal transduction mechanisms in type I cells. The one study involving HeLa cells mainly treats coculture experiments and membrane bound ligand induction [44].

Therefore this work aims for the study of the type II cell line HeLa upon ligand induction. I compare to structure formation, that has been observed in type I cells. A quantification of dot distribution and size (number of molecules) will be carried out in chapter 5.2 to allow for a comparison with SDS-stable aggregates. To test whether function of structures is similar in HeLa compared to type I cells, dot formation in different clones, related to the functions of lipid rafts and death domain aggregation was observed in chapter 5.4.

## 5.2. Quantification of Dot Formation

based on the Dot Segmentation Tool by Stefan Wörz [98]

To quantify the kinetics of dot formation, I set up an image processing pipeline around the central part for dot recognition: an Dot Segmentation Tool implemented by Stefan Wörz for microscopy images, described in 3.8 and [98].

To allow for correct comparison between different time points preprocessing, Figure 5.7 was adjusted to the specific experimental images and the question. The dot segmentation using the automated Dot Segmentation Tool by Stefan Wörz is performed. For the further processing and evaluation of the segmentation information I implemented a Matlab tool, to determine intensity distribution histograms and compare the different time points.

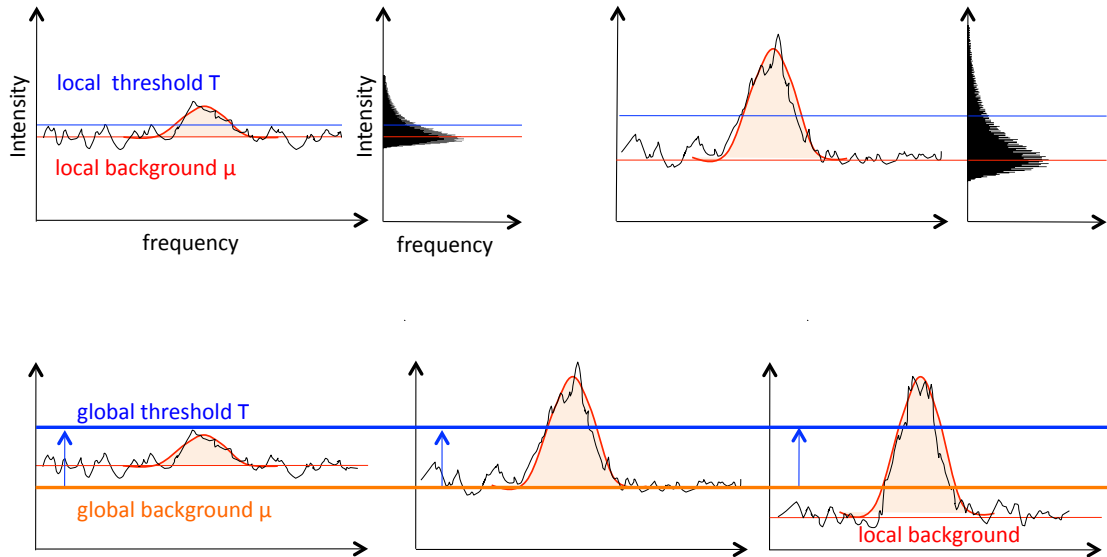


**Figure 5.7.:** Pre-processing of images had to be adapted to the experimental question and the features of the Dot Segmentation Tool by Stefan Wörz. To allow for a comparison of images of different time points, the automatically set threshold has to be set globally (Bottom) and not locally (Top). Therefore in a preprocessing step images are combined into a montage in ImageJ.

To acquire time series data HeLa CD95 knockdown cells (CD95-kd) were transfected with CD95-wt-mGFP as in the previous experiments, chapter 5.1, and induced with ILZ-sCD95L. In order to observe cells for longer times, apoptosis was blocked using the

caspase inhibitor zvad. Time lapse imaging was performed in collaboration with Joël Beaudouin.

### 5.2.1. The Number of Dots increases over Time

To achieve optimal segmentation, images have to be preprocessed accordingly and parameters adjusted. The threshold for spot detection is defined by the image analysis tool indirectly using the mean  $\mu_h$  and standard deviation  $\sigma_h$  of the image histogram, as illustrated in Figure 5.7(a).

For the experiments of this study however the goal is to compare images of the same cell at different time points, therefore the same threshold should be used. To achieve same threshold settings, Figure 5.7(b), all images were combined into a montage in ImageJ before compilation by the analysis tool. The output file, containing the spot feature information had to be re-sliced accordingly.

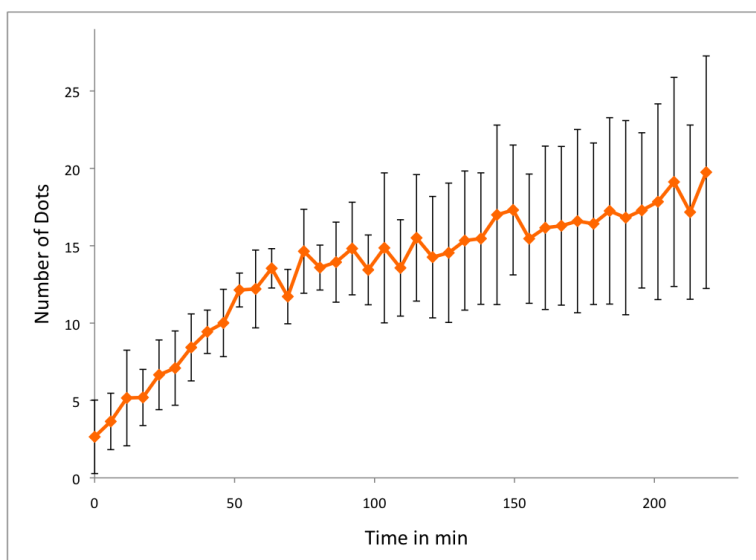


**Figure 5.8.:** The number of dots increases upon ligand induction. HeLa cell were transfected with CD95wt-GFP upon induction with ILZ-sCD95L and zvad, time lapse imaging was performed. Images were segmented using the Segmentation tool by Stefan Wörz and the Matlab tool for further data processing. The number of dots on  $100 \mu\text{m}^2$  of the lower plasma membrane is showed related to time.

The parameters for the smoothing, threshold, fitting size were adjusted by eye, to optimize dot recognition. To avoid segmentation of big dark structures such as membrane unevenness instead of bright dots especially at early time points where the pool of recep-

tors is still bright, the tool was adjusted to exclude structures of size bigger than  $400 \text{ nm}^2$ .

Figure 5.8 shows the number of dots per  $100 \mu\text{m}^2$  appearing on the plasma membrane over time. The dots appear steadily in time for about 90 min until the dot density reaches a plateau at about 14 to 18 dots per  $100 \mu\text{m}^2$ .

### 5.2.2. The Dot Size increases over Time

The next question was whether dots grew in size with time, so the molecules per cluster were quantified. The integrated fluorescence intensity of one dot is directly proportional to the number of fluorescent molecules. On the other hand the contrast of the dots is related to the highest pixel intensity and not the number of molecules. Therefore I implemented a Matlab tool to analyze histograms of the dot intensities  $I$  or contrast  $c$  for every image. Figure 5.9 shows the distribution of values of  $I$  of one example time point of one image. By fitting a lognormal curve to the distribution, the mean fluorescence intensity, the mode of the curve or quantiles - like the median - can be determined for every time point.

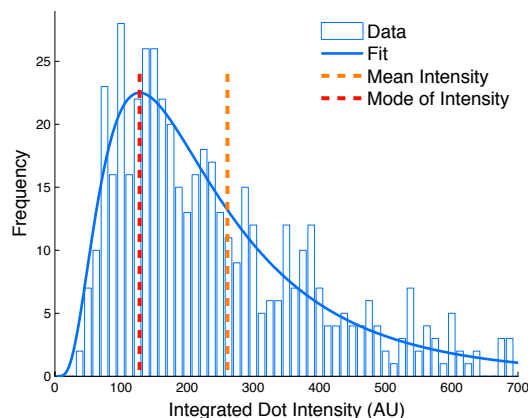


**Figure 5.9.:** Histogram of fluorescence intensity of dots of one image at one time point. I implemented a Matlab tool to determine dot intensity histograms from the dot segmentation data from the analysis using the Dot Segmentation Tool of Stefan Wörz in our department [98]. The histogram can be fit to a lognormal curve and the mean and the mode of the distribution can be estimated from the fit.

The local background of the detected spot is not originating from noise but is fluorescence of the pool of soluble receptor on the plasma membrane. When receptor clusters form, this pool is getting smaller, resulting in a decrease of this background. I tested subtraction of this fluorescent background before spot segmentation, but the influence

on the number of detected spots was negligible. The resulting properties such as dots intensity and contrast were also not significantly altered, which can be explained by the fact, that the gaussian fitting in the image processing tool results in an effective local background subtraction.

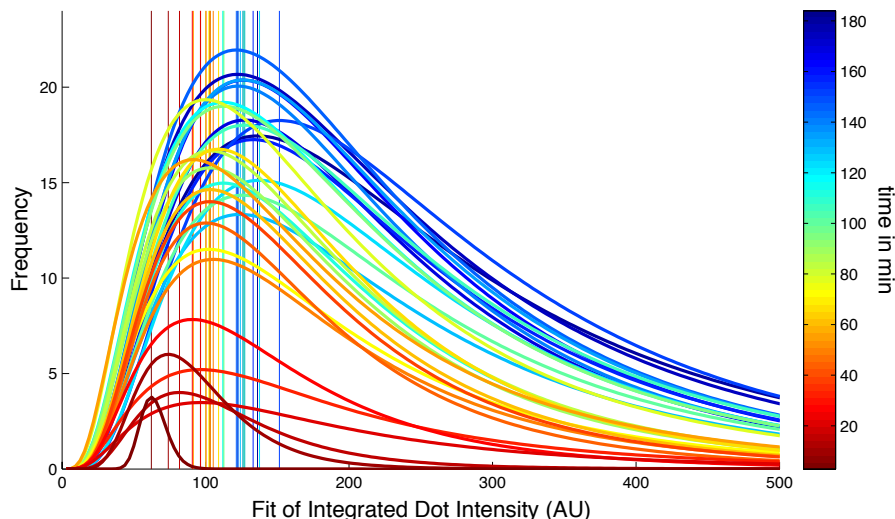


**Figure 5.10.:** Histograms of dot intensity over time. The mode of the histogram, i.e. the intensity value of the peak, increases over time.

Figure 5.10 shows the histograms of the dot intensities at different time points. Again at higher time points there are more dots, represented by the area under the curve. The size of the dots also increases over time as the whole distribution shifts to the right. We conclude that, with time, more receptor molecules get incorporated into these structures.

### 5.2.3. The Majority of Dots contains about seven Molecules

To relate the dot formation after induction to other studies a size estimate would be a good comparison. The SDS-stable aggregates observed in other studies in type II cell have a typical size of 90 to 200 kDa [38], with a receptor of 45 kDa.

In microscopy the fluorescence intensity corresponds to the number of molecules, therefore to estimate oligomerization levels the intensity axis is calibrated.

While the contrast is measured in units, that can not be related to a biological meaning, because it depends on pixel size and settings, the whole integrated dot intensity can

be calibrated by comparison to characterized cells. As calibration the stable cell line Apo-mGFP1 was imaged with the same settings, yielding an intensity of  $759/\mu\text{m}^2$ . The stable cell line has 140 000 receptors on the outside of the cell, relating to the size of the cell membrane  $2000\mu\text{m}^2$ , this results to a receptor density of  $70/\mu\text{m}^2$  and therefore a fluorescent intensity of  $10.8/\text{receptor}$ .

Using an analogous calculation the receptor concentration on the transiently transfected cells of this experiment was estimated; the mean intensity before induction was  $1227/\mu\text{m}^2$  corresponding to a receptor concentration of  $113/\mu\text{m}^2$ . The error of intensity measurement (also due to uneven illumination of different slices) was assumed to be about 8%.

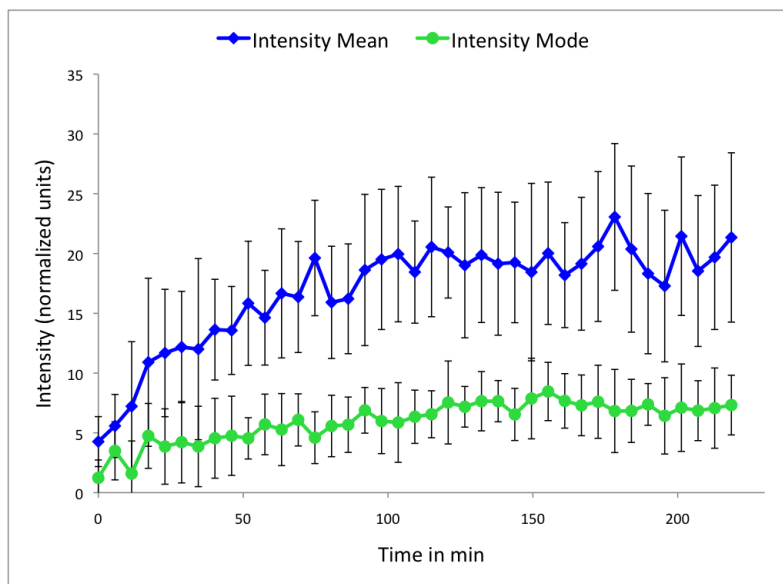


**Figure 5.11.:** The mean and the mode of dot intensity increase over time. The calibration of intensity axis allows for a quantification of the number of molecules per dot. Most dots, i.e. the peak of the distribution, contain 7.2 molecules.

Figure 5.11 shows the mean and the mode of the intensity distributions over time (bars represent the cell to cell variation estimated as standard deviations). Again it shows that the dots grows in size over time.

With the intensity axis calibrated, one can estimate receptor numbers per dot: While most of the dots (intensity mode) contain about  $7.2 \pm 3$  molecules after 150 min, the mean number of receptors in the dots is about  $19.8 \pm 7$ , meaning that a few very big dots shift the mean towards high numbers, while the majority is at 7 molecules per dot.

This calibration of intensity to receptor amount allows for an oligomerization estimate at high expression levels. The number of molecules per dots ( $7.2 \pm 3$ ) is in the same order

of magnitude as the number of receptors observed in SDS-stable aggregates, where 90 to 200 kDa correspond to 2 to 4 receptors.

The precision of measurement of clustering by detecting dots is very depending on image analysis and dot segmentation. Due to the pool of unclustered fluorescent receptors, small clusters can not be identified, as long as their intensities are still within the range of noise and background. Therefore I studied clustering by dynamics measurement, which can possibly allow for detection of smaller clustering, as was shown on dimerization measurements of the EGF receptor. Furthermore it represents a more robust method, not relying on the detection of single dots.

### 5.3. Clustering measured by Dynamics Observation

To study the formation of small clusters, that can not yet be detected as dots and perform more robust methods for higher clustering, that are not sensitive to single dots detection, I performed dynamics measurements of the receptor with fluorescence recovery after photobleaching before and after induction with the ILZ-sCD95L.

#### 5.3.1. Fluorescence Recovery after Photobleaching

In a region of interest (ROI) molecules are bleached and then the unbleached molecules from outside the region move in, while bleached molecules move out. There are different methods to record and analyze these processes. One very common method is to follow the intensity inside the ROI over time.

##### Recovery in the ROI

The most common FRAP- technique is to bleach an area and then follow the fluorescence intensity in that area over time: Part of the molecules can move due to diffusion or other transport mechanisms. This is the so called mobile fraction. But there might be also a fraction of molecules fixed to structures (e.g. by attachment to the cytoskeleton or the extracellular matrix), this is the immobile fraction. After bleaching the mobile fraction can redistribute and its intensity in the ROI can recover, while the immobile fraction does not recover. One example of such an intensity recovery is shown in figure 5.12 (Webpage). Axelrod et. al were first to use this technique in 1976 [99], while Soumpasis introduced a more simple mathematical analysis in 1983 [100].

One can model this recovery assuming three different cases:

In the easiest situation one population of molecules uses diffusion as only transport mechanism: the single component recovery. Computation of an effective diffusion coefficient

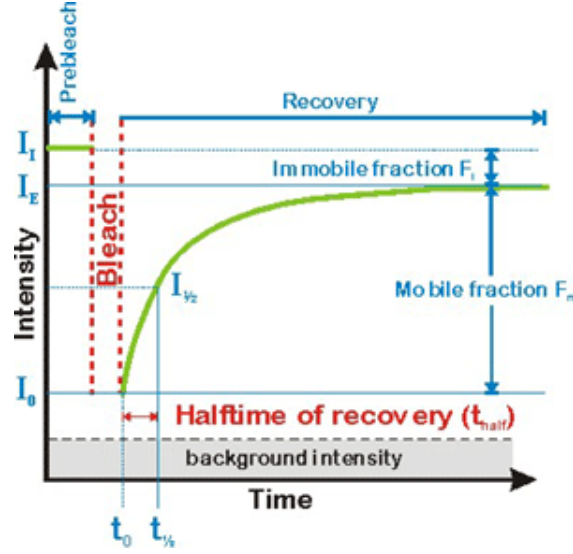


**Figure 5.12.:** Example of a FRAP recovery curve

$D$  from the recovery half time  $t_{1/2}$  for a circular ROI with radius  $\omega$  is relatively straightforward [100]:

$$D = 0.224 \frac{\omega^2}{t_{1/2}} \quad (5.1)$$

In a more complex situation one has to consider multiple components for the diffusion equation, e.g. binding and release from intracellular components or monomeric and multimeric forms. In the third case alternative movement mechanisms might occur such as molecular motors or membrane tension flow.

However this method of diffusion coefficient estimation has its limitations: on the one hand it is highly dependent on a correct estimate of the size of the ROI  $\omega$ , additionally it is assuming that the bleaching takes place in a much shorter time than the recovery, but experimentally bleaching is performed with a scanning laser with finite remaining times. During the bleaching process therefore molecules can diffuse leading to a smearing out of the bleaching profile, a corona effect. Weiss [101] performed simulations of these effects and found that the normal experimental procedure can lead to an underestimation of the diffusion coefficient up to 4-fold.

In this work, diffusion coefficients will be measured on the lower plasma membrane of adherent cells, therefore these problems can be circumvented by the analysis of bleaching profiles in space.



### Recovery of bleaching profile

There have been various theoretical considerations on the influence of the bleached pattern of FRAP analysis [102]. One experimental example using the analysis of the bleaching profile instead of the recovery half time  $t_{1/2}$  was performed in 1986 on a macroscopic scale to measure diffusion (and convection) of tissue fluid where a point wise digitization of the image was used for recording and later fitting of the bleaching profiles [96].

In our experiment on the relatively flat, lower plasma membrane of the cell we used the technique to bleach a stripe and observe the progression of the bleaching profile over time [103] ([96] [102]). The bleached molecules diffuse out of the stripe and fluorescent molecules diffuse into the stripe, making the stripe larger and dimmer. The intensity profile  $I(x)$  can be approached by a Gaussian function in space  $x$  of the width  $\sigma$ :

$$I(x) = \frac{c_0}{\sigma\sqrt{2\pi}} \exp\left(\frac{-x^2}{2\sigma^2}\right) \quad (5.2)$$

As shown in chapter A.1 the width of this Gaussian is proportional to time  $t$ , with the slope related to the diffusion coefficient  $D$ .

$$\sigma^2 = 2Dt \quad (5.3)$$

The advantage of this method is, that it does not depend on the assumption of fast bleaching and the precise estimate of the bleaching profile for time point 0. Instead time point 0 has no meaning and the fitting of the slope yields an accurate estimation of the diffusion coefficient as long as the profiles themselves can be fit well to gaussian curves.

### Experimental procedure

To determine the diffusion coefficient of the transmembrane protein CD95-GFP, we chose cells with a flat lower plasma membrane and bleached a stripe of about  $2\text{ }\mu\text{m}$ . Gradually the bleached molecules diffuse out of the stripe and fluorescent molecules diffuse into the stripe, making the stripe larger and dimmer. For expected diffusion coefficients in the range of  $0.1\text{ }\mu\text{m}^2$ , it means 100 s to cross half the stripe.

As illustrated before, the settings for the bleaching should aim for fast bleaching at high laser power. For the imaging, setting needs to be optimized for the competing quantities. There is a tradeoff between time resolution for an optimal fitting of the equation 5.3, space resolution for the profiles and minimal laser power to avoid corruption by bleaching while imaging.

Therefore pixel size was not chosen to highest spatial resolution, but set to 247 nm. At

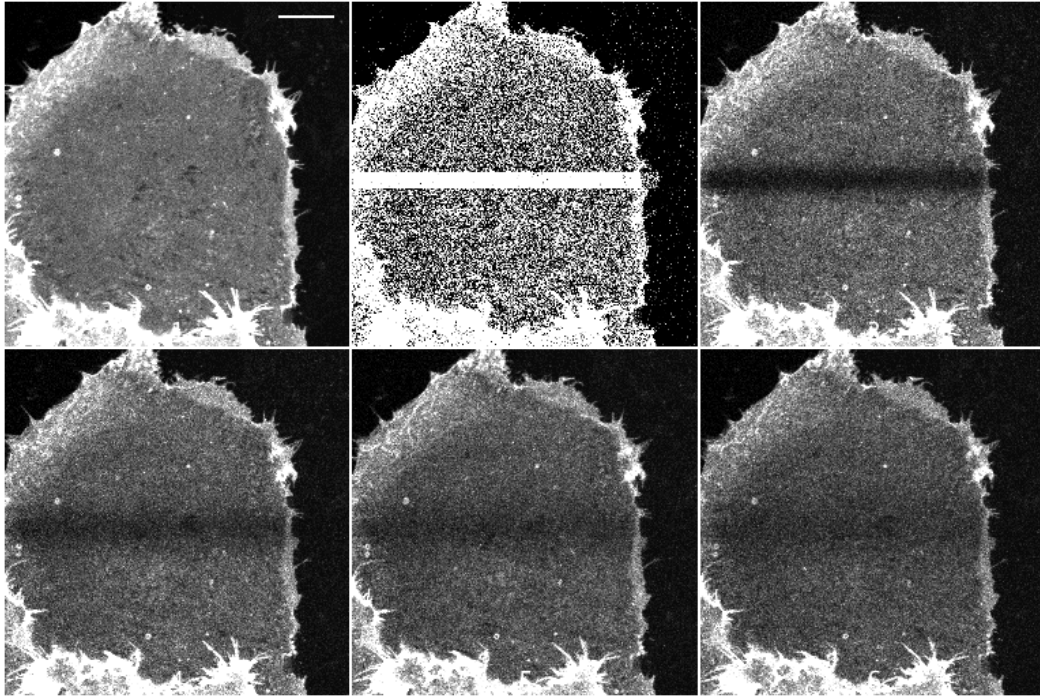


**Figure 5.13.:** Example of a recovery of a bleached stripe on the lower plasma membrane. HeLa CD95-knockdown cells were transiently transfected with CD95-wt-mGFP. After three to four days the lower plasma membrane was imaged, following the FRAP bleaching protocol. Upper left: lower plasma membrane before bleaching. Upper middle: bleaching of a stripe. Upper right: bleaching profile directly after bleaching. Bottom: recovery and widening of bleaching profile with time. Scale bar 5  $\mu\text{m}$

optimal PMT and Laser-settings, this leads to one image every 0.28 s, while still having a signal to noise ratio of 29/12 (Intensity in arbitrary units), that allows for a good fitting 2  $\mu\text{m}$ -profile. We tested bleaching at high laser power and with these settings 20 scans lead to a high bleaching while still being relatively fast.

One FRAP-measurement is performed as following: with the settings from above 20 images are acquired directly before bleaching. Then a ROI is bleached with 20 scans at highest laser power and following directly 100 images were acquired to follow the recovery of the bleached area. Examples of a cell before bleaching (1), during bleaching (2) and recovery between 0 s (3) and 10 s (6) after bleaching are displayed in 5.13. At the early time points (3) the bleaching stripe is dark and narrow, at late time points (6) the bleaching recovered to a nearly even distribution.

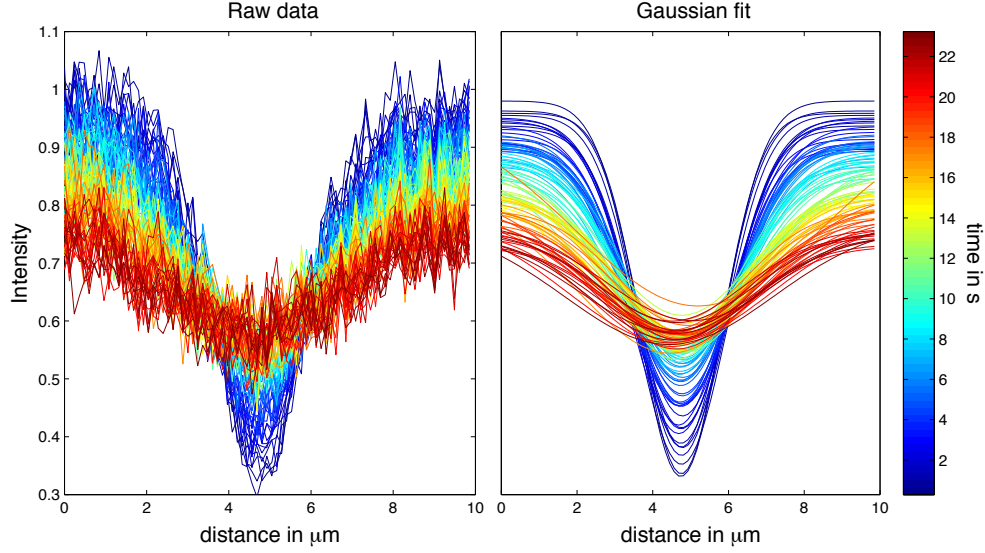


**Figure 5.14.:** The diffusion coefficient  $D$  is estimated by observing bleaching profile recovery. The profile is fit to a gaussian of width  $\sigma$  for every time point, based on a Matlab Tool by Clarissa Liesche in our department. According to equation 5.3 the width of the profile is proportional to the time and  $D$ . The latter is estimated by a linear fit as shown in Figure 5.15.

The mean profile of the stripe for every time point  $t$  is calculated from the images in ImageJ (automated with a plugin from Joël Beaudouin) after background subtraction and normalization with the intensity before bleaching.

These profiles are fit to a gaussian of width  $\sigma$ . Clarissa Liesche provided a Matlab-tool for automated fitting of these curves to the gaussian function, equation 5.2. Figure 5.14 shows the bleaching profiles (raw data on the left) and the respective fits (right) of one example cell for one FRAP measurement (= 100 profiles).

When plotting the width  $\sigma$  against the time, one can fit the linear relationship, Figure 5.15 and estimate the diffusion coefficient according to equation 5.3. Since the profile is becoming more and more shallow, the error of the fit also increases with time, therefore by means of the error it has to be decided until which time point profile data are used for the later linear fit. To guarantee comparability of different data sets, we decided to fit until 30 time points corresponding to 8.4 s.

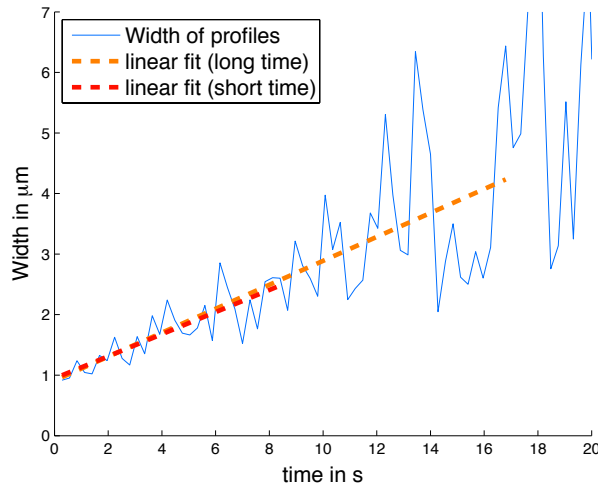


**Figure 5.15.:** The diffusion coefficient is estimated from linear fit of the width of the bleaching profiles estimated in Figure 5.14 to time, according to equation 5.3.

### 5.3.2. CD95 diffuses three to four-fold slower upon Induction

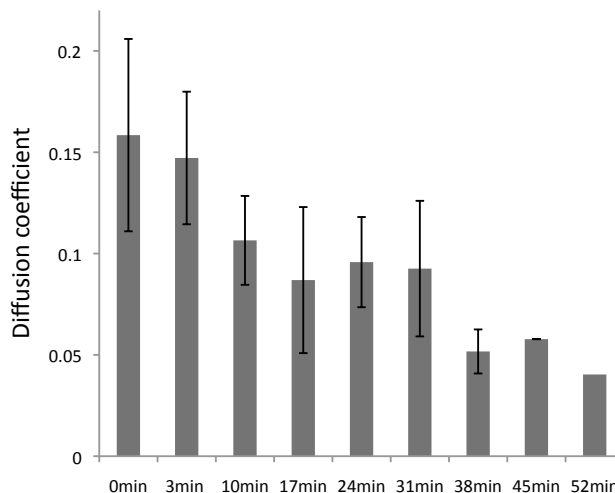
To test whether the receptor oligomerizes after induction, we measured a time series of FRAP after induction. In an automated measurement the same cells were imaged with the above described FRAP-protocol at different time points after induction with ILZ-sCD95L. Again, in order to image receptor on the membrane and not in internal trafficking pathways, cells were imaged three to four days after transfection and plated on fibronectin-coated glass. (data acquisition: Verena Rickert, internship in our department)

Figure 5.16 shows the results of the diffusion coefficient measurement. There is a clear slowdown of the receptor with time, leading to a 3 to 4-fold lower diffusion coefficient after 40 min for CD95wt. The diffusion coefficient before induction is  $0.158 \mu\text{m}^2/\text{s}$ , corresponding very well to literature data for other transmembrane proteins at  $37^\circ\text{C}$  ([94]) - ranging between  $0.03 \mu\text{m}^2/\text{s}$  and  $0.3 \mu\text{m}^2/\text{s}$  depending on cell type and protein.

### 5.3.3. Possible Slowdown Reasons

It is not straight forward to interpret this drop in diffusion coefficient for CD95wt-GFP, since there are various reasons that can lead to a real or apparent decrease, as also discussed in 2.3.1 and 5.3.1:

One possibility is that diffusion is slowed down by a clustering of the diffusing molecules.



**Figure 5.16.:** Fluorescence recovery after photobleaching shows a slowdown of the receptor after induction with ILZ-sCD95L. HeLa CD95 knockdown cells were transiently transfected with CD95wt-mGFP. Three to four days after transfection cells were induced with ILZ-sCD95L and the diffusion coefficient was measured using stripe bleaching fluorescence recovery. Measurements were automatized as a time series to increase precision thus allowing for a comparison between time points. The error bar represent the cell to cell variation. (data acquisition: Verena Rickert, internship in our department)

The increase in membrane spanning radius would slow down the proteins. As discussed before a quantitative description depends on the exact protein and protein interaction structure, that we can only estimate for CD95, therefore clustering can only be observed qualitatively and not quantitatively by FRAP.

A second possibility to account for an apparent slowdown is the directed movement of CD95 either into one direction on the plasma membrane or out of the membrane by endocytosis. The latter was excluded in chapter 5.1, which indicates that dots are not mainly endosomes. Figure 5.17 shows that the mean of the gaussian profile does not move in space, excluding a directed flow of receptors.

A third possibility to slowdown transmembrane receptors is the transient interaction with or binding to other cellular components, again including many possibilities: the redistribution into lipid raft and attachment to the cytoskeleton are examined in ???. Also binding of molecules of the DISC intuitively is a possible explanation for a slowdown of the receptor. However it has been shown, that due to the high viscosity of the plasma membrane, the transmembrane domain is the main diffusion determining part of a transmembrane protein [84], while protein domains and binding particles in the aqueous phase do not slowdown significantly (e.g. domain deletion on the EGF-receptor [104] or binding

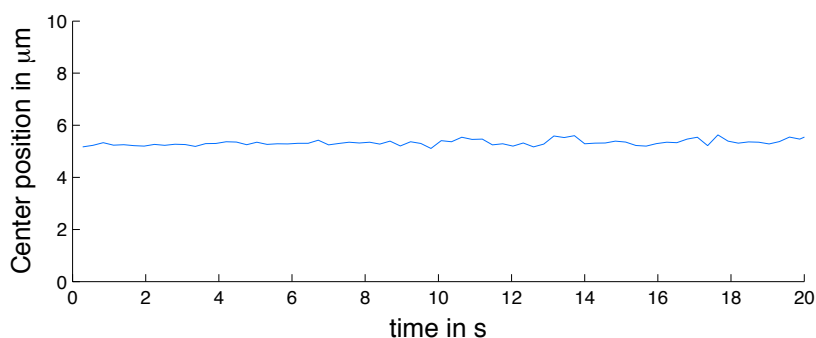


**Figure 5.17.:** The estimation of diffusion coefficient by FRAP can be faulted by a directed flow of the measured molecules. In the experiment of Figure 5.16 the center of the bleaching profile, estimated by the gaussian fit, did not move in space excluding the possibility of a directed flow.

of quantum dots [105] does not change the diffusion coefficient).

A fourth possibility, that could account for the lower diffusion coefficient is, that conformational changes through induction increase friction and thus slow down the molecule. With little information on the structure of CD95 as there is, it is difficult to exclude this possibility, however a slowdown of 3 to 4-fold as observed in the experiments is rather unlikely to be originated only in a small conformational change.

Fluorescence recovery after photobleaching of the receptor showed a three to four-fold slowdown of the receptor about one hour after ILZ-sCD95L induction. The upper reasonings propose clustering of the receptor as most likely reason for the measured slowdown. This clustering measurement is consistent with the clustering observed via dots formation analysis in chapter 5.1. FRAP receptor slowdown measurements confirm the observed clustering and show similar time scales of cluster formation and of cluster saturation.

Both methods, the dots formation analysis and the dynamics measurements were used to investigate the origin of clustering and possible clustering mechanisms.

## 5.4. The Only Aggregation Mechanism is Crosslinking by the Ligand

In chapter 1.3 the different signaling regulation mechanisms were described, that can lead to receptors clustering at different levels. To test whether dot-formation is related to these mechanisms, different mutants were analyzed in terms of dot formation. The focus was put especially on death domain clustering and lipid rafts.

#### 5.4.1. The Receptor Aggregation is independent of the Lipid Rafts

Feig et al. studied in detail the SDS-stable aggregates containing CD95 receptor, that form as early signaling events in type I cells followed by actin-dependent internalization. In SKW 6.4 and H9 cells they could show, that formation of these aggregates in a palmitoylation- dependent process and the formation is abrogated when palmitoylation is blocked by mutation of cysteine 199, reducing internalization and caspase 8 activation. The same palmytoylation site has been reported to responsible for the localization of CD95 to actin cytoskeleton-linked rafts upon stimulation in Hek293T cells [42]. (Both publications show the necessity of palmitoylation of cysteine 199 for CD95 internalization and efficient signaling.)

The dots observed in HeLa type I cells in Figure 5.5 have similar size as the SDS-stable aggregates, for a further comparison the functioning upon palmitoylation inhibition was tested. To test whether formation of the dots is palmitoylation dependent, the CD95-C199V mutant was imaged at the same conditions as experiments above upon ILZ-sCD95L induction. The palmitoylation mutant formed similar dots as the wt-receptor, Figure 5.18. In the majority of clusters (mode of intensity) there are  $9.2 \pm 3$  molecules (where 3 indicated the cell to cell variation), which is the similar dot size as for the wt receptor. Quantification does not show significant difference between dots formation of the palmitoylation mutant and dots formation of the wt receptor.

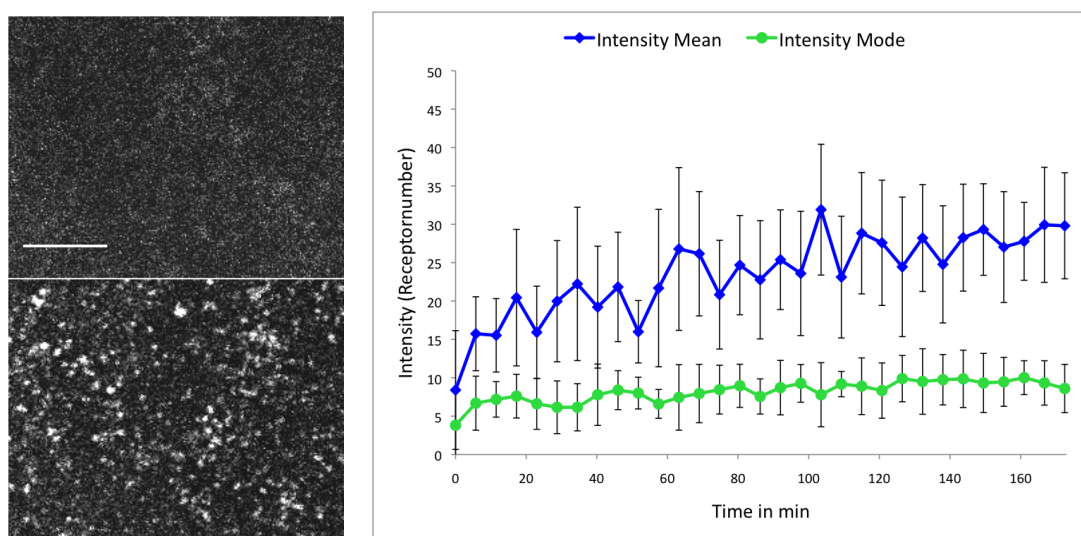


**Figure 5.18.:** Dot formation is not palmitoylation dependent. HeLa CD95-knockdown cells were transiently transfected with CD95-C199V-mGFP, imaged and analyzed as before. Scale bar: 5  $\mu$ m

This shows that contrary to the studies in type II cells, the formation of dots that can be observed by microscopy is not palmitoylation dependent. (As observed in other experiments (data not shown), cells transfected still very efficiently went to 100% apoptosis, the endogenous receptor in the knockdown cell lines contributes only to 10% cell death as shown in chapter 3.1).

To confirm that palmitoylation is not the reason for clustering using a more robust method, dynamics measurements of the CD95-C199V mutant were performed in the same conditions as for the wild type receptor.

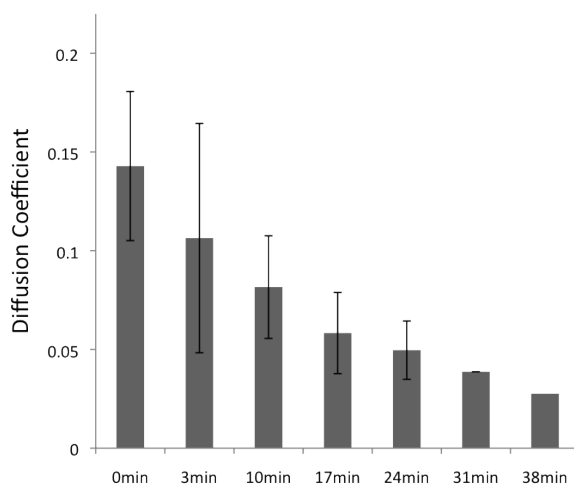


**Figure 5.19.:** Receptor slowdown is not palmitoylation dependent. HeLa CD95-knockdown cells were transiently transfected with CD95-C199V-mGFP. FRAP diffusion coefficient measurements were performed before and after induction with ILZ-sCD95L in an automated time lapse experiment. Error bar represents the cell to cell variation. (data acquisition: Verena Rickert, internship in our department)

Before induction (time point 0 in 5.19 ) the construct diffuses at the same speed as the wild type receptor, (data acquisition: Verena Rickert, internship in our department), showing that mutation itself does not influence receptor diffusion. Upon induction with ILZ-sCD95L the construct shows the same 3 to 4-fold slowdown as the wild type receptor. Therefore lipid rafts can be excluded as reason both for slowdown and for clustering.

The observed clustering in both the dot formation and dynamics experiments is not due to palmitoylation of cysteine 199. Therefore the observed aggregates do not correspond exactly to the SDS-stable aggregates found in type I cells, since they are still able to form, when palmitoylation is inhibited. The cysteine 199 has been shown to be the targeting



signal for the lipid rafts and in Hek293T cells is the connection to the ezrin-mediated cytoskeleton association, which is necessary for the subsequent internalization. Figures 5.18 and 5.19 however show that in HeLa dot formation and clustering is independent of this raft targeting and the ezrin-mediated cytoskeleton association.

#### 5.4.2. The Receptor Aggregation is independent of the Death Domains

The observed dots in HeLa cells of type II do not directly correspond to the SDS-stable aggregates observed in type II cells and do not form in the same palmitoylation dependent manner. There has been another observation of CD95 aggregates: the so-called SPOTS (signaling protein oligomerization transduction structure) can be observed directly by microscopy as spots on the cells after induction. Both the CD95 death domain and FADD are independent for the formation of these aggregates in Jurkat cells as well as CD95-mediated cell death [37]. The central role of death domains for clustering are also supported by structural studies as was discussed in chapter 1.3.

To test whether the observed dots in HeLa form via death domain clustering of the receptor, we imaged the construct, where the death domain was deleted, CD95- $\Delta(210-233)$ -mGFP, as before with time-lapse microscopy after ligand induction.

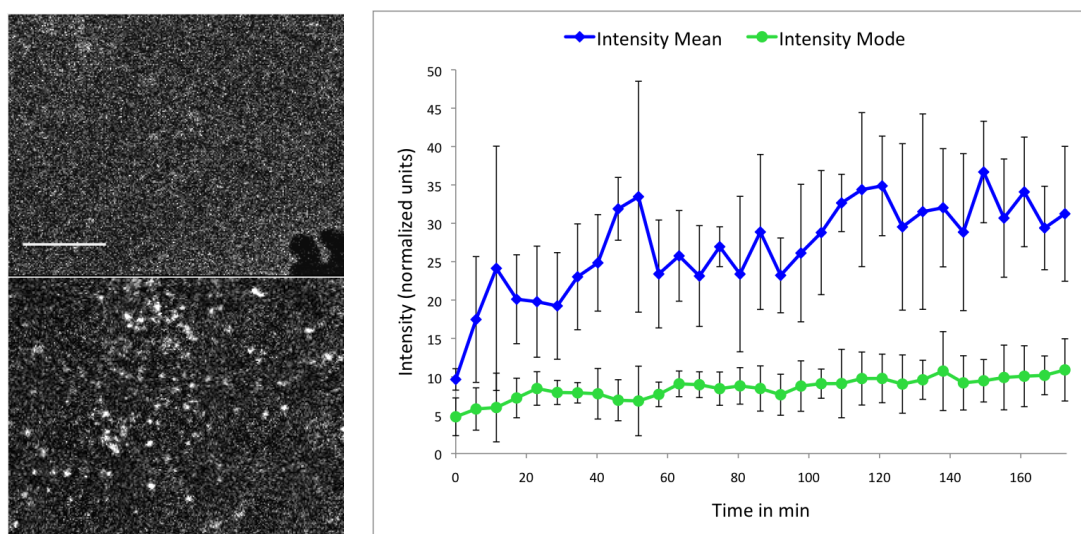


**Figure 5.20.:** Dot formation is not caused by the CD95 death domain. HeLa CD95-knockdown cells were transiently transfected with CD95- $\Delta(210-233)$ -mGFP, imaged and analyzed as before. Scale bar: 5  $\mu$ m.

The death domain deletion did not disturb dot formation. Dots form at the same time

scale and size was even slightly higher (this will be discussed further in the next chapter):  $9.7 \pm 4$  molecules per cluster (mode of intensity), Figure 5.20. (The deletion of the death domain as expected inhibited CD95-mediated cell death (data not shown)).

To confirm this finding, that clustering is death domain independent, FRAP dynamics measurement of the mutant lacking the death domain, CD95- $\Delta$ (210-233)-mGFP, were performed.

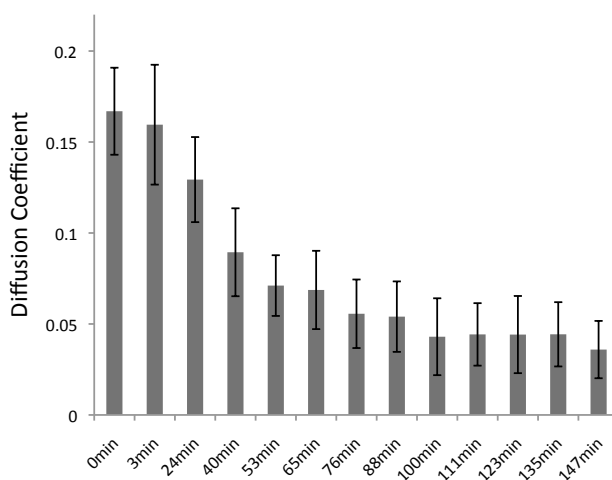


**Figure 5.21.:** Receptor slowdown is not death domain dependent. Fluorescent recovery after photobleaching measurements on a mutant lacking the death domain, CD95- $\Delta$ (210-233)-mGFP, confirm that the receptor clustering at high expression levels is death domain independent. HeLa CD95 knockdown cells were transfected with CD95- $\Delta$ (210-233)-mGFP and the diffusion coefficient measured in an automated manner as a function of time as described before, Figure 5.16. (data acquisition: Joël Beaudouin in the department)

The mutant showed same decrease in diffusion coefficient up to three to four-fold after induction with ILZ-sCD95L. The experiment was performed with a 10 times dilution of the ILZ-sCD95L, which explains the longer time scale of dot formation. To confirm, that dot formation is on the same scale, experiments should be repeated with same ligand concentrations as used in the wild type.

The dynamics and dotsformation experiments show, that the observed aggregation of CD95 receptor in HeLa is not due to a clustering via the death domain. The mutant lacking the death domain is slowed down after ligand induction to the same extent as the wild time receptor and dots formation takes place at a similar time scale and extent

as for the wild type receptor. Contrary to SPOTS formation in Jurkat cells, the death domain is not required for the clustering of the receptor in HeLa cells observed by dot formation analysis and dynamics measurements.

### 5.4.3. The Dot Size is Concentration Dependent

The fact, that cluster sizes vary slightly raised the speculation, that cluster size depends on expression levels. Since cells were transiently transfected, expression levels vary from cell to cell, making it possible to measure cluster size as a function of initial concentration. To test the concentration dependence, cluster size at 150 min was plotted against receptor concentration before induction, calibrated as shown before in chapter 5.2.3. Because of its intrinsic inhibition of apoptosis the death domain deleted mutant can be expressed at higher expression levels than the functional constructs.

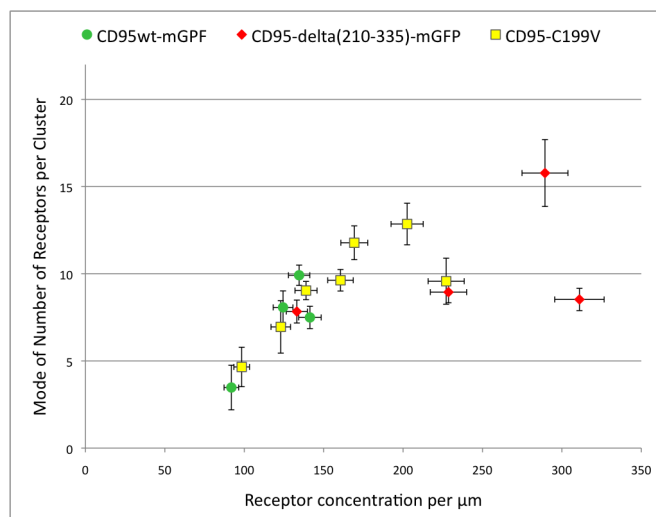


**Figure 5.22.:** The dot size depends on the initial receptor concentration.

The cluster size increases with initial concentration but seems to reach a plateau at a concentration of 200 receptors per  $\mu\text{m}^2$ . The aggregate formation in HeLa cells is concentration dependent. This is complemented by measurement of surface expression levels in CD95 knockdown clones, in which the receptor concentration is proportional to percentage of cell death, chapter 3.1.

In the experiments of this chapter, I observed formation of dynamic clusters of the CD95 receptor after ILZ-sCD95L induction in type I HeLa cells. The clusters were quantitatively analyzed by image analysis and cluster size was estimated to  $7 \pm 3$  molecules per

dot (for the majority of dots, i.e. the intensity mode). Dynamics measurements showed a slowdown of the receptor after induction, that confirmed the cluster formation observed by dot formation analysis.

The mechanism of clustering and dot formation can be neither related to lipid raft localization via the palmitoylation of cysteine 199, not can it be contributed to the CD95 death domain clustering. This indicates that the observed clusters are another kind of structure than the reported SDS-stable aggregates or the so-called SPOTS observed by microscopy in type I cells.

The mechanisms lipid raft localization and death domain clustering were exclude, which also excludes further downstream events such as FADD recruitment as clustering reason. Therefore the ligand induction itself appears as a very strong mechanism, that at high receptor concentrations already alone induces a formation of large aggregates.

Since dot size of receptor clusters as well as the death inducing effect of the receptor is concentration dependent, cluster formation at physiological expression levels in HeLa cells could give more insight on the possible function or necessity of cluster formation for apoptosis induction.

## 6. CD95-Clustering at Physiological Expression Levels

## 6.1. The CD95 Organization on the Plasma Membrane at Confocal Resolution

To observe the CD95-receptor distribution on the plasma membrane, we stained the cells by immunofluorescence and imaged 3D-stacks with Confocal Laser Scanning Microscopy (CLSM). At the highest resolution of CLS-microscopy the receptor distribution appears as a dotted pattern, Figure 6.1. To observe only receptors located on the plasma membrane and not those in the cytosol, the cells were not permeabilized. The cross-sections in the figure show clearly, that no staining is inside the cell.

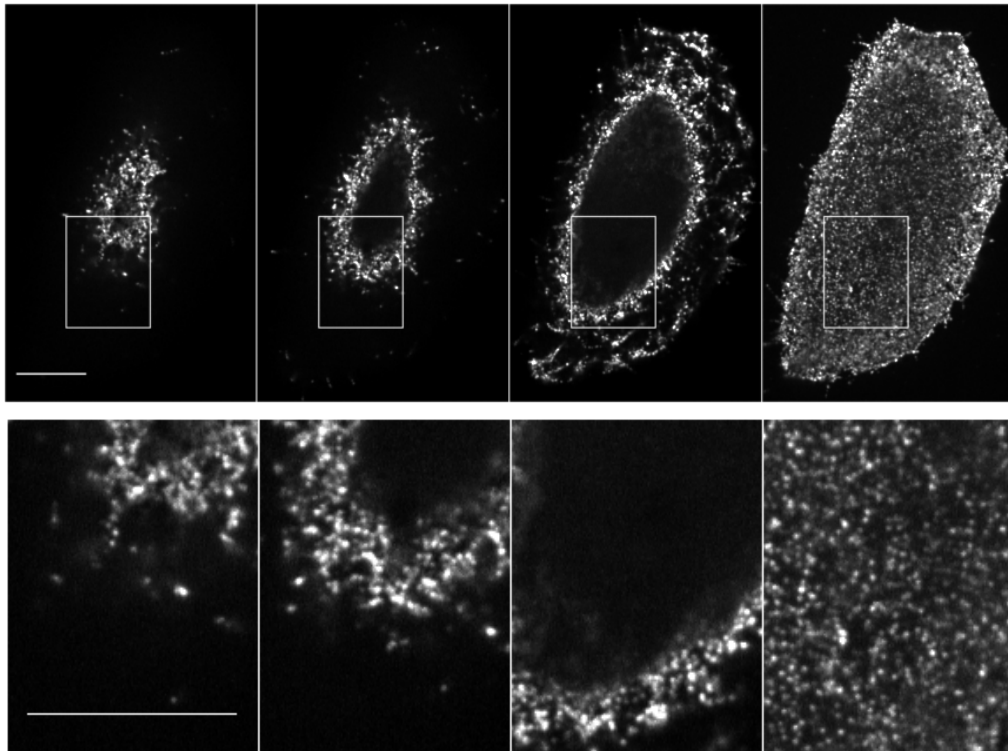


**Figure 6.1.:** 3D-Image of the whole cell. The figure shows only four out of about 60 cross sections of the cell. Top: the whole cell at low magnification. Bottom: the ROI marked in top at 3-fold higher magnification. Scale bar 10  $\mu\text{m}$ .

To prove that this pattern is not an artifact of the fixation and immunostaining, we imaged a stable clone, that expresses the fusion protein CD95-GFP at physiological expression levels in living cells. At these relatively low concentrations these fluorescent molecules are too dim to be well distinguished from the autofluorescence background,

so that they can not be resolved with normal confocal microscopy. To avoid the cytosolic background I performed total internal reflection fluorescence (TIRF) microscopy (in collaboration with Michael Schwering). In this technique, the evanescent field only illuminated a 100 nm-thick layer near the glass, that includes the plasma membrane, while the cytosol is not illuminated and therefore does not generate background. In order to image live cells relatively high laser powers and short illumination times were used.

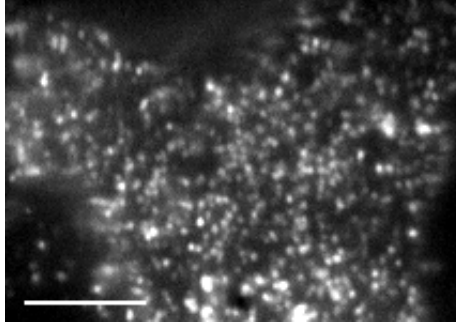


**Figure 6.2.:** Life cell imaging of receptor distribution shows the same dotted pattern: HeLa stably expressing CD95-GFP at physiological concentrations were imaged with total internal reflection microscopy (collaboration Michael Schwering) to reduce autofluorescence background. Scale bar 5  $\mu$ m.

The receptor distribution at the lower plasma membrane of the CD95-GFP clone, shows the same dotted pattern, Figure 6.2, as the immunostained 3D-stacks of HeLa cells. Therefore I conclude, that the optimized fixation and staining protocol enables the imaging of the receptor distribution on the plasma membrane, as it appears in living cells.

For physiological expression levels the receptor distribution can be resolved and shows single dots. But what are these dots? Are these single monomeric receptors or clusters of receptors?

### 6.1.1. Quantification of Dots

#### based on Dot Segmentation Tool by Stefan Wörz [98]

In order to relate to the amount of clustering or oligomerization, I quantified the dots on the plasma membrane of stacks of whole cells and related to the amount of receptors on single cells as determined in chapter 4.1.2.

The Dot Segmentation Tool by Stefan Wörz described in chapter 3.8 and in [98] was used to segment the dots in this dotted pattern and determine number of dots per cell. Figure 6.3 shows a segmentation example, where segmented dots are marked with a black point.

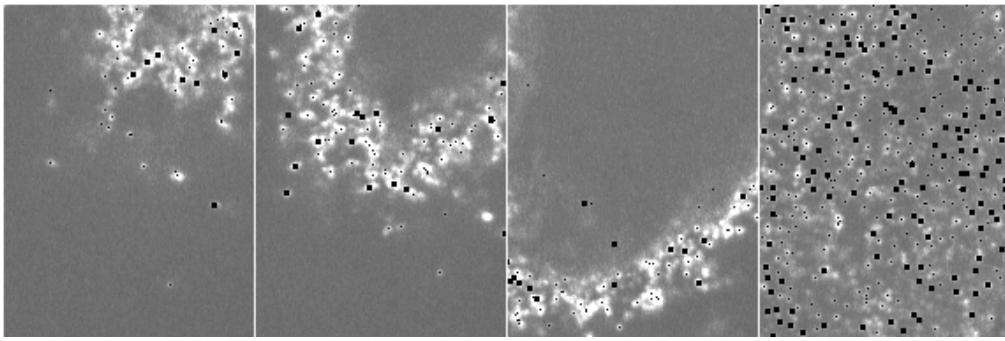


**Figure 6.3.:** Example for dot segmentation with Dot Segmentation Tool by Stefan Wörz [98]. The segmented dots are marked with a black points, the big black points mark dots centered in the image plain, the small black points mark the dots centered in another plain of the 3D image. Scale bar 10  $\mu\text{m}$ .

The number of dots in tryout analysis displayed itself very sensitive to the various tunable parameters and could vary largely even when the visual impression was the same. This is due noise, that is wrongly segmented as dots. To understand this high variance due to noise, I analyzed the number of dots  $N_{dots}(\omega, f)$  as a function of those parameters, that it appeared most sensitive to: the smoothing factor  $\omega$  and the threshold factor  $f$ , Figure 6.4.

When the smoothing kernel is chosen small ( $=$  small  $\omega$ ), the noise is not filtered out correctly and segmented as dots. When  $\omega$  is chosen too big, also the signal of smaller dots will be smoothed, so that these dots are not segmented. Typical values for smoothing would be around the resolution of the microscope (here corresponds to  $\omega = 1$ ), taking account for the fact, that any peak of width smaller than the resolution can only be noise.

Similar considerations hold true for the threshold factor  $f$ : if chosen too high, not all dots are segmented, when chosen too low, noise will be considered as signal. Since the



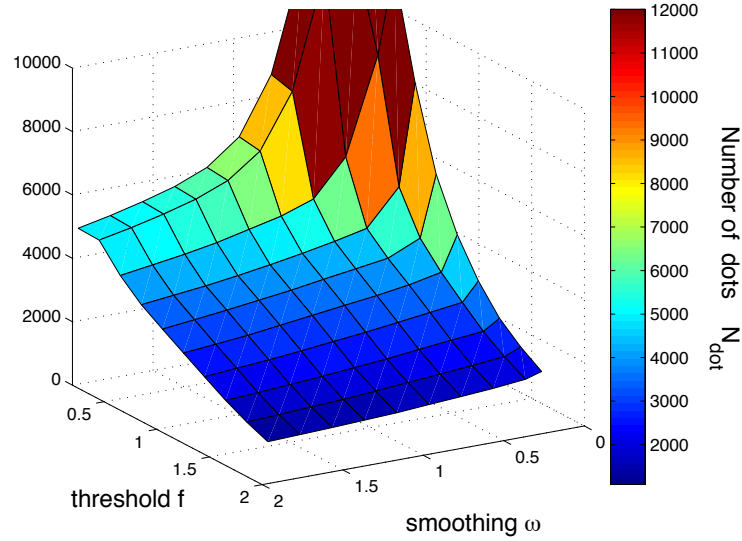


**Figure 6.4.:** Analysis Optimization. The number of segmented dots estimated by the Dot Segmentation Tool of Stefan Wörz [98] highly depends on the choice of adaptable parameters. To optimize the dot segmentation I studied the the number of segmented dots as a function of the parameters  $\omega$  and  $f$ . When the parameters are chosen high, a lot of signal is excluded and not segmented as dots, resulting in an underestimation of number of dots. When parameters are chosen too low, noise is segmented as dots, leading to an overestimation of dots. Therefore I concluded that noise plays an eminent role when analyzing images using the Tool and so I aimed for reduction of noise and subsequent optimal parameter choice using histograms, Figure 6.5.

threshold is defined by  $T = \mu_h + f\sigma_h$  (where  $\sigma_h$  and  $\mu_h$  are center and width of the noise distribution histogram) a factor around 1 should exclude most of the noise, while including as much signal as possible.

To avoid segmentation of noise, I looked for criteria, that allow for distinction of segmented noise and real dots, since the visual impression was not as accurately as needed (many dots at high concentration confuse the eye). To find this criterium, I plotted the properties of the single dots obtained from the segmentation as histograms. Figure 6.5 (a) shows an example of these frequencies of dot intensities  $i_{dot}$ , the dot size  $s_{dot}$  and the contrast  $c_{dot}$ . In this example only the parameter  $f$  was varied. The histograms show that the variation in number of dots mostly derives from dots of low intensity or contrast, confirming the fact, that noise is wrongly segmented and corrupts the measurement of dots.

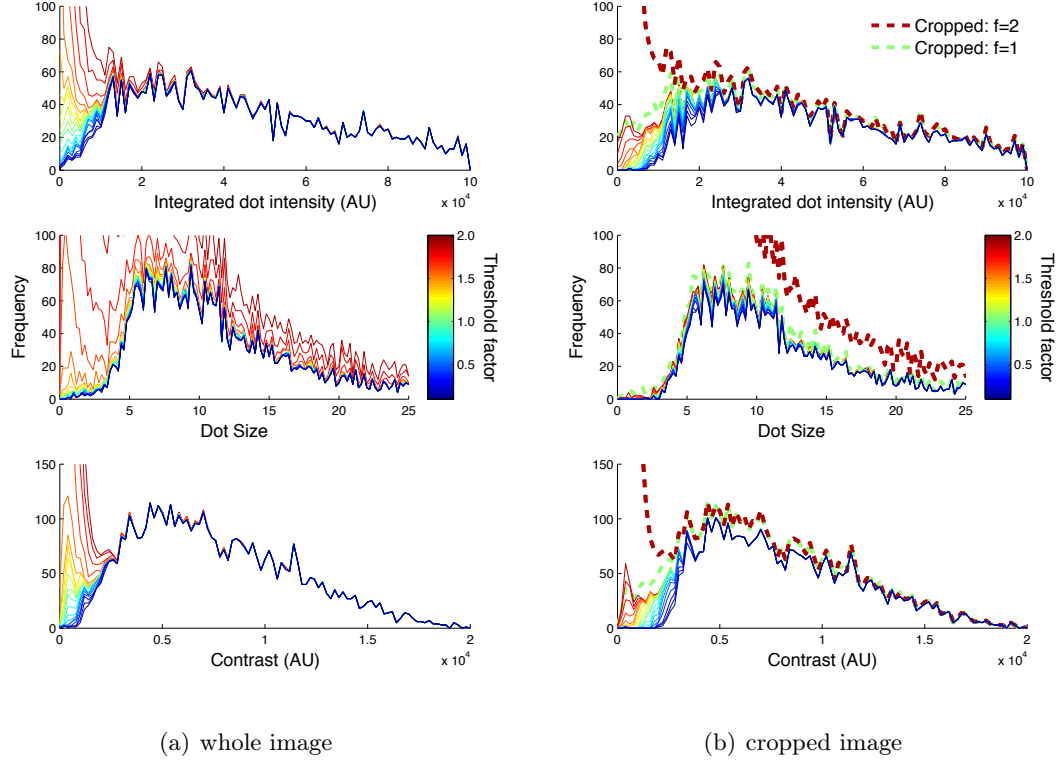


**Figure 6.5.:** Analysis Optimization: One example of frequency histograms of dot integrated intensity  $i_{dot}$ , size  $s_{dot}$  and contrast  $c_{dot}$  for variation of the parameter  $f$ . Similar histograms can be obtained for variation of  $\omega$ . (a) When the analysis parameter is varied the number varies for those dots with low intensities, size and contrast, i.e. for the noise. (b) A lot of noise can be excluded by cropping the image to cell size before analysis.

One of the major improvement is the cropping of the image to the size of the cell, thus excluding a lot of noise and background from the glass next to the cell. Figure 6.5 displays the histograms of an uncropped image that show, that much more noise was segmented as dots. Especially for low intensities and low contrast a lot of noise is raising the frequency values in the histogram compared to the cropped image (black line). Therefore all images were cropped before further analysis.

In order to exclude the noise from the number of segmented dots, the intensity histogram was fit to a lognormal distribution  $f(i_{dot})$ , Figure 6.6, and the area under the curve

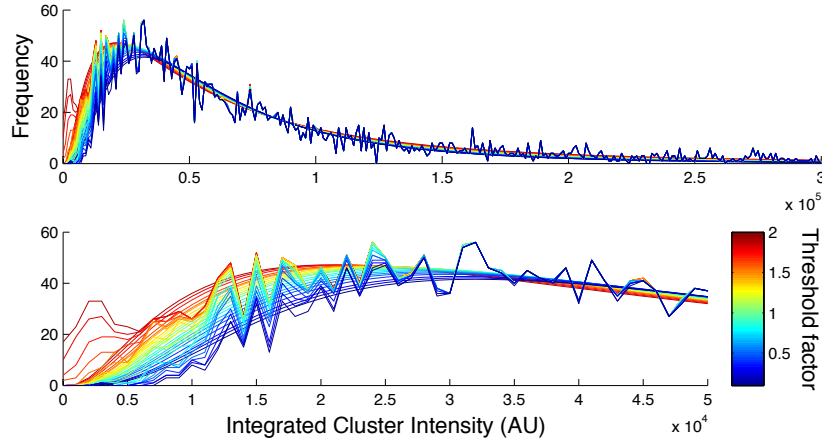


**Figure 6.6.:** Analysis Optimization: The dot integrated intensity histogram , generated by a Matlab tool, can be fit to a lognormal distribution. Integration of this fit will yield a more reliable estimate of the number of dots than simple counting, because it excludes noise.

estimated that corresponds to the number of segmented dots.

$$N_{dot} = \int f(i_{dot}) di \quad (6.1)$$

By fitting the noise is excluded. It is not sensible to fit the dot size  $s_{dot}$  or contrast  $c_{dot}$ , because the former is determined by a combination of the point spread function of the microscope and biological reasonings. Also the latter is not a measure of a real biological quantity and thus not as suited as the integrated intensity.

The histogram and its fit constitute an optimal criterium for the parameter choice. Figure 6.6 and 6.5 refer to  $f = 1$  as optimal, including little noise but maximum signal. Similar histograms for  $\omega$  indicate 0.6 as a good choice. Therefore in the following cells were analyzed with parameters  $\omega = 0.6$  and  $f = 1.0$ .

### 6.1.2. The Number of Dots is Proportional to the Cell Size

By implementing a Matlab analysis of the dot intensity histograms, I have established a tool to optimize the segmentation data from the Dot Segmentation Tool of Stefan Wörz [98] for these specific immunofluorescence images to determine a precise estimate of the number of dots per cell. Using this optimized tool I determined the number of dots on thirty cells of three replicate samples, Figure 6.7.

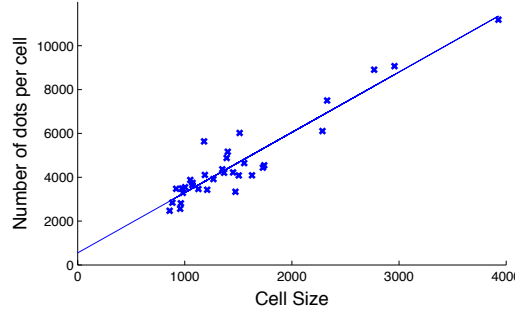


**Figure 6.7.:** The number of dots per cell  $N_{dot}$  is proportional to cell size  $S_{cell}$ : HeLa cells were fixed and CD95 was immunostained with Apo1-3 mouse and anti-mouse Alexa488 antibody. The number of dots was estimated with the Dot Segmentation Tool by Stefan Wörz [98] using the before optimized parameters:  $f = 1$  and  $\omega = 0.6$ .

My first observation was, that the number of dots on the cells  $N_{dot}$  is proportional to cells size  $S_{cell}$ . Cell size here was measured as the projection of the cell on the x-y plane, a good estimate also of the cell volume, because the cells are very flat on the glass. Cell size was estimated automatically by setting a threshold on fluorescent images after checking that this estimate corresponds to an cell size estimate by hand.

$$N_{dot} = 2.7 S_{cell} + 550 \quad (6.2)$$

Furthermore the cell size and thus also the number of dots per cell is lognormal distributed, Figure 6.9 , just like the number of receptors per cell, chapter 4.1.2.

For this number of cells the median can only be estimated inaccurately, demonstrated by the difference between median estimate from data  $\langle N_{dots} \rangle = 4090$  and estimate from the lognormal fit  $\langle N_{dots} \rangle = 3647$ .

### 6.1.3. The Mean Number of Dots per Cell is 4300

To obtain a better estimate for the median number of dots per cell, I used the proportionality: instead of estimating the median from the distribution of number of dots from 30 cells, I estimated it indirectly from the size distribution.

At low magnification and resolution it is easy to acquire big fields of view with hundreds of cells, where the size is automatically analyzed in ImageJ. With a sample number of 600 cells the distribution is more accurately defined, Figure 6.9, and the median cell size estimated from the data corresponds to the median estimated from the lognormal fit.

Using equation 6.2 the mean number of dots per cells was estimated to  $\langle N_{dots} \rangle = 4300$ .

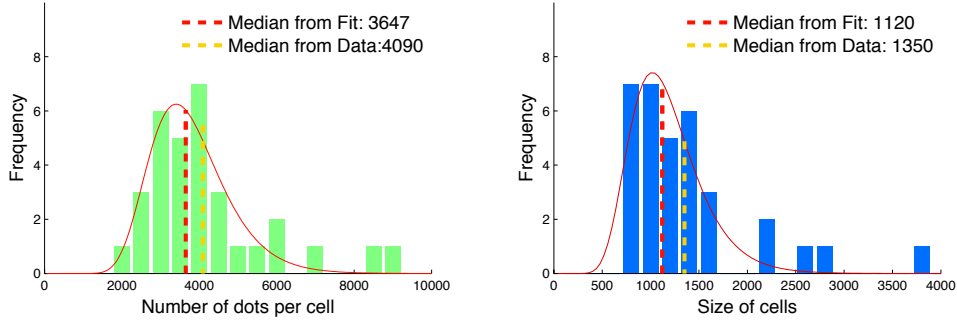


**Figure 6.8.:** HeLa cells were immunostained for the CD95 receptor and segmented using the Dot Segmentation Tool by Stefan Wörz [98]. The number of dots per cell  $N_{dot}$  and cell size  $S_{cell}$  are lognormal distributed. For this relatively small number of cells, the median can only be estimated with a relatively high error, showing the difference between median estimation from the data directly and median estimation from the lognormal fit.

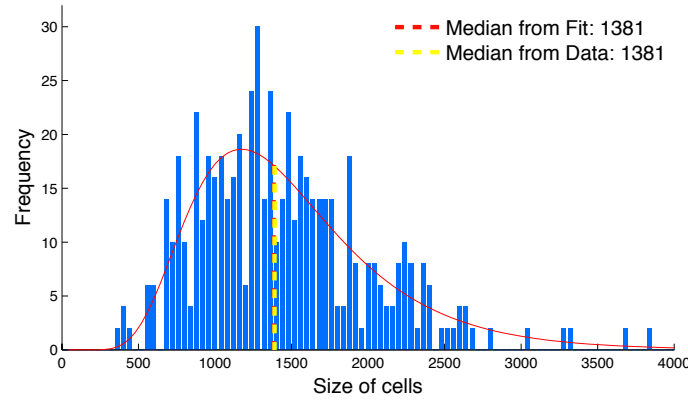


**Figure 6.9.:** More accurate estimate with higher sample size: 600 HeLa cells were immunostained and imaged at low magnification with a large field of view to obtain a high sample number and size was estimated automatically with ImageJ. The histogram allows for a precise estimate of the mean cells size:  $1381 \mu\text{m}^2$ , relating to a mean number of dots  $N_{dots} = 4300$ .

This number can be directly compared to the number of receptors per cell, measured in chapter 4.1.2, since for both measurements exactly the same staining procedure was used. However the number of dots is not yet easy to interpret, because resolution and noise of the microscope will temper with the signal, that not every dot can be seen. Therefore relation between dot number and receptor number will be further discussed and analyzed with a simulation in chapter 6.2.

#### 6.1.4. The Intensity Calibration reveals that most Dots contain less than Three Receptors

There are several ways to estimate the oligomerization state of the receptors on the plasma membrane from the images shown above. While the comparison of dot number and receptor number is discussed in detail later, here I want to take a side trip on what can be learned from the intensities themselves. The intensities of the dots  $i_{dot}$  can be summed up over the whole cell to estimate the cells intensity  $I_{cell}$ . However because of the cell to cell variation this should not yet be related to the receptor number but rather averaged over the number of cells to estimate a mean cell intensity:

$$\langle I_{cell} \rangle = \sum_{N_{cells}} \frac{I_{cell}}{N_{cells}} = \sum_{N_{cells}} \frac{\int f(i_{dot}) di}{N_{cells}} \quad (6.3)$$

This mean cell intensity is exactly the same quantity that was measured in chapter 4.1.2 and corresponds to the measured 20000 receptors per cell.

$$\langle I_{cell} \rangle \Leftrightarrow 20000 \text{ receptors} \quad i_{rec} \Leftrightarrow \frac{\langle I_{cell} \rangle}{20000} \quad (6.4)$$

The receptor intensity in the microscopy images therefore is  $i_{rec} = 13600$  (arbitrary units) so that the intensity scale can be calibrated.

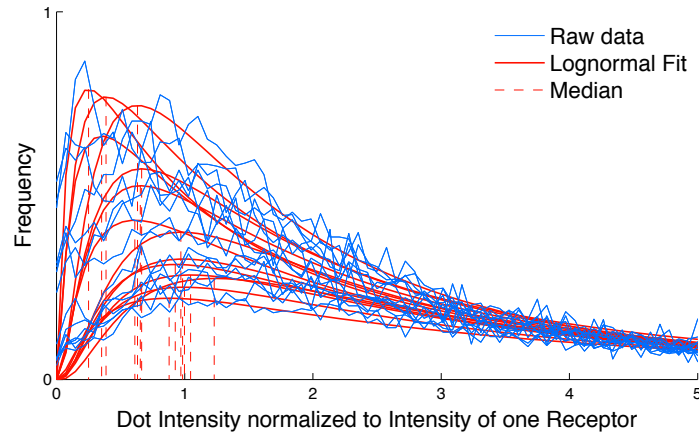


**Figure 6.10.:** HeLa cells were immunostained for CD95, the dotted pattern imaged and analysed (Dot Segmentation Tool by Stefan Wörz [98]) and the intensity histogram generated. Averaging the intensity over 30 randomly chosen cells (only 10 displayed for clarity) allows for a calibration of the intensity axis to single receptor intensity  $i_{rec}$ . The median dot intensity is about  $1 \cdot i_{rec}$ . This indicates that receptors are not massively clustered at the plasma membrane but rather distributed at low oligomerization level.

Figure 6.11 plots the dot intensity distributions  $f(i_{dot})$  for 30 different cells (only 10 shown for clarity). The median dot intensity  $i_{dot}$  for most cells is about or below the intensity for one receptor  $i_{rec}$ .

However a multilevel antibody staining is used, where not every receptor has the same amount of fluorescent dyes. Therefore the dot intensity distribution could origin from a different amount of receptors per dot, but also from a different amount of fluorescent dyes, which can explain dot intensities below the intensity of one receptor.

Furthermore, we do not yet know, whether dots originate from physical clustering of receptors or from randomly near receptors, that by broadening through the point spread function appear as one dot.

The intensity calibration shows, that receptors are not massively clustered on the plasma membrane. If receptors form clusters, the dots do not necessarily correspond to clusters, however they constitute an upper limit for the number of receptors per cluster. The calibrated histogram of dots therefore gives a first indication, that if the receptors form clusters, these are very small (2 to 10 receptors) and the peak of the distribution at 1 indicates that a significant part of receptors will still be monomeric.

#### 6.1.5. The Lower Membrane represents the Whole Cell

To check that staining is also complete on the lower part of the cell and antibodies can enter the space between membrane and glass, I analyzed only the lower part of the plasma membrane and compared to the whole cell analysis.

The analysis of only the plasma membrane for the upper cells yields a number of  $211 \pm 13$  dots per  $100 \mu\text{m}^2$ .

The size of the plasma membrane of whole cells was estimated by microscopy of cells, that were detached and slightly swollen by osmotic pressure, so there were no folds in the plasma membrane. The mean cell surface size is  $2000 \mu\text{m}^2$ . Therefore the whole cell analysis adds up to 215 dots per  $100 \mu\text{m}^2$ .

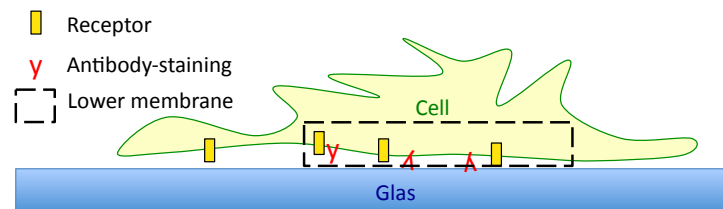


**Figure 6.11.:** Outline of cell position on the glass. The lower plasma membrane lies flat and does not fold massively, while the upper membrane folds into so called filipodia.

The analysis of the lower plasma membrane is in very good agreement with the whole cell analysis, confirming the fact, that the lower plasma membrane is well stained and opening the possibility to only analyze the lower plasma membrane, as will be used for high resolution microscopy in chapter 6.3.

## 6.2. Simulation of the Microscope Characteristics

There are less dots in the images than the receptor density implies. This fact is not easy to interpret. It could be due to a clustering or oligomerization of the receptors, but it could also be that receptors are randomly near to each other and due to resolution width merge to one dot in the image. Additionally the fluorescence of staining is differing and noise is covering part of the signal. Therefore we simulated the different scenarios: randomly distributed monomers or oligomers/clusters. Simulations include the microscopy resolution, background, noise and fluorescence distribution. There are a number of input parameters for the simulation, that were estimated from the experimental data as described in the following. Then a workflow for the generation of in silico images was established using these parameters.

### Input Parameters for the Simulation

**The receptor concentration** in physiological expression on HeLa cells was estimated in chapter 4.1.2 to 10 receptors per  $\mu\text{m}^2$ .

**The median fluorescence of one receptor**  $\langle F \rangle = 2000$  (arbitrary units) was at first roughly estimated single lying dots in the experimental images and refined later, since a priori it is not known, whether single dots correspond to single receptors.

**The antibody fluorescence distribution** is caused by the multilevel staining with primary and secondary antibody, leading to different amounts of fluorophores on different receptors. We determined the fluorescence distribution of the staining measuring primary and secondary antibody, that were bound to glass (Figure 6.12). It is lognormal (equation 6.5) with  $\mu = 5.26$  and  $\sigma = 0.93$ . The normalization factor  $N$  relates to intensities of this particular measurement and is not comparable to experiments in cells.

$$F = N * \left( \exp \frac{-(\mu^2 + \log x)}{2\sigma^2} \right) / \sqrt{2\pi x \mu} \quad (6.5)$$



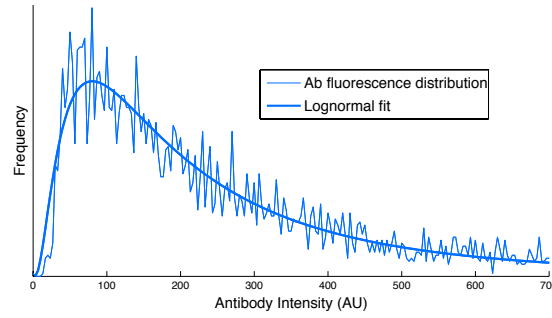


**Figure 6.12.:** Fluorescence distribution of the antibody staining. Apo1-3 mouse antibody was absorbed to glass surface, blocked and then stained with anti-mouse-Alexa488 antibody. The antibodies were imaged and images segmented and evaluated as in chapter 6.1 to obtain the intensity histogram.

**The spatial resolution** was determined on single lying dots in the experimental images and adds up to  $230 \pm 12$  nm.

**The background intensity and noise** was determined on not stained ROIs inside the cells and fit to a gaussian distribution with mean  $\mu_h$  and width  $\sigma_h$ .

## Workflow of the Simulation

**Receptor coordinates and fluorescence intensities:** I simulated 1000 receptors in three dimensions for an area of  $100 \mu\text{m}^2$ . Coordinates were generated with a random number generator for every receptor, for the case of oligomers coordinates for the first receptor were randomly generated and set to the same value for the other receptors of the oligomer. The fluorescence value for every receptor was also randomly generated, but here a special plugin had to be used, so that fluorescence values follow the experimentally determined lognormal distribution values  $\langle F \rangle$ ,  $\sigma$  and  $\mu$ , that were determined before.

**Broadening with point spread function:** the fluorescence intensity distribution was convoluted with the point spread function of the microscope to account for the measured spatial resolution.

**Pixelization:** the intensity distribution was binned into pixels in order to obtain a 16bit-3D-image of size  $100 \mu\text{m}^2 \times 1.5 \mu\text{m}$  and pixel size  $83 \text{ nm} \times 83 \text{ nm}$ ).

**Noise and background generation:** background and random noise, following a normal distribution with  $\sigma_h$  and  $\mu_h$  as determined from the experiment, were added to every pixel of the image

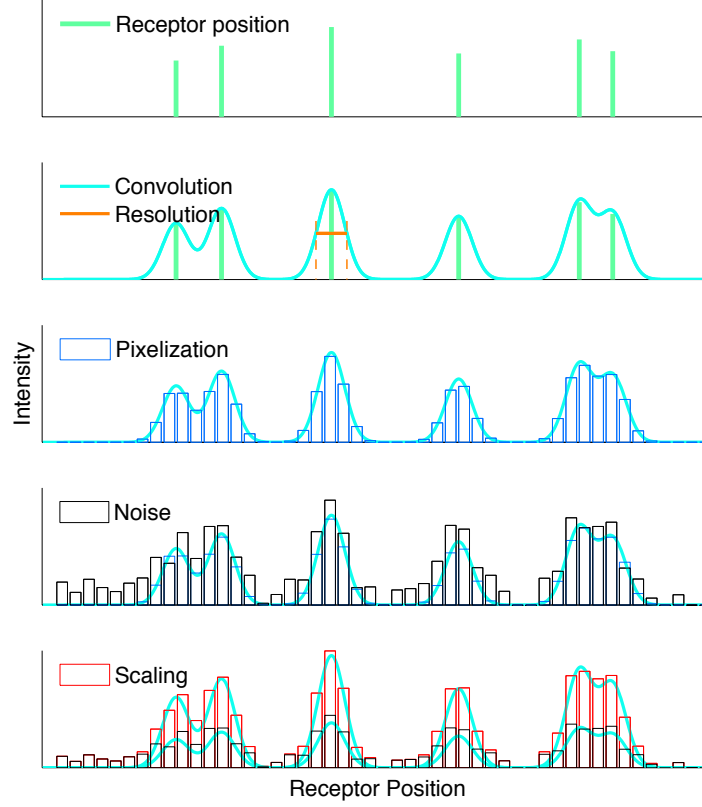


**Figure 6.13.:** Generation of in silico images: Step 1: generate receptors with coordinates and fluorescence intensity that follow the lognormal distribution. Step 2: Convolve with the points spread function. Step 3: pixelize to a 16bit image of pixel size 83 nm. Step 4: add noise and background according to experimental distribution. Step 5: iteratively re-adjust receptor intensities  $\langle F \rangle$  to yield the experimental dot intensity  $i_{dot}(exp)$

**Adjusting fluorescence intensities:** as discussed before the median fluorescence  $\langle F \rangle$  of single receptors can not be determined from the experimental images directly and therefore was approximated before. In this last step this input value was adjusted in an iterative process by comparing the brightness of dots  $i_{dot}(sim)$  (output value) of the simulations to the experimental images  $i_{dot}(exp)$ .

### 6.2.1. In Silico Images

Using this workflow, in silico images for the three different scenarios were generated: the receptor being monomeric, dimeric or trimeric, Figure 6.14.

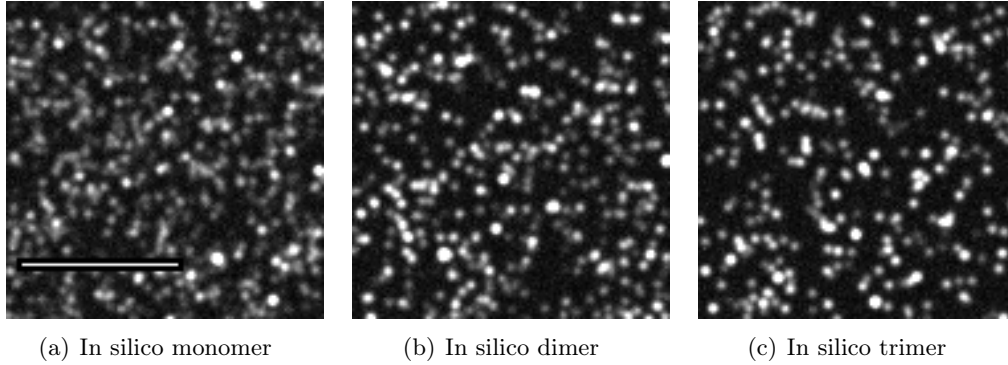


**Figure 6.14.:** In silico images for each of the three scenarios. Following the workflow represented in Figure 6.13 for every scenario 20 images of size  $100\mu\text{m}^2$  were generated with the experimentally determined resolution 230 nm. Scale bar:  $5\mu\text{m}$

To test variation from randomness, 20 images were generated for every scenario, that from the visual impression are all similar to the shown examples in the Figure. In the following error bar will indicated this variation due to randomness.

### 6.2.2. Many Oligomers contain less than Three Receptors

The reason for simulation was to test whether the low number of dots, compared to number of receptors is due to a clustering of the receptors or whether the random distribution paired with resolution and noise leads to a visual merging of receptors that are not actually clustered. Therefore a criterium to compare simulation and experimental images is needed since the visual impression here might not be reliable.

Hence I chose the number of segmented dots using the Dot Segmentation Tool of Stefan Wörz [98] as criterium for comparison of the simulation to the experiments, Figure 6.15. To estimate the suitability of this quantity for a comparison I considered the possible sources of error.

One possible source of error is the sensitivity of the Dot Segmentation Tool of Stefan Wörz [98] to the adaptable analysis parameters, as was discussed in chapter 6.1. However this error source was excluded by exactly modeling all image properties such as noise, background, resolution to best approximate the experimental images. Therefore in silico images are analyzed with exactly the same analysis parameters as the experiment to exclude this source of error.

A second possible source of error is the image resolution. As described earlier the resolution is one of the main reasons, that could lead to a merging of receptors in the image that in reality are separate. The resolution, i.e. the width of the point spread function, was measured on the experimental image and is  $230 \pm 12$  nm.

To test the error arising from a little variance of the resolution, I generated further images with the resolution 218 nm and 242 nm and determined the number of dots as before, Figure 6.15. Already by eye one can see that the uncertainty of the power of resolution makes a comparison of simulation and experiment difficult. It is impossible to distinguish between the scenario of monomers and dimers. A T-Test shows that depending on the assumed power of resolution, either the scenarios "monomers" or "dimers" are more likely. Furthermore one could assume distributions of oligomerization including monomers, dimers and higher oligomers.

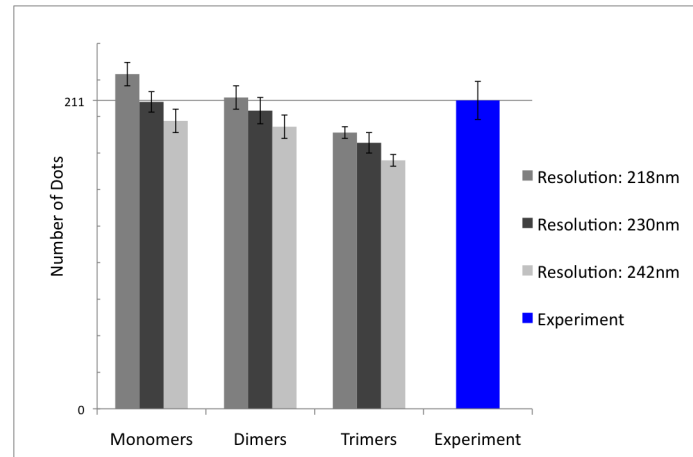


**Figure 6.15.:** Discrimination between the scenarios by number of dots per  $100 \mu\text{m}^2$ : The error bar represent cell-to-cell variation on the experiment, for the simulations they represent the variation due to randomness of input parameters.

Monomers	Dimers	Trimers	Resolution
$10^{-3}$	<b>0.67</b>	$10^{-5}$	<b>218 nm</b>
<b>0.6</b>	0.03	$10^{-13}$	<b>230 nm</b>
0.007	$10^{-3}$	$10^{-9}$	<b>242 nm</b>

**Table 6.1.:** T-Test for the comparison of experimental data to in silico images in Figure 6.15.

The comparison of simulation and experiment allows for one certain conclusion: A biological scenario where CD95 is systematically trimerized on the plasma membrane can be excluded. To achieve images with this number of dots, a substantial part of the receptors must present itself as monomers or dimers on the plasma membrane. This statement could only be found through modeling of the microscopy characteristics, since the mere numbers: 4300 dots and 20000 receptors would suggest a higher clustering, rather than excluding sheer trimerization.

Furthermore simulation indicates that the power of resolution plays a key role for discrimination between monomers and dimers at physiological receptor concentrations on HeLa cells. To illuminate the oligomerization level more, I aimed for high resolution microscopy techniques.

### 6.3. Stimulated Emission Depletion allows for Higher Resolution of Clusters

**STED imaging was performed in collaboration with Matthias Reuss (Stefan Hell, Optical Nanoscopy in Bioquant)**

The spinning disc imaging and analysis in chapter 6.1 have shown that in HeLa cells CD95-receptors are not massively clustered on the plasma membrane at physiological expression. Notably I used two methods to estimate the amount of oligomerization.

One method was to determine the distribution of the dot intensities. By calibrating the intensity scale using cells with known amounts of CD95-mGFP, I estimated the number of receptors per dot. This number is lognormally distributed with a peak between one and two receptors. However one dot does not necessarily correspond to only one receptor oligomer, but might comprise more than one. Therefore the distribution of oligomers might be shifted to even smaller numbers of receptors per cluster, indicating that a big part of receptors presents itself in the range of monomers or dimers, chapter 6.1.4.

The other method was to simulate the random nature of oligomer distribution and the microscopy features, particularly the resolution, assuming three possible biological scenarios, monomeric, dimeric or trimeric receptor. The simulations for a constitutive trimer could not explain the high number of dots that were observed in the experiment indicating that an eminent part of the receptors is monomeric or dimeric at the plasma membrane.

Both of these complementing analysis methods, the calibration of the intensity scale and the simulation of the random receptor distribution, speak for a large fraction of oligomers lower than trimers.

On the other hand the simulation illustrated the fact that one limiting aspect of these experiments was the resolution. Therefore I performed the high resolution technique stimulated emission depletion microscopy (STED) on the receptor in collaboration with Matthias Reuss from the group of Stefan Hell: optical nanoscopy.

### 6.3.1. STED Imaging of CD95

To shed more light into the question of oligomerization level, the receptor was imaged with the high resolution technique stimulated emission depletion (STED) in collaboration with Matthias Reuss (Optical Nanoscopy, Stefan Hell) and then analyzed analogously to before, chapter 6.1.1.

To image the receptor with STED the same staining procedure as for spinning disc imaging, chapter 6.1, and flow cytometry, chapter 4.1.2, was used making a direct comparison to these experiments possible. However the fluorescent dye had to be optimized to the laser line of the instrument.

We tested anti-mouse antibodies with fluorescent dyes ATTO-647N and ATTO-635 both suited in terms of laser wavelength of the stimulating and the depleting laser. The ATTO-647N antibody proved to be brighter (higher signal to noise ratio) and since it is less lipophilic exhibited less unspecific signal in the control (data not shown). Therefore staining was performed as before using anti mouse ATTO-647N antibody (H+L).

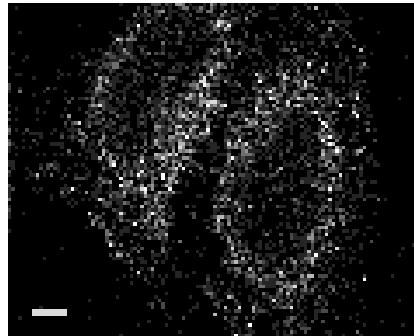


**Figure 6.16.:** A pre-scan at low resolution serves as an orientation for the positioning under the nucleus. The same settings are used for focussing on the lower plasma membrane. Scale bar 5  $\mu\text{m}$ .

The laser power of the depleting laser is orders of magnitude higher than the exciting laser and these high energies lead to a relatively high bleaching. For this particular sam-

ple bleaching allows only for one high resolution image to be taken and not stacks of cells.

As shown before the lower plasma membrane under the cell nucleus is a good representation of the whole cell membrane regarding receptor distribution. Therefore low resolution pre-scan was used to choose ROIs that lie directly beneath the nucleus and for focussing on the lower plasma membrane, Figure 6.16. Then one high resolution image was acquired at the predefined location, Figure 6.17.

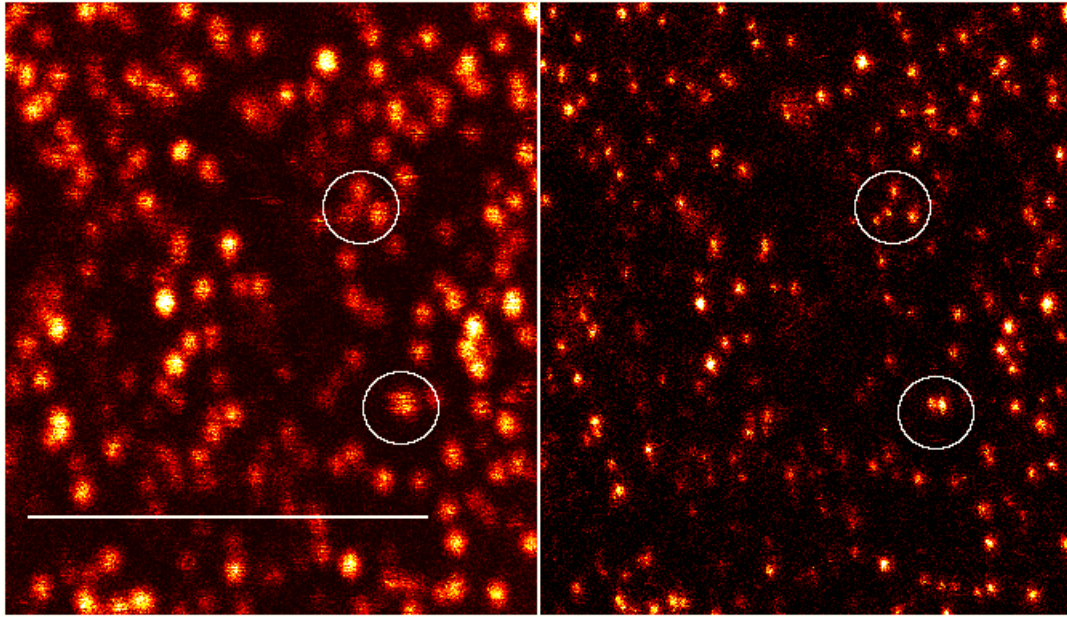


**Figure 6.17.:** High resolution microscopy of CD95 receptor: HeLa were immunostained for CD95 with ms APO-1-3 and  $\alpha$ -ms ATTO-647N antibody. The lower plasma membrane beneath the nucleus was imaged with stimulated emission depletion microscopy. Left: confocal resolution. Right: same position at STED resolution. ROIs mark receptors, that could not be resolved at confocal resolution, but could be resolved at STED resolution. Scale bar 5  $\mu$ m.

Figure 6.17 demonstrates that stimulated emission depletion allows for the resolving of dots that were merged into one at confocal resolution.

Having established the protocol for sample preparation and imaging, we imaged the lower plasma membrane of 20 randomly chosen cells for a comparison to Spinning Disc imaging and analysis of oligomerization levels as described before.

## 6.4. The Simulation of the Characteristics of STED Images

The simulation of STED microscopy is mainly analogous to the simulation of Spinning Disc images. The input parameters have to be adapted to the different images, as later described. However two characteristic features need to be added for STED microscopy simulation that are intrinsically different from a physical point of view to those of the confocal images, namely STED has a different very characteristic point spread function and due to low photon count per pixel the shot noise has to be considered as an additional feature for the simulation.

For the STED microscopy cell were stained with an antibody fused to fluorophor ATTO 647N instead of Alexa488 that was used for the spinning disc microscopy. To account for this the antibody was attached alone to glass, the fluorescent dots measured and segmented and the fluorescence distribution of the antibody was determined, analogous to the measurement of the Alexa488 antibody fluorescence, chapter 6.2. Furthermore the values for detector noise and background were determined on ROIs in the experimental STED images that contained only background and no signal.

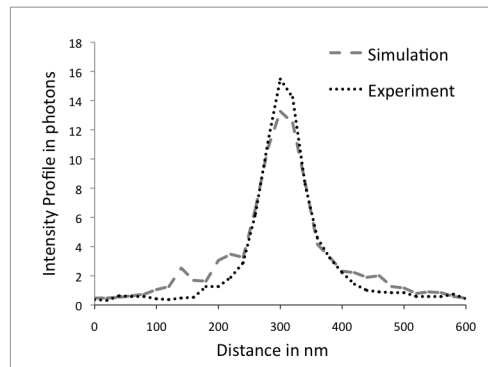


**Figure 6.18.:** The point spread function of the in simulated images corresponds to the experimental images. The characteristic basement around the peak of the STED point spread function was simulated with a gaussian of width 240 nm.

One of the additional features implemented for STED simulation is the shape of the point spread function (PSF). As described in the introduction, chapter 2.2, the PSF for STED differs from the confocal not only in the width to account for the higher resolution but also in the shape of the function, since it is not a gaussian peak but has an additional characteristic basement around the center of the peak. This basement can be interpreted as a 'local background' that disturbs image analysis and therefore needs to be included in the simulations. In the simulation the basement was implemented as an additional gaussian curve with a much larger width of 240 nm and lower amplitude than the central



peak of the point spread function, giving a good approximation to the experimentally measured PSF, Figure 6.18.

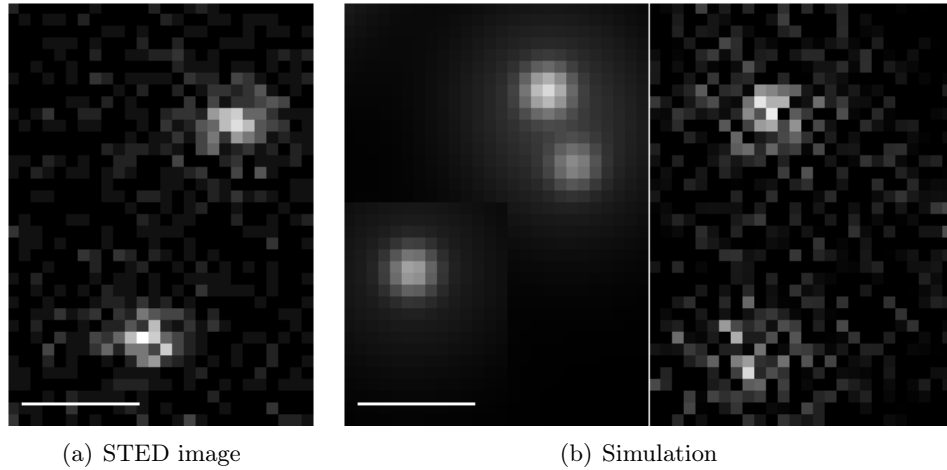


**Figure 6.19.:** To achieve a higher comparability of the *in silico* images with experimental data the shot noise was included in the simulation. (a) Experimental image with clearly visible shot noise. (b) Simulation left without and right with shot noise. Scale bar 200 nm.

The second STED feature that was implemented additionally is the shot noise. The shot noise differs fundamentally from other kinds of noise in the fact that it is not a constant random distribution but differs as a function of the signal. In the simulations of confocal imaging the shot noise was disregarded since it can be neglected against other sources of noise that were implemented. In STED imaging however, due to the high resolution and thus small pixel size, integration times per pixel become smaller, leading to a lower number of photons per pixel than at confocal resolution, e.g. typical number of photons per pixel in a peak are between 20 and 30, while background ranges between 0 and 1. Therefore the shot noise is quite high and being the square root of photon counts

$$N_{\text{shot}} = \sqrt{\text{number of photons}}$$

is not a constant distribution for all the pixels, as in confocal microscopy, but varies highly. In the simulation the shot noise was implemented as a gaussian distribution of width one multiplied by the square root of the signal of the pixel. Figure 6.19 demonstrates the effect of including shot noise in the simulations to achieve a good approximation to the experimental image.

With the additional features of STED point spread function and the shot noise the sim-

ulation is well adapted to approximate STED images. Again I used the simulation to generate *in silico* images of the three biological scenarios, the receptor being monomeric, dimeric or trimeric and compared these to the experimental images using as criterium the number of dots estimated by image segmentation of the dots.

#### 6.4.1. CD95 on HeLa Cells is either Dimeric or a Mix of Oligomers with a Mean of Two Receptors per Cluster

To determine the oligomerization status of the receptor I generated *in silico* images of monomeric, dimeric or trimeric receptors, Figure 6.20, in order to compare these to the experimental data, Figure 6.22.

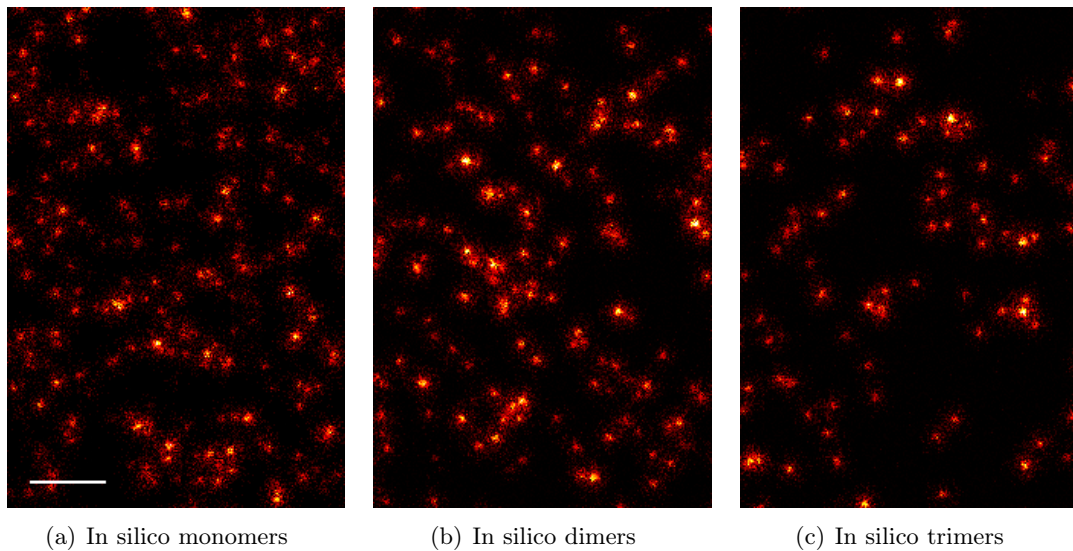


**Figure 6.20.:** *In silico* images of the three different biological scenarios. To discriminate between the three different models, the receptor being monomeric, dimeric or trimeric, *in silico* images were generated using the simulation workflow from chapter 6.2 including the additional STED-specific features of the point spread function and the shot noise. *In silico* images were compared to the experimental images by dot quantification using the dot segmentation tool in an analogous way to chapter 6.2.2. Scale bar 1  $\mu\text{m}$ .

To compare experimental and *in silico* images I used the criterium the number of dots determined by the image analysis tool, analogously to the comparison at confocal resolution, chapter 6.2.2. Also the images analysis tool had to be adapted to the special properties of the STED images. Due to the very small intensity values, resulting from

the small pixel size in STED imaging, image analysis appeared to be even more sensitive to the analysis parameters, than Spinning Disc images.

Therefore Bjoern Bachmann, in the context of an internship under my supervision, implemented an image analysis tool determine best analysis parameters, by comparing the STED images and confocal images of the same ROI. When imaging receptors at the lower plasma membrane the signal of STED images is about a third of the photon count of confocal images. Therefore dot recognition, i.e. the separation of the signal from the noise is more precise on confocal images, while STED images provide a higher dot resolution, i.e. the separation of two dots. The image analysis tool was established to combine these two benefits, namely to use the information from the confocal images, to exclude segmentation parameters that results in many wrongly segmented dots in STED images.

The workflow was as described in the following. STED images were segmented with varying parameters for dots with the image analysis tool provided by Stefan Woerz, chapter 3.8. The results of these segmentations were used to generate artificial images at confocal resolution. In order to choose reasonable parameters for image segmentation these artificial confocal images were compared to the experimental confocal images of the same ROI and those parameters were chosen, that provided best accordance between artificial and experimental confocal images. The best parameters, see chapter 3.8 influence of parameters, appeared to be a smoothing factor of 1.6, a threshold factor of 0.7 and a fitting ROI of 6, as applied to the experimental image in Figure 6.22.

The validity of this image analysis was proven to be high by comparison to manual analysis, Figure 6.21. Error bars represent the cell to cell variation, estimated as a standard deviation.

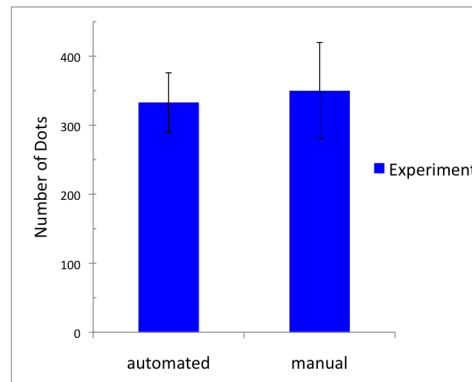


**Figure 6.21.:** Validity test for automated image analysis: the number of dots estimated by the automated dot segmentation corresponds to the number of dots estimated by manual analysis within the standard deviation.

With this, we established a tool for image analysis that was used to analyse the STED images. HeLa cells were immunostained for CD95 and the dotted pattern of the receptor at the lower plasma membrane was imaged with STED. The mean number of dots per  $100\text{ }\mu\text{m}^2$  was estimated to  $333 \pm 43$ , cell to cell variation.

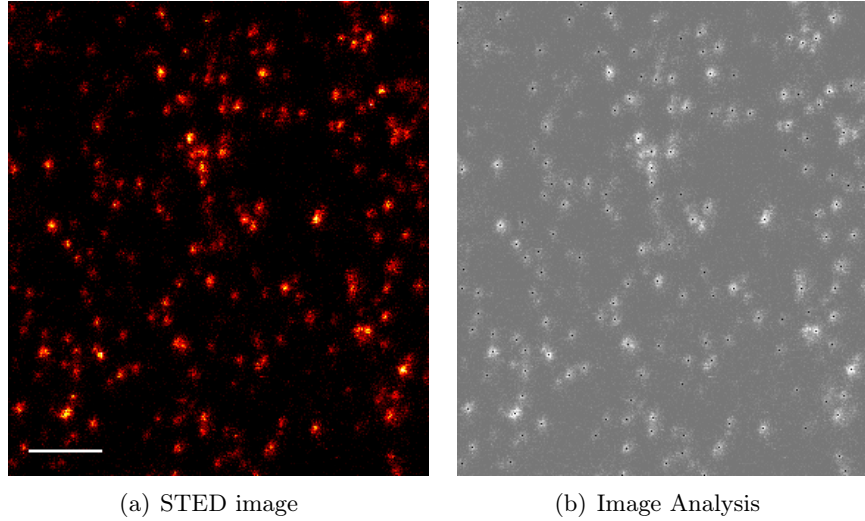


**Figure 6.22.:** High resolution microscopy of CD95 receptor: HeLa were immunostained for CD95 with ms APO-1-3 and  $\alpha$ -ms ATTO-647N antibody. The lower plasma membrane beneath the nucleus was imaged with stimulated emission depletion microscopy. Images were analysis with the image analysis tool described above using same parameters as for the analysis of the in silico images. Scale bar  $1\text{ }\mu\text{m}$ .

To test, which models scenario is in best accordance with the experiment, both experimental and in silico images were segmented and dot number compared, Figure 6.23. The error bar represents the cell to cell variation for the experimental images, respectively the variation due to the random nature of receptor distribution in the in silico images. Just as for the spinning disc images in chapter 6.2.2 the resolution of the experimental images can only be determined to a certain accuracy,  $(71 \pm 3)\text{ nm}$ . Therefore simulation were performed at the different resolutions within the error of the measured resolution.

The comparison to simulations of the biological scenarios shows a correspondence to the the scenario of receptor dimers. This however does not take into account the very likely possibility of a mix of oligomers that on average appears as a dimeric receptor. The T-test , table 6.2, confirms the scenario of constitutive receptor monomers as well as of constitutive receptor trimers can be excluded.

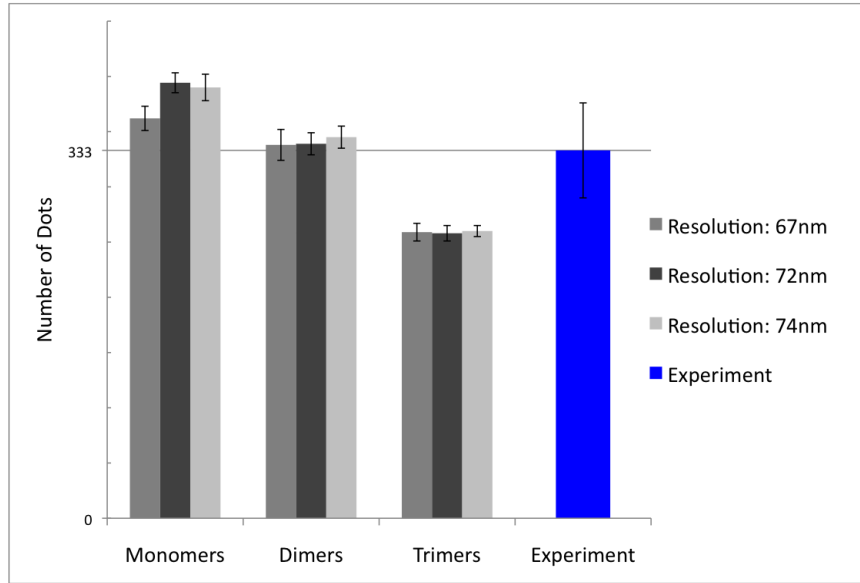


**Figure 6.23.:** The three in silico models are compared to the experimental images using the number of dots per  $100 \mu\text{m}^2$  as discrimination criterium. For the experiment the error bar represent the cell to cell variation, for the in silico images error bars represent the variation due to randomness of receptor distribution. The models of exclusively trimeric and of exclusively monomeric receptor can be excluded, see also T-test in table 6.2. The experiment corresponds to the scenario of receptor dimers whereupon a mix of oligomers is a likely model for receptor distribution on HeLa.

The resolution does not play a significant role compared to the variation of dots numbers due to randomness in the simulations.

Monomers	Dimers	Trimers	Resolution
0.06	<b>0.72</b>	$10^{-5}$	<b>67 nm</b>
$10^{-4}$	<b>0.65</b>	$10^{-6}$	<b>72 nm</b>
$10^{-4}$	<b>0.41</b>	$10^{-5}$	<b>74 nm</b>

**Table 6.2.:** T-Test for the comparison of experimental data to in silico images in Figure 6.23.

The high resolution STED-analysis of endogenous receptor clustering on HeLa cells shows, that the CD95 distribution on the plasma membrane corresponds best to a scenario of dimeric receptor. The scenarios of receptors being exclusively trimeric or exclusively monomeric can be excluded. However it is reasonable to assume that receptors are present at the plasma membrane in a distribution of different oligomerization levels, as already shown via calibration of the intensity axis with Spinning Disc data in chapter 6.1.4. The mode of the distribution however is at the oligomerization level of dimers.

#### 6.4.2. CD95 is Monomeric in Knockdown Conditions

In the previous chapters, 6.1 and 6.3, I studied the oligomerization level of CD95 on the plasma membrane at physiological expression levels. It was shown, that the receptor is not a constitutive trimer but an eminent amount of the receptors is monomeric or dimeric at the plasma membrane. Furthermore the intensity of the dots that are observed with spinning disc imaging follow a lognormal distribution, according to calibration in chapter 6.1.4, with a peak between one and two receptor intensities. This speaks for a model where receptor oligomerization follows an equilibrium that shifts to higher or lower oligomer sizes according to receptor concentration.

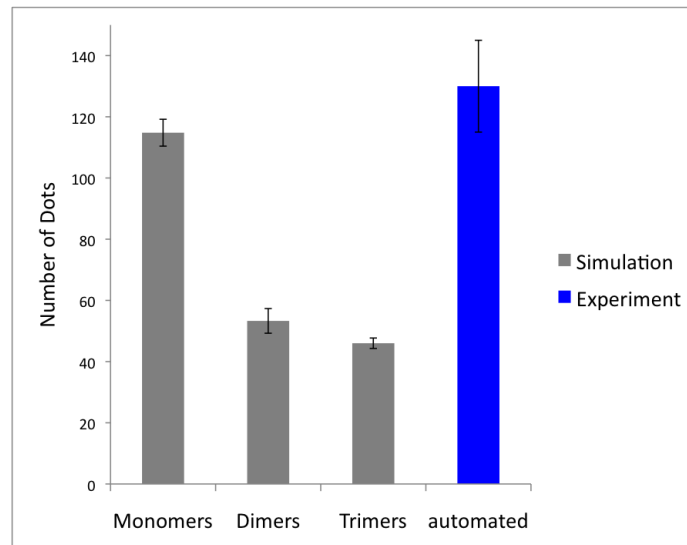


**Figure 6.24.:** The three in silico models are compared to the experimental images in knockdown conditions as before, Figure 6.23. The images of CD95 in knockdown conditions correspond to the scenario of a monomeric receptor.

To test the dependency of receptor oligomerization on the receptor concentration at the plasma membrane, I performed STED imaging at low receptor concentrations using the CD95 knockdown cell line. The low receptor concentration allows for an even better resolution of single receptors so that images show well separated dots.

As in the previous chapter, the oligomerization level is studied by a comparison of the experimental images with simulation generated images of the three biological scenarios, monomeric, dimeric or trimeric receptor. The STED in silico images were generated using the same workflow as in the previous chapter only adapting the receptor amount to that of the CD95 knockdown cells, 3000 receptors per cell. The number of dots was estimated using the image analysis tool as in the previous chapter for experimental and in silico images, Figure 6.24. The error bars represent the cell to cell variation for the experiment and for the simulation the variation due to the random nature of the receptor distribution.

In knockdown conditions i.e. at very low receptor concentrations the CD95 receptor distribution corresponds to the scenario of a monomer. This is in agreement with a model assuming that the receptor is present at the plasma membrane as a mix of oligomers dependent on the receptor concentration and when receptor levels are pushed to low concentrations the oligomers fall apart into monomers.

Contrary to what has been often presumed in literature, I could show via microscopy, detailed image analysis, dot quantification and simulation of microscopy features as well as random nature of spacial distribution, that CD95 at physiological levels on the plasma membrane is not constitutively trimeric. Instead there has to be a significant amount of monomeric or dimeric receptor at the plasma membrane.

High resolution microscopy was used to distinguish between monomeric or oligomeric receptors. The comparison to simulations showed, that the receptor in HeLa cells is not mainly monomeric, but a high amount of pre assembly of the receptor could be observed. This confirms studies, that show receptor pre assembly, and identified a domain, the PLAD, that is responsible for oligomerization.

However when receptor concentration becomes very low, receptors fall apart into monomers, showing the concentration dependence of the binding strength of the PLAD domain.

## 7. Discussion



### 7.1. The CD95 Oligomerization after Induction

CD95 is one of the death receptors and plays an eminent role in apoptosis signaling. Its main function in the organism is in the development of the immune system [12]. There are a number of diseases related to the malfunctioning of this particular receptor [7].

There have been numerous studies on the importance of CD95 oligomerization and clustering in apoptosis signaling. Biochemical experiments have shown a formation of SDS-stable aggregates containing CD95 after induction of the receptor [36], [38], [35]. With the fusion of receptors to fluorescent protein, the formation of signaling protein oligomerization transduction structures (SPOTS) could be observed by microscopy [65], [37].

In Jurkat cells microscopy revealed a recruitment of most receptors to one domain at the cell surface, a process named capping [48], [22].

In this work, I studied the cluster formation in the type II cell line HeLa, which were induced with ILZ-sCD95L instead of the less physiological antibodies. Other experiments in the laboratory, by Clarissa Liesche, have shown that the ILZ-sCD95L is trimeric, like the sCD95L, but has a stronger affinity than the latter. The transiently expressed CD95-GFP was imaged with confocal microscopy at the lower plasma membrane. Within few minutes of induction it was possible to observe the formation of dots. These were intact structures, that stayed intact over time and diffused on the plasma membrane. High quality images allowed for a precise image analysis, making it possible to quantify dots and follow their formation in time. In order to relate to the observations and oligomerization in other studies, I quantified the number of dots and number of molecules per cluster. By relating to receptor concentrations measured via flow cytometry it was possible to calibrate the fluorescence intensity and estimate the number of molecules per dot. The dots are sized following a lognormal distribution with the peak of the distribution at receptor numbers less than 10.

I also characterized aggregation of the receptor by measuring their diffusion coefficients. When molecules aggregate, the radius of the diffusing particles increases, therefore they diffuse slower than non aggregated molecules. Compared to the image analysis of dot formation that is limited by detection, this dynamics measurement is more robust, because it measures receptor populations, but can also be more sensitive, as it is likely to detect small clusters that may not be seen by normal imaging.

Although a decrease in diffusion coefficient correlates with clustering, it is not possible to quantitatively correlate this decrease with the number of molecules per cluster. When lacking structural data about the receptor, as in the case of CD95, one can not precisely estimate the effective radius of the oligomers, since arrangement of the receptors in the oligomer might be differing according to receptor type. There are different models

for receptor diffusion in the plasma membrane, that consider various diffusion hindering mechanisms. While some receptors follow a Stokes-like diffusion model [76], [77] others obey to the Saffman Delbrück model [75]. Therefore diffusion coefficient measurements can be highly sensitive for clustering, as in the case of dimerization measurement of EGF receptors [105]. There again no change in diffusion coefficient does not allow any conclusions on presence or absence of clustering. Furthermore diffusion coefficients are measured on receptor populations and it is not possible to infer on the size distribution of the oligomers.

The features of high robustness and possible high sensitivity for small oligomers make dynamics measurement a good complement for the image analysis of dot formation, that yields quantitative distribution data.

I utilized dynamics measurements to investigate the clustering of CD95-GFP upon induction. Automated imaging allowed for a precise measurement of diffusion coefficient changes. After induction with ILZ-sCD95L, a massive slowdown of the receptor was observed, from  $(0.158 \pm 0.05) \mu\text{m}^2/\text{s}$  to  $0.04 \mu\text{m}^2/\text{s}$  confirming the receptor clustering that was measured by dot formation analysis.

In this study, I used two different methods to observe CD95 receptor clustering in the type II cell line HeLa upon induction with ILZ-sCD95L. This clustering likely corresponds to the aggregate formation observed in type I cell lines as SDS-stable aggregates and SPOTS formation with microscopy. Contrary to other studies, I measured clustering on whole, living cells at a single cell level. Both methods, the dot formation analysis and the dynamics measurement comprehend a quantification of either the dot size or the diffusion coefficient and these values can be measured as a function of time. These values provide a useful criterium to compare receptor clustering at different conditions and furthermore to compare the time scale at which clustering occurs. Thus using these criteria I studied the various proposed clustering mechanisms of CD95 by measuring different receptor mutants.

### 7.2. The Lipid Rafts can be excluded as Oligomerization Mechanism

Various mechanisms have been proposed to be involved in the aggregate formation of CD95 after induction, notable the clustering by the ligand itself, lipid raft relocalization and related actin association of receptors after induction [46], [47], [42], [21], [22] and clustering by the death domain of the receptor [61], [63], [62].

The relocalization of receptors into the lipid rafts is a confinement of the receptor to a cell compartment that possibly leads to high local concentrations, making it one plausible mechanism for CD95 clustering efficient caspase 8 activation and signal transduction. Biochemical evidence shows the importance of lipid rafts for aggregate formation, for the association to the cytoskeleton, receptor internalization and for apoptosis signaling [36]. The palmitoylation site at cysteine 199 constitutes a mechanistic evidence for lipid raft participation as it is responsible for relocating of the receptor to lipid rafts [42] and is essential for the formation of SDS-stable aggregates and cell death [38]. Inhibition of this palmitoylation blocked aggregate formation and reduces caspase 8 activation. Evidence for this derives from biochemical experiments using whole cell lysates and fractionations and receptors were not observed on the plasma membrane. Most studies were performed on type I cells, inducing with agonistic antibodies.

To test whether the formation of dots in type II cell line HeLa is palmitoylation dependent, I studied a mutant C199V, where the palmitoylation site is mutated into a valine that can not be palmitoylated in living cells. Microscopically, the same dots form. Image analysis shows that their size was similar to that of the dots formed by the wild type receptor. The dynamics measurement of the C199V mutant showed the same decrease in the diffusion coefficient as the wild type receptor, indicating that the aggregation of receptors in HeLa is not dependent on the palmitoylation or lipid raft association. Moreover further experiments in our laboratory, by Joël Beaudouin, showed the same aggregation and diffusion coefficient decrease when lipid rafts were destroyed by cholesterol depletion with methyl  $\beta$  cyclodextrin.

Therefore the dots in HeLa cells do not follow the same formation mechanism as those which were shown for the SDS-stable aggregates in type I cells. Dot formation and receptor aggregation after induction in HeLa are independent of lipid raft association and palmitoylation.

### 7.3. The Death Domains can be excluded as Oligomerization Mechanism

Another mechanism involved in clustering is the self-association of the death domains of the receptor. NMR studies on the death domain of CD95 and the complex formation with the FADD death domain suggest that death domains themselves can lead to aggregation. Under acidic conditions a four to four structure could be found, where an opening of CD95 death domain structure exposes a binding site for FADD with promoting receptor clustering, so that the complex functions as a mechanistic switch [62]. However a more recent study using more basic conditions found an asymmetric oligomeric structure composed of five to seven CD95-death domains and five FADD death domain [63]. How-

ever NMR studies of domains of purified proteins at high concentrations do not represent the situation of full-length proteins in the plasma membrane of a living cell. Therefore, this clustering mechanism does not necessarily reflect an active mechanism in living cells. Moreover studies on Jurkat cells, using receptor mutants lacking the death domain, have shown that an intact death domain is indispensable for the formation of SPOTS visible with microscopy [37].

To test the contribution of the death domains in type II HeLa cells I studied a CD95 mutant in which the death domain was deleted. The mutant clustered at the plasma membrane after induction with the ligand at the same speed and size as observed for the wild type receptor. Diffusion coefficient measurements by FRAP confirmed this finding: the mutant showed the same slowdown after induction as the wild receptors.

Therefore we conclude that the mechanism for dot formation and receptor aggregation in HeLa cells does not involve lipid rafts, nor is the clustering caused by death domain aggregation or FADD association. The clustering mechanism, that was observed at high receptor concentrations is likely only caused by the ligand.

### 7.4. The Oligomerization is Concentration Dependent

Most studies on CD95 clustering were performed in one cellular context, without testing the effect of concentrations especially the ones of the receptor.

In this study I calibrated of fluorescence on the microscope to quantify numbers of receptors inside the formed aggregates. With this I could show, that aggregate formation is concentration dependent. Higher concentrations lead to higher aggregates, while at lower receptor concentrations smaller dots are formed. Furthermore I measured receptor oligomerization after induction at physiological expression levels (data not shown), but could not observe a further clustering after induction, indicating that at these relatively low concentrations further clustering by induction is below the detection limit. These data at overexpression and observations at physiological expressions show the importance of initial receptor concentrations on the plasma membrane for the clustering after induction.

The role of receptor concentrations was also tested in CD95 knockdown clones, where flow cytometry measurements revealed that cell death percentage after induction is proportional to the CD95 concentration on the cells, chapter 3.1. Generally I could observe in the laboratory that CD95-overexpressing cells die faster than the same cells with physiological CD95 expression levels. Both observations show that the function of CD95 is

highly correlated to its concentration on the plasma membrane.

To complement the many studies at high receptor concentrations - most of them involve biochemical evidence or NMR studies of the purified receptor - I characterized the receptor distribution on the plasma membrane of living cells at physiological expression levels.

### 7.5. Oligomerization on the Plasma Membrane at Physiological Expression Levels

Most evidence for the oligomerization levels of CD95 is drawn by analogy to the other members of the TNF receptor superfamily [60], [54].

There are different evidences speaking for a pre-ligand assembly of the receptor. Dominant interference of some CD95 mutants causing the disease called ALPS (autoimmune lymphoproliferative syndrome) of the receptors can only be explained by a pre-ligand assembly of the receptor. A special domain at the N-terminal part of the TNF receptors, the so called PLAD, has been shown to be responsible for this assembly and has been confirmed for CD95 on ALPS mutants. CD95 has not yet been crystallized as a whole protein. Therefore structural data are taken from NMR data of single domains or in analogy to TNF structures. CD95 ligand is most likely trimeric. Therefore the receptor is often assumed to be trimeric [3]. However direct evidence is still lacking. In fact there is evidence that TNFR-1, CD27 and CD40 (other receptors of the TNF-receptor family) are dimeric through intermolecular disulfide bonds [54], [58] .

I characterized the receptor distribution at physiological expression levels on the cell plasma membrane with confocal microscopy. For this protocol for staining and imaging of the receptor was established. With spinning disc confocal microscopy it was possible to image the endogenous CD95 receptor in three dimensions and resolve the spacial distribution as a dotted pattern on the plasma membrane. To study the distribution of dot intensities and relate to receptor amount, I established an image processing pipeline: dots are segmented by the dot segmentation program and dot intensity histograms are generated, that show a lognormal distribution of dot intensities. Analysis of these intensity histograms provided a precise estimate of the number of dots per cell and revealed that dot intensity distribution is lognormal. By calibrating the intensity it was shown that the dots at the peak of the distribution contain around between one and two receptors per dot.

This characterization of the intensity distributions is not enough to conclude on the oligomerization of the receptor as they can be randomly near to each other, so that due to limited resolution they appear as one dot. A simple calculation tells us, that equally

distributed receptors would a distance of about  $0.3\mu\text{m}$ , which approximates the limit of resolution. Therefore I performed a simulation to regard the randomness of location and the microscopy features. Notably the resolution, but also the noise, background and fluorescence distribution of the antibodies were modeled following the parameters of the images in order to generate in simulated images of the receptors. These simulations showed that in fact, the limit of resolution and the random nature of receptor distribution and staining play an eminent role, when analyzing the dotted pattern of receptor distribution.

The simulation was used to generate *in silico* images of three scenarios: namely a monomeric, dimeric or a trimeric receptor, with all the characteristics of the experimental images. A comparison of *in silico* and experimental images showed that the scenario of the receptor being trimeric can be excluded. A separation between monomers and dimers was not possible, and this limitation could directly be referred to the limitations in resolution.

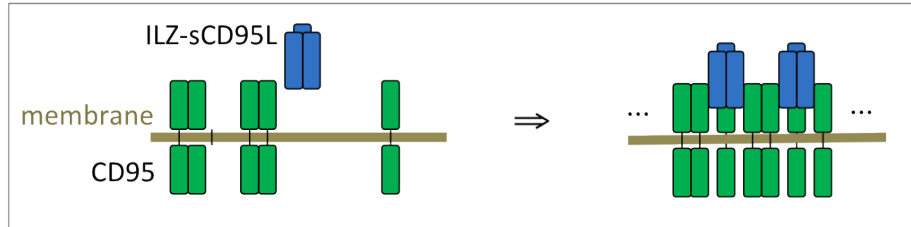
Therefore considering the intensity distribution and image simulation I found that on HeLa cells at endogenous expression levels a large fraction of the receptor must be monomeric or dimeric. This is in contrast to the typical assumption in literature of a constitutively trimeric receptor.

Furthermore the simulations demonstrated the central importance of resolution for microscopic measurements of receptor clustering. Therefore in a collaboration with Matthias Reuss from the group of Stefan Hell, optical nanoscopy, high resolution microscopy with stimulated emission depletion (STED) was performed. The receptors were imaged in two dimensions at the lower plasma membrane of the cell beneath the nucleus at a resolution of  $70\text{ nm}$ . A comparison could show that high resolution allows for the separation of spots, that were merged by diffraction in confocal images.

I performed analogous simulations considering the different features such as form of point spread function and shot noise. The high resolution allowed for a discrimination between the possibilities, distinctly excluding a scenario of exclusively monomeric receptors on the plasma membrane. The experiments were consistent with the simulation of dimers, however one can not exclude the plausible possibility of a mix of populations. However the experiment is consistent with a pre-assembly that was experimentally observed at high concentrations and with the role of the PLAD-domain to oligomerize the receptors in the absence of the ligand.

When exploring knockdown conditions, meaning even lower receptor concentrations, simulations of receptor monomers are in good agreement with the data in the receptor falls into monomers. This indicates, that at lower concentration levels, the receptor falls into

monomers, showing that the mechanism of pre-ligand assembly is concentration dependent.



Combining the experimental results I propose the second of the four models introduced in chapter 1.2.2 for receptor clustering and related apoptosis sensitivity. The receptor clustering mechanism is determined by a pre-ligand assembly of the receptor and a crosslinking by the ligand. Simulations allow to exclude the proposed model of a constitutively trimeric receptor. Instead oligomerization is a dynamic process and the receptor is present as a mixed distribution of different oligomerization levels that depend on the initial receptor concentration. This distribution is shifted towards monomers or dimers for physiological concentrations and can experimentally be shifted towards monomers by a knockdown of the receptor. Moreover also the death-inducing function of the receptor is correlated with the initial receptor concentration.

Upon induction the ligand crosslinks the receptor. This crosslinking alone is a strong mechanism that can lead to massive formation of detectable dots with seven and more receptors per dot. It highly depends on the initial receptor concentration. Additional experiments in our laboratory indicate that one other critical feature for the cell death inducing function it is the affinity of the ligand to the receptors.

Therefore I propose a model, where the sensitivity of a cell to CD95 induced apoptosis correlated to the receptor clustering that is defined by two critical features: the initial receptor concentration and the ligand affinity.

## A. Appendix



## A.1. Estimation of the Diffusion Coefficient from the Bleaching Profile

To determine the diffusion coefficient from recovery of a bleached stripe, one has to relate the spacial intensity pattern of a stripe in the images of every time point to diffusion equation ((A.1)) in time and space:

$$\frac{\partial I(x, t)}{\partial t} = D \frac{\partial^2 I(x, t)}{\partial^2 x} \quad (\text{A.1})$$

One approach solution is to assume a gaussian profile for the stripe where intensity scales with  $1/\sqrt{2\pi}\sigma$ :

$$I(x, t) = \frac{c_0}{\sigma\sqrt{2\pi}} \exp\left(\frac{-x^2}{2\sigma^2}\right) \quad (\text{A.2})$$

The tryout assumption is:

$$\sigma^2 = 2Dt \quad (\text{A.3})$$

$$I(x, t) = \frac{c_0}{2\sqrt{\pi Dt}} \exp\left(\frac{-x^2}{4Dt}\right) \quad (\text{A.4})$$

Take the derivative of this equation:

$$\frac{\partial I}{\partial t} = \frac{c_0}{2\sqrt{\pi Dt}} \exp\left(\frac{-x^2}{4Dt}\right) \frac{x^2}{4Dt^2} + \frac{c_0}{2\sqrt{\pi Dt}} \left(\frac{-1}{2t}\right) \exp\left(\frac{-x^2}{4Dt}\right) \quad (\text{A.5})$$

$$\frac{\partial^2 I}{\partial^2 x} = \frac{c_0}{2\sqrt{\pi Dt}} \exp\left(\frac{-x^2}{4Dt}\right) \left[ \left(\frac{-2x}{4Dt}\right)^2 - \frac{2}{4Dt} \right] \quad (\text{A.6})$$

$$(\text{A.7})$$

Put these partial derivatives into the diffusion equation ((A.1)) to test, whether our assumptions hold true.

$$\left(\frac{x^2}{4Dt^2}\right) + \left(\frac{-1}{2t}\right) = \left(\frac{-2x}{4Dt}\right)^2 - \frac{2}{4Dt} \quad (\text{A.8})$$

Our Ansatz (A.4) solves the diffusion equation, therefor we can determine the diffusion coefficient  $D$  as the slope in (A.3)

# List of Figures

1.1.	The different functions of apoptosis . . . . .	11
1.2.	Model of the intrinsic and extrinsic signaling pathways . . . . .	13
1.3.	Structure of CD95 . . . . .	14
1.4.	TIRF imaging of FADD crosslinking . . . . .	24
2.1.	Principle of fluorescence depicted on a Jablonski diagram. . . . .	29
2.2.	Setup of a fluorescent microscope . . . . .	30
2.3.	The confocal principle . . . . .	31
2.4.	The Spinning Disc is a method to accelerate scanning . . . . .	32
2.5.	The airy disc describes the intensity pattern, that results from diffraction . . . . .	34
2.6.	The STED principle . . . . .	36
2.7.	Intensity profile of exiting and depleting laser and fluorescent spot . . . . .	37
2.8.	STED setup . . . . .	38
2.9.	The point spread function of STED . . . . .	39
2.10.	Membrane Model of Singer and Nicolson . . . . .	41
3.1.	Flow cytometry measurement of transient transfected knockdown cells. . . . .	49
3.2.	Characteristics of stable knockdown clones. . . . .	49
3.3.	Flow cytometry calibration . . . . .	51
3.4.	Illustration of the dot segmentation performed by the Dot Segmentation Program of Stefan Wörz . . . . .	53
4.1.	Histogram of calibration beads for flow cytometry . . . . .	58
4.2.	Demonstration of protocol optimzation . . . . .	58
5.1.	Receptor localization on the plasma membrane respectively in the endo- plasmic reticulum . . . . .	61
5.2.	Receptor Dot formation on HeLa after ligand induction at high receptor concentrations . . . . .	62
5.3.	Movement of dots on HeLa . . . . .	62
5.4.	Dot formation resulting from different inducers . . . . .	63
5.5.	Dots are not internalized (Immunostaining) . . . . .	64
5.6.	Dots are not internalized (early endosomes) . . . . .	65
5.7.	Outline of pre-processing for dot segmentation . . . . .	66

## LIST OF FIGURES

---

5.8. The number of dots increases upon ligand induction. . . . .	67
5.9. Histogram of fluorescence intensity of dots of one image at one time point. . . . .	68
5.10. Histograms of dot intensity over time. . . . .	69
5.11. The mean and the mode of dot intensity increase over time. . . . .	70
5.12. Example of a FRAP recovery curve . . . . .	72
5.13. Example of a recovery of a bleached stripe on the lower plasma membrane. . . . .	74
5.14. The diffusion coefficient $D$ is estimated by FRAP. . . . .	75
5.15. Linear fit for estimation of diffusion coefficient $D$ . . . . .	76
5.16. Slowdown of the receptor after induction with ILZ-sCD95L . . . . .	77
5.17. Exclusion of error sources for FRAP . . . . .	78
5.18. Dot formation is not palmitoylation dependent. . . . .	79
5.19. Receptor slowdown is not palmitoylation dependent. . . . .	80
5.20. Dot formation is not caused by the CD95 death domain. . . . .	81
5.21. Receptor slowdown is not death domain dependent. . . . .	82
5.22. The dot size depends on the initial receptor concentration. . . . .	83
6.1. 3D-Image of CD95 distribution on the whole cell. . . . .	86
6.2. Life cell imaging of receptor distribution with TIRF . . . . .	87
6.3. Example for Dot Segmentation Tool by Stefan Wörz [98]. . . . .	88
6.4. Analysis Optimization: dependency on adaptable parameters . . . . .	89
6.5. Intensity frequency histograms for Analysis Optimization . . . . .	90
6.6. Fit of Intensity histogram . . . . .	91
6.7. The number of dots per cell $N_{dot}$ is proportional to cell size $S_{cell}$ . . . . .	92
6.8. The number of dots per cell $N_{dot}$ and cell size $S_{cell}$ are lognormal distributed. . . . .	93
6.9. More accurate estimate with higher sample size. . . . .	93
6.10. Receptors are not massively clustered. . . . .	94
6.11. Outline of cell position on the glass. . . . .	95
6.12. Fluorescence distribution of the antibody staining. . . . .	97
6.13. Workflow of the Image Simulations . . . . .	98
6.14. Simulation of Spinning Disc Microscopy. . . . .	99
6.15. Discrimination between the scenarios . . . . .	100
6.16. Positioning for STED microscopy . . . . .	102
6.17. STED microscopy of CD95 . . . . .	103
6.18. Simulation of STED point spread function . . . . .	104
6.19. Illustration of shot noise . . . . .	105
6.20. Simulation of STED images . . . . .	106
6.21. Test of automated image analysis . . . . .	107
6.22. STED microscopy and Dot Segmentation . . . . .	108
6.23. Comparison of experimental and simulated images for HeLa . . . . .	109
6.24. Comparison in knockdown conditions . . . . .	110

# Glossary

**ALPS** autoimmune lymphoproliferative syndrome: disease related to CD95. 13

**Apoptosis** one mode of programmed cell death. 8

**caspases** a group of proteases responsible for the execution of apoptosis. 10

**CD95L** the respective ligand of the CD95 receptor, there are two main forms studied in the lab: the soluble form sCD95L and an artificially trimerized form ILZ-sCD95L. 14

**Confocal Microscopy** a techniques for three dimensional imaging. 26

**Diffusion** a process by which molecules move randomly e.g. due to temperature (Brownian motion). 37

**Expression Levels** proteins expression in cells is regulated tightly, protein expression can vary naturally however especially the transient or stable expression of artificially constructed proteins can vary highly from the endogenous levels. 55

**FADD** Fas-Associated protein with Death Domain, FADD is directly recruited by CD95 (Fas) and connects it to the downstream caspases. 10

**Flow cytometry** a technique to measure full cell (or particle) fluorescent intensities with high statistics. 49

**FRAP** fluorescence recovery after photobleaching is a technique to measure the diffusion of fluorescent molecules by bleaching the molecules in one region and observing fluorescence recovery in that region. 39

**GFP** green fluorescent protein. 26

**HeLa** immortal cervical cancer cell line of type I. 16

**Immunostaining** is a technique to stain proteins in cell by attaching fluorescent antibodies. 48

**Lipid rafts** cell plasma membrane domains that are enriched in cholesterol, glycolipids and sphingolipids. 17

**Lognormal distribution** is a mathematical function the plotted on a logarithmic scale appears as a gaussian. Many proteins are distributed according to a lognormal distribution.. 66

**Nyquist Sampling** follow the rule of Nyquist for the choice of pixel sizes in microscopy. 33

**Palmitoylation** posttranslational modification, attachment of fatty acids, e.g. palmitic acid to an amino acid in a protein, often related to the regulation of the localization in the membrane. 16

**PLAD** pre-ligand-assembly domain, a domain of the CD95 receptor related to its assembly before Induction. 13

**PSF** the point spread function describes the appearance of a point source in imaging. 33

**Resolution** is a quantity to describe whether two sources of light can be discriminated from each other. 32

**Signal** the fluorescent signal in microscopy is proportional to the number of fluorescent molecule and can therefore be used for quantification of clustering. 30

**Spinning Disc** is a microscopy technique that allows a much faster scanning by using 1000 pinholes instead of one at a time. 30

**STED** stimulated emission microscopy is a high resolution technique, that increases resolution of molecule by depleting fluorescent molecules into the surrounding area. 34

**Type I and Type II cells** cells can be classified according to the apoptosis pathway they perform: extrinsic type I and intrinsic type II. 15

**z-vad** a caspase inhibitor that blocks apoptosis. 14

## B. Bibliography

- [1] U. Ziegler. Morphological Features of Cell Death. *News in Physiological Sciences*, 19(3):124–128, June 2004.
- [2] Yaron Fuchs and Hermann Steller. Programmed cell death in animal development and disease. *Cell*, 147(4):742–58, November 2011.
- [3] Shigekazu Nagata and Death Factor. Apoptosis by Death Factor. *Cell*, 88:355–365, 1997.
- [4] B Fadeel and S Orrenius. Apoptosis: a basic biological phenomenon with wide-ranging implications in human disease. *Journal of internal medicine*, 258(6):479–517, December 2005.
- [5] Bartolo Favaloro, Nerino Allocati, Vincenzo Graziano, Carmine Di Ilio, and Vincenzo De Laurenzi. Role of Apoptosis in disease. *Aging*, 4(5):330–49, May 2012.
- [6] B Fadeel, S Orrenius, and B Zhivotovsky. Apoptosis in human disease: a new skin for the old ceremony? *Biochemical and biophysical research communications*, 266(3):699–717, December 1999.
- [7] G Papoff, P Hausler, a Eramo, M G Pagano, G Di Leve, a Signore, and G Ruberti. Identification and characterization of a ligand-independent oligomerization domain in the extracellular region of the CD95 death receptor. *The Journal of biological chemistry*, 274(53):38241–50, December 1999.
- [8] Magdalena L Circu and Tak Yee Aw. Glutathione and modulation of cell apoptosis. *Biochimica et biophysica acta*, 1823(10):1767–1777, June 2012.
- [9] F K Chan. The pre-ligand binding assembly domain: a potential target of inhibition of tumour necrosis factor receptor function. *Annals of the rheumatic diseases*, 59 Suppl 1(suppl I):i50–3, December 2000.
- [10] C Sandu, G Morisawa, I Wegerzewska, T Huang, a F Arechiga, J M Hill, T Kim, C M Walsh, and M H Werner. FADD self-association is required for stable interaction with an activated death receptor. *Cell death and differentiation*, 13(12):2052–61, December 2006.

- [11] Mark P. Boldin, Igor L. Mett, Eugene E. Varfolomeev, Irina Chumakov, Yonat Shemer-Avni, Jacques H. Camonis, and David Wallach. Self-association of the Death Domains of the p55 Tumor Necrosis Factor (TNF) Receptor and Fas/APO1 Prompts Signaling for TNF and FAS/APO1 Effects. *The Journal of biological chemistry*, 270(January 6.):387–391, 1995.
- [12] a. Ashkenazi. Death Receptors: Signaling and Modulation. *Science*, 281(5381):1305–1308, August 1998.
- [13] Shyr-Te et al Ju. Fas(CD95)/FasL interactions required for programmed cell death after T-cell activation. *Nature*, 373:444–448, 1995.
- [14] Donald Bellgrau, Daniel Gold, Helena Selawry, Jodene Moore, Alex Franzusoff, and Richard C. Duke. The role for CD95 ligand on preventing graft rejection. *Nature*, 377:630–632, 1995.
- [15] Thomas S Griffith, Thomas Brunner, Sharon M Fletcher, Douglas R. Green, and Thomas A. Ferguson. Fas Ligand-Induced Apoptosis as a Mechanism of Immune Privilege. *Science*, 270(November):1189–1192, 1995.
- [16] R M Siegel, F K Chan, H J Chun, and M J Lenardo. The multifaceted role of Fas signaling in immune cell homeostasis and autoimmunity. *Nature immunology*, 1(6):469–74, December 2000.
- [17] F K Chan, H J Chun, L Zheng, R M Siegel, K L Bui, and M J Lenardo. A domain in TNF receptors that mediates ligand-independent receptor assembly and signaling. *Science (New York, N.Y.)*, 288(5475):2351–4, July 2000.
- [18] R M Siegel, J K Frederiksen, D a Zacharias, F K Chan, M Johnson, D Lynch, R Y Tsien, and M J Lenardo. Fas preassociation required for apoptosis signaling and dominant inhibition by pathogenic mutations. *Science (New York, N.Y.)*, 288(5475):2354–7, June 2000.
- [19] Naoto Itoh and Shigekazu Nagata. A Novel Protein Domain Required for Apoptosis. *The Journal of biological chemistry*, 268(May):10932–10937, 1993.
- [20] M Muzio, B R Stockwell, H R Stennicke, G S Salvesen, and V M Dixit. An induced proximity model for caspase-8 activation. *The Journal of biological chemistry*, 273(5):2926–30, January 1998.
- [21] Consuelo Gajate, Esther Del Canto-Jañez, a Ulises Acuña, Francisco Amat-Guerri, Emilio Geijo, Antonio M Santos-Beneit, Robert J Veldman, and Faustino Mollinedo. Intracellular triggering of Fas aggregation and recruitment of apoptotic molecules into Fas-enriched rafts in selective tumor cell apoptosis. *The Journal of experimental medicine*, 200(3):353–65, August 2004.

- [22] C. Gajate. The antitumor ether lipid ET-18-OCH<sub>3</sub> induces apoptosis through translocation and capping of Fas/CD95 into membrane rafts in human leukemic cells. *Blood*, 98(13):3860–3863, December 2001.
- [23] Michael D Tibbetts, Lixin Zheng, and Michael J Lenardo. The death effector domain protein family: regulators of cellular homeostasis. *Nature immunology*, 4(5):404–9, May 2003.
- [24] M Irmeler, M Thome, M Hahne, P Schneider, K Hofmann, V Steiner, J L Bodmer, M Schröter, K Burns, C Mattmann, D Rimoldi, L E French, and J Tschopp. Inhibition of death receptor signals by cellular FLIP. *Nature*, 388(6638):190–5, July 1997.
- [25] Jin Kuk Yang, Liwei Wang, Lixin Zheng, Fengyi Wan, Misonara Ahmed, Michael J Lenardo, and Hao Wu. Crystal structure of MC159 reveals molecular mechanism of DISC assembly and FLIP inhibition. *Molecular cell*, 20(6):939–49, December 2005.
- [26] D L Vaux, I L Weissman, and S K Kim. Prevention of programmed cell death in *Caenorhabditis elegans* by human bcl-2. *Science (New York, N.Y.)*, 258(5090):1955–7, December 1992.
- [27] R. M. Kluck. The Release of Cytochrome c from Mitochondria: A Primary Site for Bcl-2 Regulation of Apoptosis. *Science*, 275(5303):1132–1136, February 1997.
- [28] Preet M Chaudhary, Michael T Eby, Alan Jasmin, Arvind Kumar, Li Liu, and Leroy Hood. Activation of the NF- $\kappa$ B pathway by Caspase 8 and its homologs. *Oncogene*, 19(July):4451–4460, 2000.
- [29] Matthew S Hayden and Sankar Ghosh. Shared principles in NF- $\kappa$ B signaling. *Cell*, 132(3):344–62, February 2008.
- [30] C Zuliani, S Kleber, S Klussmann, T Wenger, M Kenzelmann, N Schreglmann, a Martinez, J a del Rio, E Soriano, P Vodrazka, R Kuner, H-J Groene, I Herr, P H Krammer, and a Martin-Villalba. Control of neuronal branching by the death receptor CD95 (Fas/Apo-1). *Cell death and differentiation*, 13(1):31–40, January 2006.
- [31] Julie Desbarats, Raymond B Birge, Manuelle Mimouni-Rongy, David E Weinstein, Jean-Sébastien Palerme, and M Karen Newell. Fas engagement induces neurite growth through ERK activation and p35 upregulation. *Nature cell biology*, 5(2):118–25, February 2003.



- [32] Inna N Lavrik, Alexander Golks, Dagmar Riess, Martin Bentele, Roland Eils, and Peter H Krammer. Analysis of CD95 threshold signaling: triggering of CD95 (FAS/APO-1) at low concentrations primarily results in survival signaling. *The Journal of biological chemistry*, 282(18):13664–71, May 2007.
- [33] C Scaffidi, S Fulda, a Srinivasan, C Friesen, F Li, K J Tomaselli, K M Debatin, P H Krammer, and M E Peter. Two CD95 (APO-1/Fas) signaling pathways. *The EMBO journal*, 17(6):1675–87, March 1998.
- [34] Philipp J Jost, Stephanie Grabow, Daniel Gray, Mark D McKenzie, Ueli Nachbur, David C S Huang, Philippe Bouillet, Helen E Thomas, Christoph Borner, John Silke, Andreas Strasser, and Thomas Kaufmann. XIAP discriminates between type I and type II FAS-induced apoptosis. *Nature*, 460(7258):1035–9, August 2009.
- [35] Alicia Algeciras-schimmich, Le Shen, Bryan C Barnhart, Andrea E Murmann, Janis K Burkhardt, and Marcus E Peter. Molecular Ordering of the Initial Signaling Events of CD95. *Molecular and Cellular Biology*, 22(1):207–220, 2002.
- [36] F C Kischkel, S Hellbardt, I Behrmann, M Germer, M Pawlita, P H Krammer, and M E Peter. Cytotoxicity-dependent APO-1 (Fas/CD95)-associated proteins form a death-inducing signaling complex (DISC) with the receptor. *The EMBO journal*, 14(22):5579–88, November 1995.
- [37] Richard M Siegel, Jagan R Muppidi, Malabika Sarker, Adrian Lobito, Melinda Jen, David Martin, Stephen E Straus, and Michael J Lenardo. SPOTS: signaling protein oligomeric transduction structures are early mediators of death receptor-induced apoptosis at the plasma membrane. *The Journal of cell biology*, 167(4):735–44, November 2004.
- [38] Christine Feig, Vladimir Tchikov, Stefan Schütze, and Marcus E Peter. Palmitoylation of CD95 facilitates formation of SDS-stable receptor aggregates that initiate apoptosis signaling. *The EMBO journal*, 26(1):221–31, January 2007.
- [39] I E Wertz and V M Dixit. Regulation of death receptor signaling by the ubiquitin system. *Cell death and differentiation*, 17(1):14–24, January 2010.
- [40] Marilyn D Resh. Palmitoylation of ligands, receptors, and intracellular signaling molecules. *Science’s STKE : signal transduction knowledge environment*, 2006(359):re14, October 2006.
- [41] Martin Klíma, Jitka Zájedová, Lenka Doubravská, and Ladislav Andera. Functional analysis of the posttranslational modifications of the death receptor 6. *Biochimica et biophysica acta*, 1793(10):1579–87, October 2009.

- [42] Krittalak Chakrabandhu, Zoltán Hérincs, Sébastien Huault, Britta Dost, Ling Peng, Fabien Conchonaud, Didier Marguet, Hai-Tao He, and Anne-Odile Hueber. Palmitoylation is required for efficient Fas cell death signaling. *The EMBO journal*, 26(1):209–20, January 2007.
- [43] Olga M Shatnyeva, Andriy V Kubarenko, Claudia E M Weber, Alexander Pappa, Reinhard Schwartz-Albiez, Alexander N R Weber, Peter H Krammer, and Inna N Lavrik. Modulation of the CD95-induced apoptosis: the role of CD95 N-glycosylation. *PloS one*, 6(5):e19927, January 2011.
- [44] Frank Henkler, Eva Behrle, Kevin M Dennehy, Andreas Wicovsky, Nathalie Peters, Clemens Warnke, Klaus Pfizenmaier, and Harald Wajant. The extracellular domains of FasL and Fas are sufficient for the formation of supramolecular FasL-Fas clusters of high stability. *The Journal of cell biology*, 168(7):1087–98, March 2005.
- [45] Benjamin Chaigne Delalande, Jean François Moreau, and Patrick Legembre. Rewinding the DISC. *Archivum immunologiae et therapiæ experimentalis*, 56:9–14, 2008.
- [46] Jagan R Muppidi and Richard M Siegel. Ligand-independent redistribution of Fas (CD95) into lipid rafts mediates clonotypic T cell death. *Nature immunology*, 5(2):182–9, February 2004.
- [47] Patrick Legembre, Sophie Daburon, Patrick Moreau, Francesca De Giorgi, and Jean-luc Taupin. Amplification of Fas-Mediated Apoptosis in Type II Cells via Microdomain Recruitment. *Molecular and Cellular Biology*, 25(15):6811–6820, 2005.
- [48] a Cremesti, F Paris, H Grassmé, N Holler, J Tschopp, Z Fuks, E Gulbins, and R Kolesnick. Ceramide enables fas to cap and kill. *The Journal of biological chemistry*, 276(26):23954–61, June 2001.
- [49] Consuelo Gajate and Faustino Mollinedo. Cytoskeleton-mediated death receptor and ligand concentration in lipid rafts forms apoptosis-promoting clusters in cancer chemotherapy. *The Journal of biological chemistry*, 280(12):11641–7, March 2005.
- [50] S Parlato, a M Giammarioli, M Logozzi, F Lozupone, P Matarrese, F Luciani, M Falchi, W Malorni, and S Fais. CD95 (APO-1/Fas) linkage to the actin cytoskeleton through ezrin in human T lymphocytes: a novel regulatory mechanism of the CD95 apoptotic pathway. *The EMBO journal*, 19(19):5123–34, October 2000.
- [51] Kyeong-Hee Lee, Christine Feig, Vladimir Tchikov, Robert Schickel, Cora Hallas, Stefan Schütze, Marcus E Peter, and Andrew C Chan. The role of receptor internalization in CD95 signaling. *The EMBO journal*, 25(5):1009–23, March 2006.

- [52] Stefan Schütze, Vladimir Tchikov, and Wulf Schneider-Brachert. Regulation of TNFR1 and CD95 signalling by receptor compartmentalization. *Nature reviews. Molecular cell biology*, 9(8):655–62, August 2008.
- [53] D a Martin, L Zheng, R M Siegel, B Huang, G H Fisher, J Wang, C E Jackson, J M Puck, J Dale, S E Straus, M E Peter, P H Krammer, S Fesik, and M J Lenardo. Defective CD95/APO-1/Fas signal complex formation in the human autoimmune lymphoproliferative syndrome, type Ia. *Proceedings of the National Academy of Sciences of the United States of America*, 96(8):4552–7, April 1999.
- [54] Francis Ka-ming Chan. Three is Better Than One: Pre-Ligand Receptor Assembly in the Regulation of TNF Receptor Signaling. *NIH-Pa*, 37(2):101–107, 2008.
- [55] Masato Tanaka, Takashi Suda, Takehiro Yatomi, Norio Nakamura, and Shigekazu Nagata. Lethal Effect of Recombinant Human Fas Ligand in Mice Pretreated with *Propionibacterium acnes*. *The Journal of Immunology*, 158(5):2303–2309, 1997.
- [56] Kolja Schleich, Uwe Warnken, Nicolai Fricker, Selcen Oztürk, Petra Richter, Kerstin Kammerer, Martina Schnölzer, Peter H Krammer, and Inna N Lavrik. Stoichiometry of the CD95 Death-Inducing Signaling Complex: Experimental and Modeling Evidence for a Death Effector Domain Chain Model. *Molecular cell*, June 2012.
- [57] H J Schoenfeld, B Poeschl, J R Frey, H Loetscher, W Hunziker, a Lustig, and M Zulauf. Efficient purification of recombinant human tumor necrosis factor beta from *Escherichia coli* yields biologically active protein with a trimeric structure that binds to both tumor necrosis factor receptors. *The Journal of biological chemistry*, 266(6):3863–9, February 1991.
- [58] J H Naismith, B J Brandhuber, T Q Devine, and S R Sprang. Seeing double: crystal structures of the type I TNF receptor. *Journal of molecular recognition : JMR*, 9(2):113–7, 1996.
- [59] J Mongkolsapaya, J M Grimes, N Chen, X N Xu, D I Stuart, E Y Jones, and G R Screaton. Structure of the TRAIL-DR5 complex reveals mechanisms conferring specificity in apoptotic initiation. *Nature structural biology*, 6(11):1048–53, November 1999.
- [60] Craig A Smith, Terry Farmh, and Raymond Goodwin. The TNF Receptor Superfamily of Cellular and Viral Proteins : Activation & stimulation and Death. *Cell*, 76:959–962, 1996.
- [61] B Huang, M Eberstadt, ET Olejniczak, and RP Meadows. NMR structure and mutagenesis of the Fas (APO-1/CD95) death domain. *Nature*, 384(19):638–641, 1996.

- [62] Fiona L Scott, Boguslaw Stec, Cristina Pop, Małgorzata K Dobaczewska, JeongEun J Lee, Edward Monosov, Howard Robinson, Guy S Salvesen, Robert Schwarzenbacher, and Stefan J Riedl. The Fas-FADD death domain complex structure unravels signalling by receptor clustering. *Nature*, 457(7232):1019–22, February 2009.
- [63] Liwei Wang, Jin Kuk Yang, Venkataraman Kabaleeswaran, Amanda J Rice, Anthony C Cruz, Ah Young Park, Qian Yin, Ermelinda Damko, Se Bok Jang, Stefan Raunser, Carol V Robinson, Richard M Siegel, Thomas Walz, and Hao Wu. The Fas-FADD death domain complex structure reveals the basis of DISC assembly and disease mutations. *Nature structural & molecular biology*, 17(11):1324–9, November 2010.
- [64] Hyun Ho Park. Structural features of caspase-activating complexes. *International journal of molecular sciences*, 13(4):4807–18, January 2012.
- [65] J R Muppidi, a a Lobito, M Ramaswamy, J K Yang, L Wang, H Wu, and R M Siegel. Homotypic FADD interactions through a conserved RXDLL motif are required for death receptor-induced apoptosis. *Cell death and differentiation*, 13(10):1641–50, October 2006.
- [66] Philipp J Keller, Annette D Schmidt, Joachim Wittbrodt, and Ernst H K Stelzer. Reconstruction of Zebrafish Early Light Sheet Microscopy. *Science*, 322(November):1065–1069, 2008.
- [67] Denis Semwogerere and Eric R Weeks. Confocal Microscopy. In *Encyclopedia of Biomaterials and Biomedical Engineering*. Taylor and Francis, 2005.
- [68] David M Shotton. Confocal scanning optical microscopy and its applications for biological specimens. *Journal of cell science*, 94:175–206, 1989.
- [69] S W Hell and J Wichmann. Breaking the diffraction resolution limit by stimulated emission: stimulated-emission-depletion fluorescence microscopy. *Optics letters*, 19(11):780–2, June 1994.
- [70] Marcel a Lauterbach, Chaitanya K Ullal, Volker Westphal, and Stefan W Hell. Dynamic imaging of colloidal-crystal nanostructures at 200 frames per second. *Langmuir : the ACS journal of surfaces and colloids*, 26(18):14400–4, September 2010.
- [71] Volker Westphal and Stefan Hell. Nanoscale Resolution in the Focal Plane of an Optical Microscope. *Physical Review Letters*, 94(14):1–4, April 2005.
- [72] Matthias Reuss. *Simpler STED setups*. PhD thesis, Deutsches Krebsforschungszentrum Heidelberg, 2010.

- [73] Matthias Reuss, Johann Engelhardt, and Stefan W Hell. Birefringent device converts a standard scanning microscope into a STED microscope that also maps molecular orientation. *Optics express*, 18(2):1049–58, January 2010.
- [74] Pit Bingen, Matthias Reuss, Johann Engelhardt, and Stefan W Hell. Parallelized STED fluorescence nanoscopy. *Optics express*, 19(24):23716–26, November 2011.
- [75] G Saffman and M Delbrock. Brownian motion in biological membranes. *Proceedings of the National Academy of Sciences of the United States of America*, 72(8):3111–3113, 1975.
- [76] Y Gambin, R Lopez-Esparza, M Reffay, E Sieracki, N S Gov, M Genest, R S Hodges, and W Urbach. Lateral mobility of proteins in liquid membranes revisited. *Proceedings of the National Academy of Sciences of the United States of America*, 103(7):2098–102, February 2006.
- [77] Ali Naji, Alex J Levine, and P a Pincus. Corrections to the Saffman-Delbruck mobility for membrane bound proteins. *Biophysical journal*, 93(11):L49–51, December 2007.
- [78] Gernot Guigas and Matthias Weiss. Size-dependent diffusion of membrane inclusions. *Biophysical journal*, 91(7):2393–8, October 2006.
- [79] S.J. Singer and G.L. Nicolson. The fluid mosaic model of the structure of cell membranes. *Science*, 175:720–731, 1972.
- [80] Matthias Weiss, Hitoshi Hashimoto, and Tommy Nilsson. Anomalous protein diffusion in living cells as seen by fluorescence correlation spectroscopy. *Biophysical journal*, 84(6):4043–52, June 2003.
- [81] Kirsten Bacia, Dag Scherfeld, Nicoletta Kahya, and Petra Schwille. Fluorescence correlation spectroscopy relates rafts in model and native membranes. *Biophysical journal*, 87(2):1034–43, August 2004.
- [82] K Simons and E Ikonen. Functional rafts in cell membranes. *Nature*, 387(6633):569–72, June 1997.
- [83] Dylan M Owen, David Williamson, Carles Rentero, and Katharina Gaus. Quantitative Microscopy : Protein Dynamics and Membrane Organisation. *Traffic (Copenhagen, Denmark)*, 10(10):962–971, 2009.
- [84] E a Reits and J J Neefjes. From fixed to FRAP: measuring protein mobility and activity in living cells. *Nature cell biology*, 3(6):145–7, June 2001.

- [85] Nectarios Klonis, Melanie Rug, Ian Harper, Mark Wickham, Alan Cowman, Tilley, and Leann. Fluorescence photobleaching analysis for the study of cellular dynamics. *European Biophysics Journal*, 31(1):36–51, March 2002.
- [86] Jennifer Lippincott-Schwartz, Nihal Altan-Bonnet, and George H Patterson. Photobleaching and photoactivation: following protein dynamics in living cells. *Nature cell biology*, Suppl(September):S7–14, September 2003.
- [87] a Partikian, B Olveczky, R Swaminathan, Y Li, and a S Verkman. Rapid diffusion of green fluorescent protein in the mitochondrial matrix. *The Journal of cell biology*, 140(4):821–9, February 1998.
- [88] R D Phair and T Misteli. High mobility of proteins in the mammalian cell nucleus. *Nature*, 404(6778):604–9, April 2000.
- [89] M J Dayel, E F Hom, and a S Verkman. Diffusion of green fluorescent protein in the aqueous-phase lumen of endoplasmic reticulum. *Biophysical journal*, 76(5):2843–51, May 1999.
- [90] N B Cole, C L Smith, N Sciaky, M Terasaki, M Edidin, and J Lippincott-Schwartz. Diffusional mobility of Golgi proteins in membranes of living cells. *Science (New York, N. Y.)*, 273(5276):797–801, August 1996.
- [91] John F Presley, Theresa H Ward, Andrea C Pfeifer, Eric D Siggia, Robert D Phair, and Jennifer Lippincott-Schwartz. Dissection of COPI and Arf1 dynamics in vivo and role in Golgi membrane transport. *Nature*, 417(6885):187–93, May 2002.
- [92] D J Stephens, N Lin-Marq, a Pagano, R Pepperkok, and J P Paccaud. COPI-coated ER-to-Golgi transport complexes segregate from COPII in close proximity to ER exit sites. *Journal of cell science*, 113 ( Pt 1:2177–85, June 2000.
- [93] K J Zaal, C L Smith, R S Polishchuk, N Altan, N B Cole, J Ellenberg, K Hirschberg, J F Presley, T H Roberts, E Siggia, R D Phair, and J Lippincott-Schwartz. Golgi membranes are absorbed into and reemerge from the ER during mitosis. *Cell*, 99(6):589–601, December 1999.
- [94] Anne K Kenworthy, Benjamin J Nichols, Catha L Remmert, Glenn M Hendrix, Mukesh Kumar, Joshua Zimmerberg, and Jennifer Lippincott-Schwartz. Dynamics of putative raft-associated proteins at the cell surface. *The Journal of cell biology*, 165(5):735–46, June 2004.
- [95] N Periasamy and a S Verkman. Analysis of fluorophore diffusion by continuous distributions of diffusion coefficients: application to photobleaching measurements of multicomponent and anomalous diffusion. *Biophysical journal*, 75(1):557–67, July 1998.

- [96] S R Chary and R K Jain. Direct measurement of interstitial convection and diffusion of albumin in normal and neoplastic tissues by fluorescence photobleaching. *Proceedings of the National Academy of Sciences of the United States of America*, 86(14):5385–9, July 1989.
- [97] Brian L Sprague, Robert L Pego, Diana a Stavreva, and James G McNally. Analysis of binding reactions by fluorescence recovery after photobleaching. *Biophysical journal*, 86(6):3473–95, June 2004.
- [98] Stephan Heinzer, Stefan Wörz, Claudia Kalla, Karl Rohr, and Matthias Weiss. A model for the self-organization of exit sites in the endoplasmic reticulum. *Journal of cell science*, 121(Pt 1):55–64, January 2008.
- [99] D Axelrod, D E Koppel, J Schlessinger, E Elson, and W W Webb. Mobility measurement by analysis of fluorescence photobleaching recovery kinetics. *Biophysical journal*, 16(9):1055–69, September 1976.
- [100] D. M. Soumpasis. Theoretical analysis fo fluorescence photobleaching recovery experiments. *Biophysical journal: Brief communication*, 1(January):95–97, 1983.
- [101] Matthias Weiss. Challenges and artifacts in quantitative photobleaching experiments. *Traffic (Copenhagen, Denmark)*, 5(9):662–71, September 2004.
- [102] Srikanth R. Chary and Rakesh K. Jain. Analysis of diffusive and convective recovery of fluorescence after photobleaching - effect of uniform flow field. *Chem. Eng. Comm.*, 55:235–249, 1987.
- [103] P Gribbon and T E Hardingham. Macromolecular diffusion of biological polymers measured by confocal fluorescence recovery after photobleaching. *Biophysical journal*, 75(2):1032–9, August 1998.
- [104] E. Livneh, R. Benveniste, R. Prywes, S. Felder, Z. Kam, and J Schlessinger. Large Deletions in the Cytoplasmic Kinase Domain of the Epidermal Growth Factor Receptor Do Not Affect Its Lateral Mobility. *Journal of cell biology*, 103(August):327–331, 1986.
- [105] Inhee Chung, Robert Akita, Richard Vandlen, Derek Toomre, Joseph Schlessinger, and Ira Mellman. Spatial control of EGF receptor activation by reversible dimerization on living cells. *Nature*, 464(7289):783–7, April 2010.

## C. Acknowledgements

I would like to thank Prof. Roland Eils for giving me the opportunity to work on this projects in his interdisciplinary group with almost no limitation in good scientists and equipment. His generosity has allowed me to persue projects according to my own point of view and wishes. It has been a pleasure to work in his lab.

I want to thank my supervisor Joël Beaudouin for his sheer endless patience and his generosity to offer his comprehensive knowledge and experience. The endless hours in the lab of microscopy and discussions about any scientific question, be it overall general topics or minor details of biology, programming, experimental of theoretical work. He was a great enrichment and source of growth for my personal and scientific life.

Danke an das Nikon Imaging Center der Universität Heidelberg für die Möglichkeit die dortigen hochwertigen Geräte zu benutzen, aber auch für die Einführung in das Messen und die bereitwillige Hilfe bei der Optimierung der Experimente. Danke an die Kollaborationspartner mit denen das Messen und Diskutieren immer ein großer Spaß war: Matthias Reuss, Michael Schwering, Clarissa Liesche, Stefan Wörz.



Danke an Dich, Christiane, für die wöchentliche unbezahlbare, unglaublich zuverlässige Unterstützung. In diesem halben Jahr habe ich so unglaublich viel von Dir gelernt, so unglaublich viel hat sich in mir verändert und nur Deinetwegen so gut entwickelt. All die Kraft und Stärke, die ich in den letzten Wochen und Monaten aufgebracht habe, hast Du mir gezeigt und gegeben. Danke Dir für diese großartige Hilfe! Vielen, vielen Dank!

Thanks to all my colleagues! Danke allen meinen Kollegen! Joël Beaudouin, Clarissa Liesche, Sabine Aschenbrenner, Stefan Kallenberger, Marti Bernardo, Paula Gonzalez, Daniela Richter, Yara Reiss, Tobias Ahsendorf, Manuela Schäfer, Corinna Sprengart, William Godinez, Charley Choe, Björn Bachmann, Barbara Di Ventura, Sven Meseke, Hanna Glenewinkel and many more.

Danke meinen Freunden für viel Geduld und Unterstützung in Krisenstunden. Jens Jaksch, Esther Witt, Falk Löwner, Caroline Zöllner, Daniela Casarrubea, Chiara Cigonini, Esmeralda Del Olmo, Jens Roat-Kultima, Rolf Sinkovec.

Danke fürs fleißige Korrekturlesen in letzter Minute: Marko Swoboda und Paul Fletcher. Ich hab so schnell noch so viel von Euch gelernt.

Danke meiner Familie für die immerwährende Unterstützung im Leben und im wissenschaftlichen Denken und Forschen.